A POINT CONTACT SPECTROSCOPY STUDY OF TOPOLOGICAL SUPERCONDUCTIVITY

A Thesis
Presented to
The Academic Faculty

by

Xunchi Chen

In Partial Fulfillment
of the Requirements for the Degree
Doctor of Philosophy in the
School of Physics

Georgia Institute of Technology
May 2015

A POINT CONTACT SPECTROSCOPY STUDY OF TOPOLOGICAL SUPERCONDUCTIVITY

Approved by:

Professor Zhigang Jiang,
Committee Chair
School of Physics
Georgia Institute of Technology

Professor Martin Mourigal
School of Physics
Georgia Institute of Technology

Professor Phillip First
School of Physics
Georgia Institute of Technology

Professor Jean Bellissard
School of Mathematics
Georgia Institute of Technology

Professor Andrew Zangwill
School of Physics
Georgia Institute of Technology

Date Approved: 11 March 2015

To my parents, Bai Ning and Chen Youkang.

ACKNOWLEDGEMENTS

First and foremost, I would like to thank my advisor, Dr. Zhigang Jiang. He is so much more than just an academic advisor to me. He is a mentor, a good friend, and a role model. Whether it's 9 am or 9 pm, his door is always open. He has trained me not only to become a better researcher, but also to become a better person, and I am forever in debt to him.

I would like to thank my committee members, Drs. Phil First, Andrew Zangwill, Jean Bellissard and Martin Mourigal for devoting their time to read my dissertation and to provide valuable feedback.

I thank my collaborators: Dr. Yew San Hor at Missouri University of Science and Technology, Dr. Haidong Zhou at the University of Tennessee at Knoxville, Dr. Satoshi Sasaki and Dr. Yoichi Ando at Osaka University for providing the samples; Dr. Erhai Zhao at George Mason University and Dr. Carlos Sà de Melo at Georgia Tech for providing theoretical calculations. I thank Dr. Britt Torrance for providing guidance in the niobium tip etching process.

I would also like to thank my peers, Feng Wang, Wenlong Yu, Wenchao Jiang, Feifei Qian, Xiaoyao Ma, James Palmer, Catlin Baker and Si Zhou, for fighting in the same trench with me. This journey would not be the same without you. I thank Yuxuan Jiang, Di Chen, Chao Huan, Owen Vail, Jeff Chen, Daniel Benjamin and Anton Sidorov for being good labmates and good friends. I am also grateful to all the friends and coworkers that I had the pleasure to meet in the Howey building, Lede Xian, Yike Hu, Yuntao Li, Chen Yang, Louise Wu, Ruomeng Yu, Shangguo Zhu, Lei Ma, Baiqian Zhang, Zelei Guo, Meredith Nevius and many others. I thank Sara Farooq, Sioney Mckeown, and Krista Burton for the wonderful summers we had.

I couldn't have done this work without the help and support from the staff in the physics department. I thank Scott Centers, Judy Melton, Keith Garner, Samantha King, Keia Dodd, Alison Morain and Ashley Jeter for their hard work. I thank Dennis Denny and Dennis Brown at the GTRI machine shop for making the sample stages and Mel Pinson at Airgas for always trying to accommodate our needs for gas and liquid helium. I thank Dr. Xiaoshan Wu at Nanjing University, who led me on to the road of physics research. I'd also like to thank the support from Georgia Tech cleanroom staff.

I dedicate this dissertation to my parents, Ning Bai and Youkang Chen, for their unconditional support and love, at good times and bad times.

Finally, I would like to thank you, whoever is reading this right now. I sincerely hope that my work can be of help to you.

TABLE OF CONTENTS

LIST OF TABLES

LIST OF FIGURES

SUMMARY

The study of topological superconductivity has been at the forefront of condensed matter physics for the past few years. Topological superconductors are predicted to have odd parity pairing and host so called Majorana fermions, which are not only of fundamental importance, but also proposed to be building blocks for fault-tolerant quantum computing. In this dissertation, we use point contact spectroscopy to study the pairing symmetry of candidate topological superconducting materials. We study proximity induced superconductivity in the topological insulator Bi_2Se_3 by a superconducting niobium tip, and propose a model to explain its features in point contact spectra. We further study the nature of the superconductivity in highly doped superconducting topological insulators, including $Cu_xBi_2Se_3$ and $Sn_{1-x}In_xTe$, using both a normal metal gold tip and a superconducting niobium tip. For $Cu_xBi_2Se_3$, we observe a robust zero-bias conductance peak (ZBCP) in the differential conductance spectra with the gold point contact, while with the niobium point contact we find the height of the peak exhibiting an unusual non-monotonic temperature dependence. We argue that both observations cannot be explained by Andreev reflection within the standard Blonder-Tinkham-Klapwijk (BTK) model, but signify unconventional superconductivity in the material. For $Sn_{1-x}In_xTe$ samples, we observe ZBCP in the differential conductance spectra with the gold point contact, while with the niobium point contact, the temperature dependence of ZBCP is monotonic as expected from conventional theory, leaving the nature of the superconductivity of $Sn_{1-x}In_xTe$ still an open question.

CHAPTER I

INTRODUCTION

Topological superconductors (TSCs) have drawn substantial attention in the condensed matter physics community, owing to the emerging research interest in topological order and possible application to quantum computing [36, 84]. In analogy to topological insulators (TI), TSCs possess gapless states on the surface that are protected by a topological invariant, while the bulk of the material is superconducting (consisting of a fully opened energy gap). It has been theoretically predicted that the pairing symmetries of TSCs are unconventional, and robust zero-energy Majorana bound states may appear on the surface [93, 55, 83, 91, 28, 35, 66]. Correlated (Bogoliubov) quasiparticles in such states may exhibit non-Abelian statistics [73], forming the basis for realizing intriguing proposals of fault-tolerant quantum computing [56, 76]. Creation, detection and manipulation of non-Abelian quasiparticles in strongly correlated systems have been a frontier of fundamental research in the past ten years. The emerging TSCs have added to this endeavor an intriguing possibility, *i.e.*, Majorana fermions.

The experimental investigation of time-reversal-invariant TSCs has just started, triggered by the discovery of superconductivity in the topological material, $Cu_xBi_2Se_3$ [39, 113, 62, 63] and $Sn_{1-x}In_xTe$ [90, 77]. The spin-orbit coupling (SOC) between the motion of conduction electrons and their spin is expected to be very strong in these materials, leading to a triplet component on the order parameter, which is largely responsible for its unconventional superconductivity and other exotic physical properties. Better understanding of the superconductivity of TSCs would shed light on the solid-state realization of Majorana fermions and provide valuable guidance for

the ongoing search of other TSCs [90].

In this dissertation, we present experimental studies of topological superconductivity using point contact spectroscopy. Proximity induced superconductivity in TI samples are investigated, as well as the superconductivity of TSC samples. Our results strongly favor unconventional pairing symmetry in the TSCs. Before delving into the experiment details, we first give an overview of the newly discovered playground of topological materials.

1.1 Topological insulators

One of the greatest triumphs of 20th century solid state physics is the invention of band theory. Band theory classifies solids into metals and insulators based on whether there is a band gap between the conduction band and the valence band. Only very recently have scientists realized insulators can be further classified according to the topology of the Hilbert space. Recall from quantum mechanics that wave functions are described using linear combinations of a basis set of orthonormal vectors. This basis set is said to span an abstract space called the Hilbert space. It turns out the mathematical concept of topology (see Fig. 1) is relevant to the electronic states in insulators. The Hilbert space for different insulators can have different topologies, thus insulators can be labeled by a topological parameter. The topological order has profound influence on the electronic properties of the insulators. For insulators with a topology different from that of the vacuum, the term "topological insulator" was created.

The first example of a TI ever known is in the very familiar integer quantum Hall effect (IQHE). Discovered by von Klitzing and coworkers in 1980 [58], the IQHE is the phenomenon that high mobility 2-dimension electron gas (2DEG) exhibits quantized circular motion in a strong external magnetic field. As shown in Fig. 2, the electrons become localized in strong magnetic field and the energy of the circular motion is

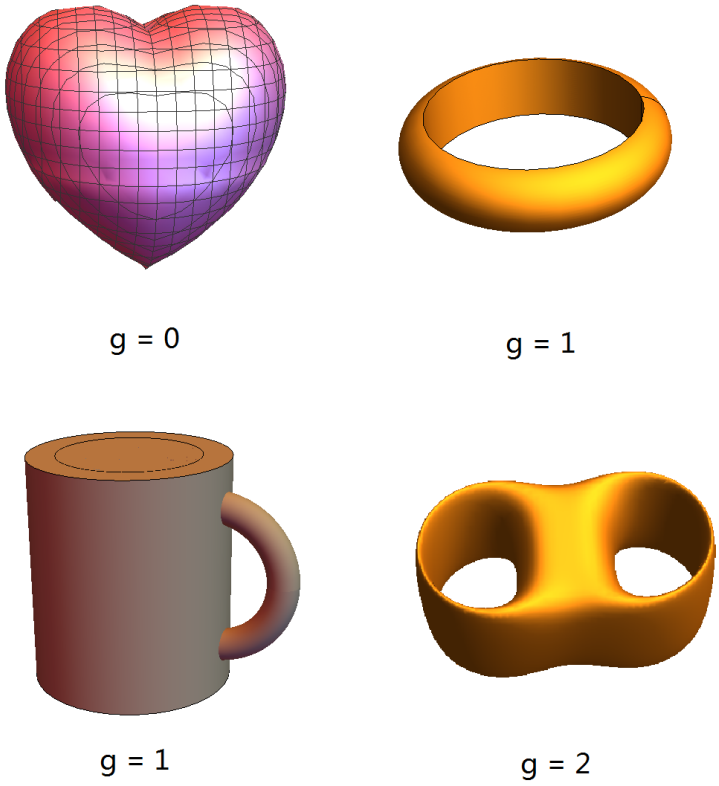

Figure 1: Basics of topology. In mathematics, two geometric shapes are said to be topologically equivalent if one can be smoothly deformed into another without tearing or gluing. The topology can be indexed by a surface integral called the genus: $2g = 2 - 1/(2\pi)\int_S KdA$, where K is the Gaussian curvature. Loosely speaking, the genus equals to the number of holes in the shape. Topologically, a ring is identical to a mug (g=1), but different from a heart (g=0).

quantized to the so called Landau levels. The Hall conductivity in this case is precisely quantized: $\sigma_{xy} = I_{xx}/V_{xy} = n \times e^2/h$, where e is the electron charge, h is Planck's constant and n is a positive integer.

In 1982, Thouless, Kohmoto, Nightngale, and den Nijs (TKNN) [107] pointed out that the precise quantization of Hall conductivity has a topological origin. The quantization number n can be calculated as an integral of the Bloch wave function over the Brillouin zone (BZ) [38]:

$$n = \frac{1}{2\pi}\int_{BZ} \mathrm{d}^2\mathbf{k}\nabla \times \mathbf{A} \tag{1}$$

where k is the momentum vector, $\mathbf{A}$ is the Berry connection and $\nabla \times \mathbf{A}$ is the Berry's

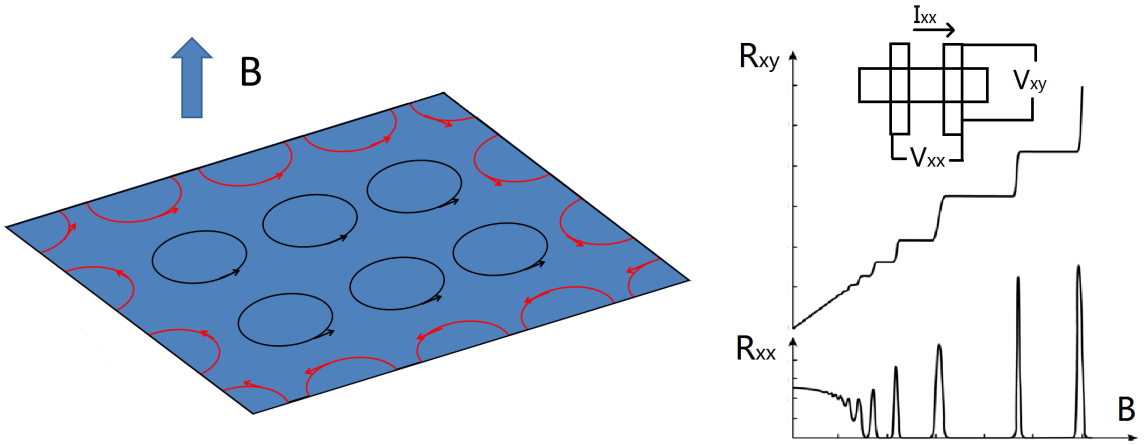

Figure 2: The integer quantum Hall effect. Left: In strong magnetic field, electrons in 2DEG form circular motions under the Lorentz force and become localized, but the incomplete circles on the edges (in red) provide a conducting edge channel. Right: Typical longitudinal ($R_{xx} = V_{xx}/I_{xx}$) and Hall ($R_{xy} = V_{xy}/I_{xx}$) resistances of the IQHE as a function of the magnetic field (data adapted from Ref. [110]). R_{xy} becomes quantized within a Landau level while R_{xx} diminishes.

curvature. Hence, the integer n is also called the TKNN invariant. In IQHE system, the energy gap has a different TKNN invariant than that of the vacuum (which has $n = 0$), so the IQHE system is a topological insulator. The quantization of σ_{xy} is protected by the TKNN invariant, and has been measured to be accurate up to three parts per billion [108].

An important consequence of the topological protection in IQHE is the edge state. At the boundary between IQHE and vacuum the energy gap cannot smoothly transit from a TKNN number of n to 0. As a result, a gapless edge state appears to connect the two topologically different gaps [34]. A wonderful property of this edge state is that since it is under topological protection, it is immune from scattering, which is why the longitudinal resistance of IQHE is $R_{xx} = 0$ (Fig. 2). A phase transition always happens at the boundary of a TI phase and a topologically trivial phase (such as the vacuum), so the boundary state is a hallmark of TIs.

The quantum Hall effect requires a magnetic field and thus breaks time reversal symmetry (TRS). The quantum spin Hall effect (QSHE) is an example of 2D TI that

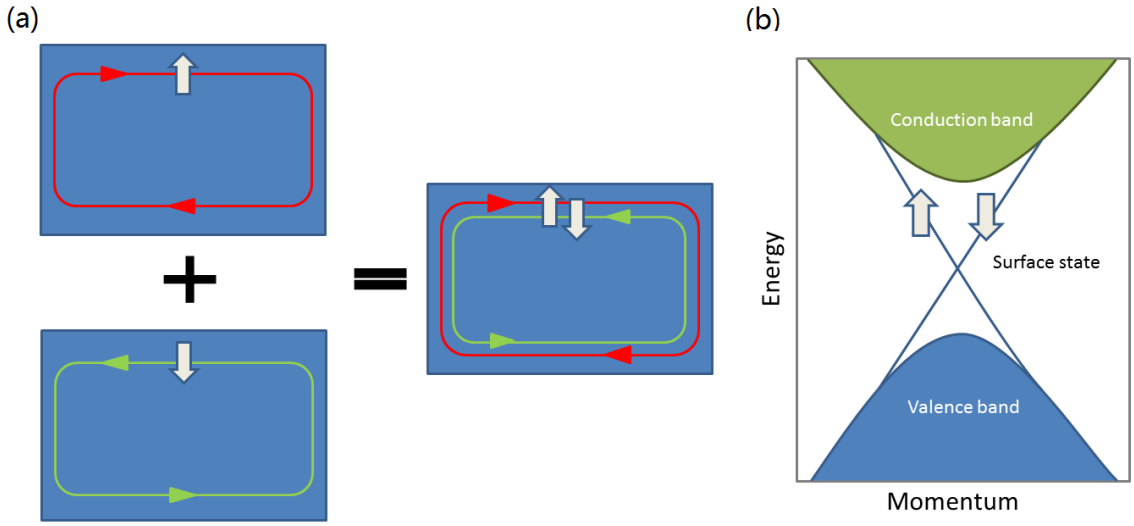

Figure 3: The quantum spin Hall effect. (a) The edge state of QSHE is like two copies of IQHE added together. One conducting channel is for spin up electrons, and the other for spin down electrons (The spin direction is represented by the grey arrows). There is no external magnetic field in this case. (b) The band structure of QSHE. A gapless surface state protected by TRS resides inside the bulk band gap.

does not break TRS. It was proposed by Kane and Mele [47], and later independently by Bernevig and Zhang [11]. QSHE occurs in 2DEG with strong SOC. The SOC replaces the role of the magnetic field in the Hamiltonian. Because spin has two directions, the QSHE can be seen as two copies of spin polarized quantum Hall systems added together, one with spin up and the other with spin down, and the overall TRS is preserved. This is depicted in Fig. 3.

The QSHE is protected by a Z_2 topology index. Here Z means integer and 2 means the Hilbert space can be classified into two distinct kinds based on the Z_2 index (odd and even). A detailed mathematical derivation of the Z_2 index can be found in Ref. [2]. Just as its IQHE counterpart, the QSHE has quantized Hall conductance σ_{xy} and gapless edge states that are immune to scattering, due to the topological protection. The first experimentally feasible QSHE system is proposed by Bernevig, Hughes, and Zhang [12] in CdTe/HgTe/CdTe quantum wells. The quantization of σ_{xy} was soon observed by König and coworkers [60], which kick-started the golden age of topological

insulators.

The Z_2 topology can be extended to 3-dimension (3D), and it turns out that four Z_2 invariants are needed to fully characterize the topology [74, 30]. Many 3D TIs have been proposed and verified, including $Bi_{1-x}Sb_x$ [29, 40], Bi_2Se_3 [123, 114], Bi_2Te_3 [123, 16], and more. The main experimental methods to verify TIs are to look for the protected surface states by surface spectroscopy measurements, such as angle-resolved photoemission spectroscopy [16] and scanning tunneling microscopy [18].

Since the study of superconductivity in 3D TIs is the main focus of this dissertation, it is worth mentioning some important properties of 3D TIs due to the TRS protection.

1. Gapless surface band protected by TRS. At the surface of 3D TIs, the energy gap cannot smoothly transit to that of the vacuum, because of the different topological order. The TRS thus guarantees a gapless surface state. Magnetic doping, which breaks the TRS, can open a band gap at the surface [17]. It should also be noted that for extremely thin TI films, hybridization of the top and bottom surfaces can open up a gap too [124].

2. Helical Dirac fermions in the surface band. Another consequence of the TRS protection is that the energy dispersion near the crossing of the surface band is approximately linear, and can be described by the Dirac equation for massless particles. The low energy band structure of TI is thus a 2D Dirac cone, and the crossing of the surface band is therefore called the Dirac point. In other words, the electrons on the surface of 3D TRS TIs are 2D massless Dirac fermions. This is very similar to the carriers in graphene [32], but the TI does not have the spin nor valley degeneracy comparing to graphene, making the TI a simpler system to study Dirac fermion physics.

3. π Berry phase. An interesting property of the Dirac fermion is the π Berry

phase [1]. In a nutshell, this means that if the wave vector of the TI is adiabatically rotated counterclockwise along a closed path that encircle the origin, the wave vector will gain an additional phase of π. The additional phase has observable consequences such as the weak anti-localization [106] and half-integer quantization of the Landau level [78].

4. Spin-momentum locking on the surface. This is another unique property to the TRS protection. The spin is non-degenerate in the surface state, and its direction is always perpendicular to the momentum vector. This is called the helicity of spins, and it has been found to be left handed [See Fig. 4(a)]. This helical spin polarization implies a dissipationless spin current flowing on the surface of TI, even if there is no electric current. Moreover, because reversing the direction of $\mathbf{k}$ means the spin direction must also be reversed, back-scattering is prohibited on the surface of 3D TIs [88].

In the QSHE and 3D TI example described above, the topological invariants are both protected by TRS. TIs can also be protected by other symmetries. For example, in a topological crystalline insulator [27, 42], the role of TRS protection is replaced by the space group symmetries of the crystalline system. In principle, there are many possibilities of topological orders of the Hilbert space [37].

1.2 Topological superconductors and Majorana fermions

Since the discovery of topological insulators, enormous efforts have been put into studying the superconducting phase of the topological materials, primarily driven by the quest for searching the so called Majorana fermion (MF). This object was proposed by Ettore Majorana in 1937 as a real solution to the Dirac equation. The most interesting aspect of the MF in condensed matter physics is that it obeys a non-Abelian statistics distribution [76]. Unlike regular boson and fermion systems where exchanging particles has no measurable effects, exchanging MFs *will* change

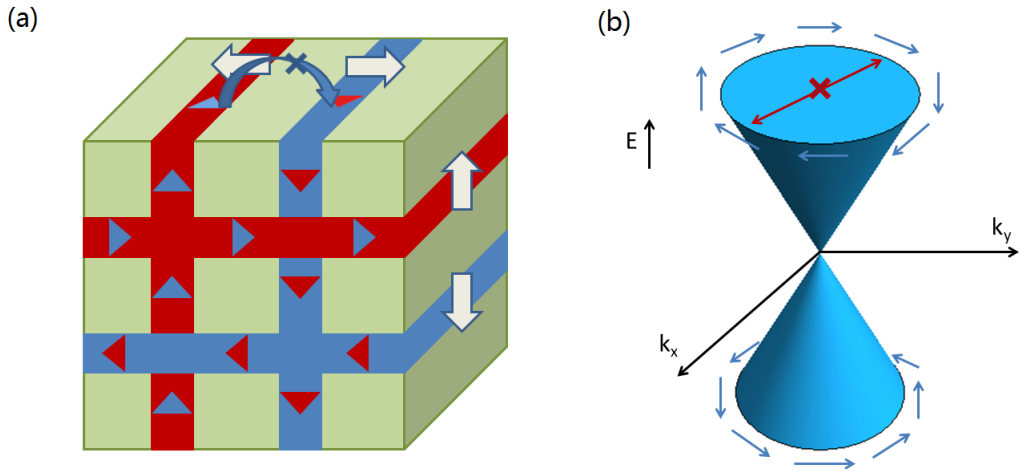

Figure 4: Spin-momentum locking on the surface of a 3D TI in (a) real space and (b) momentum space. The momentum of the electron [represented by blue and red triangles in (a)] determines the spin direction, and back scattering is prohibited.

the quantum state of the system. Some clever manipulations of these non-Abelian particles can create quantum bits for fault-tolerant quantum computers [76, 56].

A MF is charge neutral and is its own antiparticle, which are pretty stringent conditions. Although any Dirac fermion can be seen as a pair of MFs ($a = \gamma_1 + i\gamma_2$), the spin degeneracy must be lifted to delocalize the pair. Here, a is the operator for the Dirac fermion, and γ_1 and γ_2 are the operators for the pair of MFs. 70 years after the original theoretical proposal, whether there exist elementary particles that are MFs still remains an open question. On the other hand, it is possible to realize MFs as quasiparticles (*i.e.* electron and hole excitations) in condensed matter systems. In fact, in superconductors particle-hole symmetry is observed, and in TIs the spin degeneracy is broken. If the two can be combined, then a MF should manifest itself as a zero energy state in the superconducting gap.

One way to realize a zero energy Majorana bound state is through the proximity effect [31]. The low energy quasiparticle energy levels within the superconducting gap are solutions of the Bogoliubov-de Gennes equation [23]. For a conventional s-wave superconductor, these energy levels are arranged symmetrically around zero energy,

but there is no zero energy state (Fig. 5). If an s-wave superconductor is brought into proximity with a TI, the singlet Cooper pairs can leak into the TI. Due to the π Berry phase in a TI, the quasiparticle energy levels are shifted, and a zero energy state appears (The same mechanism is responsible for the zero energy Landau level in graphene).

Another way to produce MFs is to dope a TI to make it superconducting. In this case, the bulk of the TI becomes superconducting, and if the SOC is sufficiently strong, the Cooper pairs will have an odd-parity pairing. This means the Cooper pairs in the material have non-zero angular momentum. If such a superconductor is centrosymmetric, then the order parameter of the superconductor is itself topologically nontrivial [28]. The doped TI then becomes a topological superconductor, and hosts MFs as zero energy quasiparticles in its surface band. Unlike the topologically trivial, spin degenerate p-wave superconductors (e.g. Sr_2RuO_4) where the pairing is fragile, the pairing in TSC is protected by TRS and is immune to disorder.

In this thesis, we will look for signatures of MFs in both the proximity induced superconductivity in TIs, and the bulk superconductivity in doped TIs.

1.3 Outline of thesis

This thesis is organized as the following: Chapter 2 describes the sample growth process and explores some fundamental material properties of TIs. Chapter 3 introduces point contact spectroscopy, which is the main experiment technique used in this dissertation. A discussion of the theory behind the electronic transport through a point contact is presented. Chapter 4 discusses the experiment setup, including the mechanical and electronics setup of the experiments, and the preparation of point contact tips. Chapter 5 is devoted to the point contact measurement using conventional superconductor tip on topological insulators. The nature of the observed

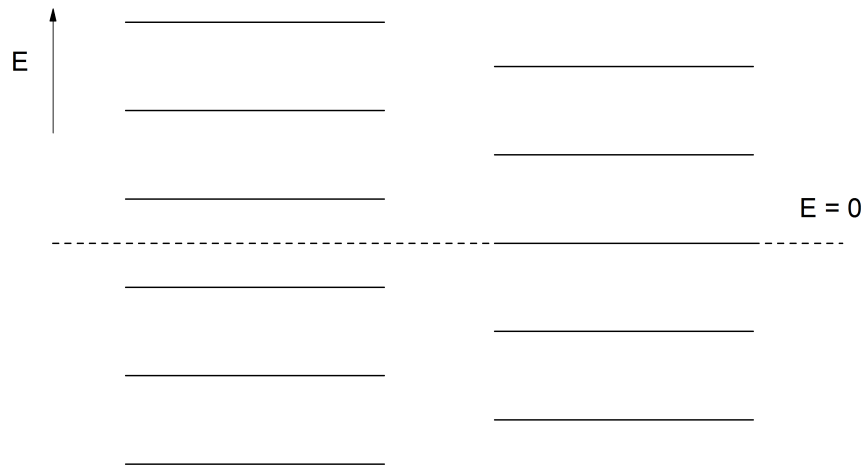

Figure 5: Schematic of two possible low energy excitation spectrum of a superconductor. On the left is a topologically trivial phase, where there is no zero energy state. On the right is a TSC, where a protected zero energy state exists. For the proximity induced superconductivity in TI, the zero energy state is protected by the π Berry phase. Quasiparticles at $E = 0$ are Majorana fermions.

proximity induced superconductivity is discussed. Chapter 6 presents the point contact experiments on TSCs $Cu_xBi_2Se_3$ and $Sn_{1-x}In_xTe$. Both superconducting and nonsuperconducting tips are used to probe these samples, and the implications of the results on the pairing symmetries of the samples are discussed. Chapter 7 concludes the thesis.

CHAPTER II

SAMPLE PREPARATION AND CHARACTERIZATION

2.1 Growth of topological insulator Bi_2Se_3 and Sb_2Te_3 single crystals

The first proposed and confirmed 3D TI is Bi_xSb_{1-x} [29, 40]. It is an alloy with random substitutional disorder (so the electronic structures are only defined within the mean field) and has extremely complex surface states with at least five dispersion branches. This makes both the theoretical and experimental studies of the material very complicated. In an effort to search for stoichiometric TIs, Zhang and coworkers [123] calculated the band structures of $Bi(Sb)_2Se(Te)_3$ family of materials. They found that if the SOC, added to chemical bonding and crystal-field splitting, is strong enough to push the $P1_z^+$ orbitals of Bi(Sb) atoms to below the $P2_z^-$ orbitals of the Se(Te) atoms , the band inversion will drive the material to be a topological insulator [Fig. 6(b)]. This mechanism is in exact analogous to that in the 2D TI HgTe [12]. Their calculation shows that the SOCs in Bi_2Se_3, Bi_2Te_3 and Sb_2Te_3 are strong enough to induce the topological non-trivial phase, while Sb_2Se_3 is a trivial band insulator. The $Bi(Sb)_2Se(Te)_3$ family has well defined crystal structure and simple surface band topology [Fig. 6(c)], with only a single Dirac cone located at the center of the Brillouin zone. Also Bi_2Se_3 has a relatively large band gap of 0.3 eV (0.16 eV for Bi_2Te_3 and 0.28 eV for Sb_2Te_3), which is larger than the energy scale of room temperature. For these reasons, the $Bi(Sb)_2Se(Te)_3$ family is much more favored by the community to study as a prototype TI, both theoretically and experimentally.

Single crystal Bi_2Se_3 has a rhombohedral crystal structure with the space group $D_{3d}^5(R\bar{3}m)$. There are five atoms in the trigonal primitive cell. A straightforward

way to visualize the structure is to use a hexagonal lattice with the unit cell being a quintuple layer, as shown in Fig. 6(a). Like graphite, adjacent Se-Se layers are held together by weak van der Waals force. Bi_2Te_3 and Sb_2Te_3 have a similar crystal structure by substituting Bi atoms with Sb and Se with Te, respectively.

Large grain polycrystalline Bi2Se3 materials (single crystal grain size >1 mm) were synthesized by Dr. Peter Sharma's group at the Sandia National Laboratories. First, Bi_2Se_3 pieces (99.999%, from VWR international, LLC.) were placed in an evacuated (< 107 Torr) quartz ampoule and melted at 800 °C for 16 h. The melt was then cooled at 10 °C/h to 550 °C, held for 3 days at this temperature, and finally allowed to furnace cool to room temperature. Single crystals of Sb_2Te_3 were grown using Bridgman method by Dr. Y. P. Chen's group at the Purdue University. Stoichiometric amount of high purity antimony and tellurium (99.999%) was deoxidized and purified by multiple vacuum distillations under dynamic vacuum of < 107 Torr and then heated up to 900 °C. This was followed by a slow cool down under a controlled pressure to minimize tellurium defects. Afterwards, the crystals were grown at a speed of 0.5-1.5 mm/h with a linear temperature gradient set to 5 °C/cm. A typical X-ray diffraction (XRD) spectrum of the sample is shown in Fig. 6(d). The as-grown Bi_2Se_3 crystals are naturally n-doped due to remnant Se vacancies. Hall measurements show typical carrier densities over 1×10^{18} cm^{-3} at ambient conditions. Sb_2Te_3 crystals are grown in a similar fashion. It is important to note that although $Bi(Sb)_2Se(Te)_3$ family of materials are band insulators, natural doping causes the Fermi levels to be in the conduction bands, thus the materials are bulk conducting. It is very difficult to distinguish between bulk and surface transport experimentally, which is why most experimental studies of the material have been focused on surface spectroscopies.

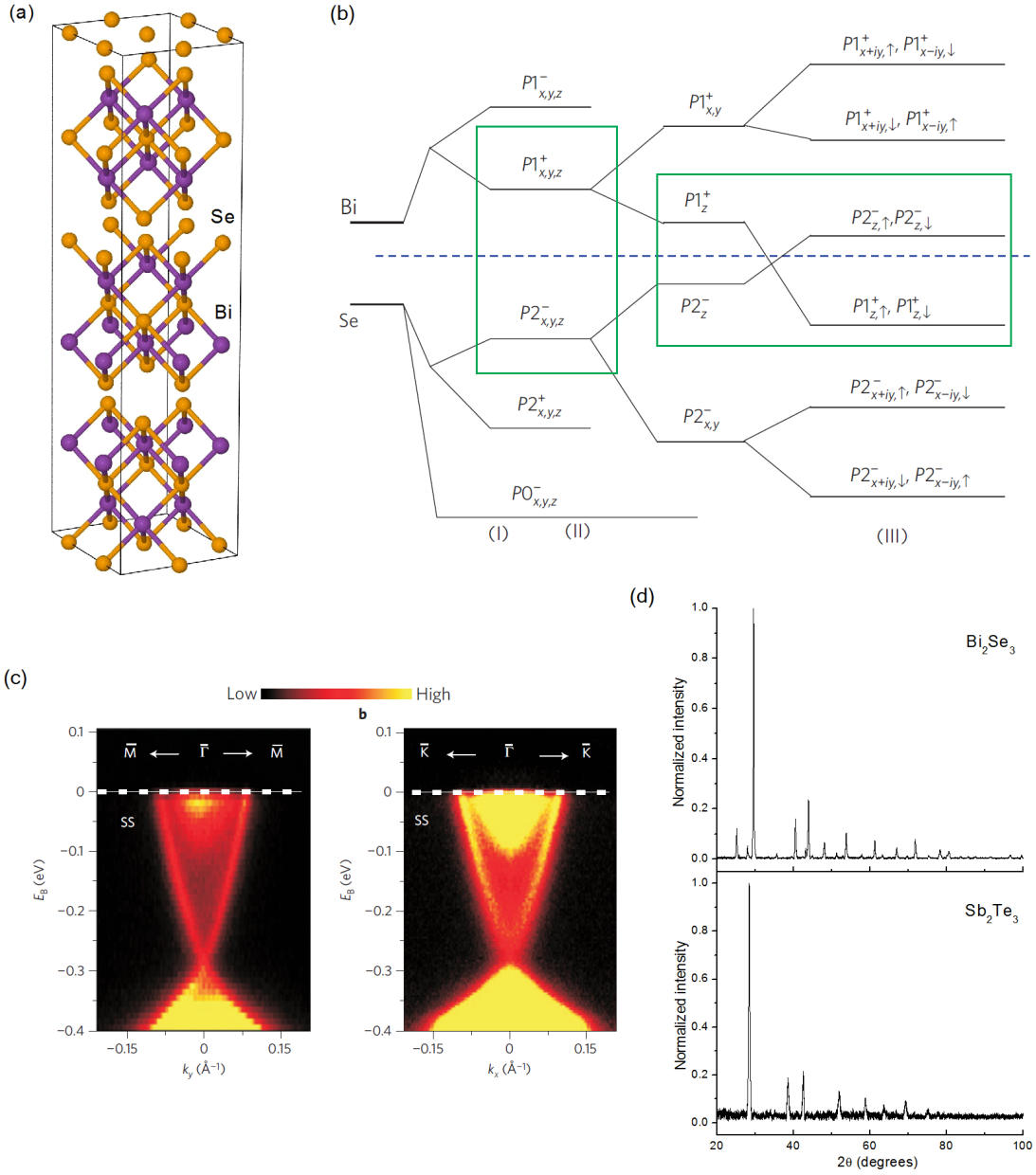

Figure 6: (a) Hexagonal unit cell of Bi_2Se_3. The distance between two nearest Se atoms of the two adjacent Se layers is larger than the sum of their covalent radii. As a result, the Se-Bi-Se-Bi-Se quintuple layers are hold together by weak van der Waals force. (b) (adapted from Ref. [123]) Schematic diagram of the evolution from the atomic $p_{x,y,z}$ orbitals of Bi and Se into the conduction and valence bands of Bi_2Se_3 at the Γ point of the Brillouin zone. The three different stages (I), (II) and (III) represent the effect of turning on chemical bonding, crystal-field splitting and SOC, respectively. (c) (adapted from Ref. [114]) High-resolution angel-resolved photoemission spectroscopy measurements of surface electronic band dispersion on $Bi_2Se_3(111)$. (d) XRD spectrum of Bi_2Se_3 and Sb_2Te_3 at 10 K. Maximum peak intensity is normalized to 1.

2.2 Thermal expansion of Bi_2Se_3 and Sb_2Te_3 crystals

The $Bi(Sb)_2Se(Te)_3$ family compounds were under extensive studies in 1950s and 1960s as excellent thermoelectric materials. However, some basic physical properties still remain unexplored. For this reason, we digress from the main topic of the dissertation in this section and the next section. In this section, we present the measurements of the linear thermal expansion coefficients of Bi_2Se_3 and Sb_2Te_3 crystals using XRD [15]. In the next section, we present the measurement of the temperature dependence of optical phonons in the same materials using Raman spectroscopy [50]. We collaborate with Dr. Haidong Zhou in the XRD measurements, and Dr. Dmitry Smirnov in the Raman studies. Both measurements were performed at the National High Magnetic Field Laboratory (NHMFL) at Tallahassee, FL.

Thermal expansion is the tendency of materials to change in size and shape as they heat and cool. It is essential to device design and engineering, as the induced strain could cause the deformation of the device and affect its phonon dynamics. In addition, the knowledge of thermal expansion coefficients is necessary for the directional growth of TI crystals and the understanding of the high thermoelectric efficiency [79]. In our work, the XRD patterns were recorded using a Huber G670 imaging-plate Guinier camera equipped with a Ge monochromator and Cu $K_{\alpha 1}$ radiation (1.54059 Å). Data were collected in steps of 0.005° in a wide temperature range from 10 K to 270 K. The lattice parameters were calculated via WINPREP program with residual factor $0.02 < R_w < 0.03$. Typical XRD spectra of Bi_2Se_3 and Sb_2Te_3 crystals (at 10 K) are shown in Fig. 6(d). From the spectra, one can determine the lattice constant of Bi_2Se_3 (extrapolated to 0 K): $a_{\mathrm{hex}} = 4.1263$ Å and $c_{\mathrm{hex}} = 28.481$ Å, which translate to $a_{\mathrm{rho}} = 9.7880$ Å and $\alpha_{\mathrm{rho}} = 24.337°$ for the rhombohedral cell. For Sb_2Te_3, the corresponding values are $a_{\mathrm{hex}} = 4.2423$ Å, $c_{\mathrm{hex}} = 30.191$ Å, and $a_{\mathrm{rho}} = 10.357$ Å, $\alpha_{\mathrm{rho}} = 23.635°$.

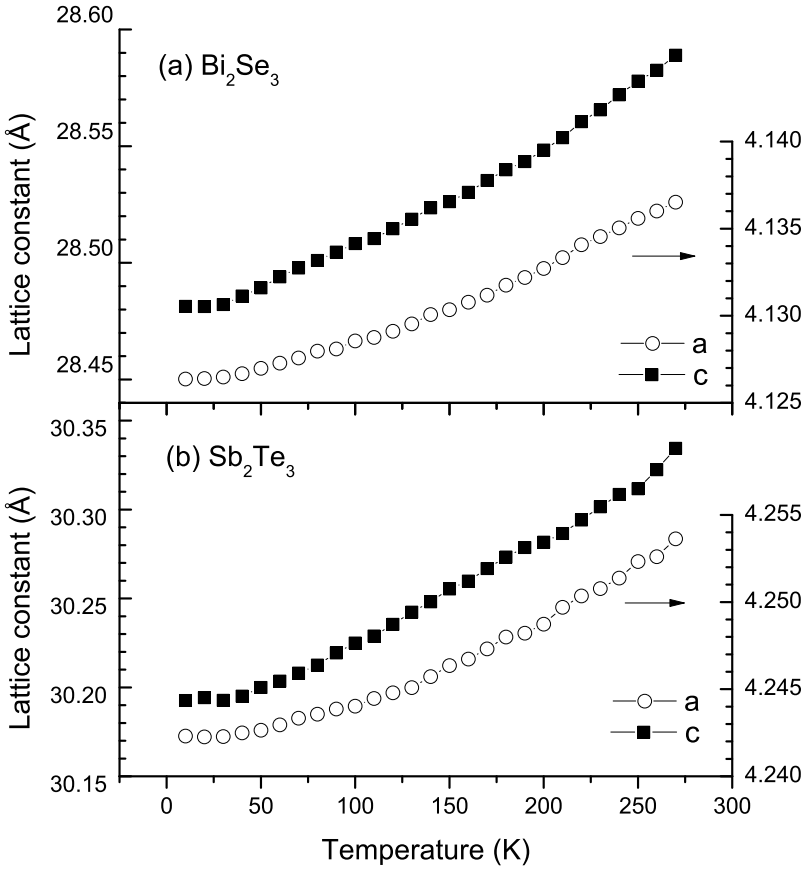

Figure 7: Lattice constant of (a) Bi_2Se_3 and (b) Sb_2Te_3 as a function of temperature.

Figure 7 plots the measured lattice parameters of Bi_2Se_3 and Sb_2Te_3 as a function of temperature, from which the linear thermal expansion coefficients (α) of the material can be derived

$$\alpha_L = \frac{1}{L}\frac{dL}{dT}, \tag{2}$$

where L is the lattice constant (i.e., $a_{\rm hex}$ or $c_{\rm hex}$), and T is the temperature. Figure 8 shows the obtained linear thermal expansion coefficients of Bi_2Se_3 and Sb_2Te_3 parallel ($\alpha_\parallel$) and perpendicular ($\alpha_\perp$) to the trigonal c-axis. Considerable anisotropy between $\alpha_\parallel$ and $\alpha_\perp$ is observed, reflective of the material bonding anisotropy. The ratio of the elastic constants C_{11}/C_{13} characterizes the anisotropy of chemical bonds; $C_{11}/C_{13} = 2.5$ for Bi_2Te_3 [69] and similar values are expected for Bi_2Se_3 and Sb_2Te_3 owing to the structural similarity and comparable Debye temperature [45]. To understand the

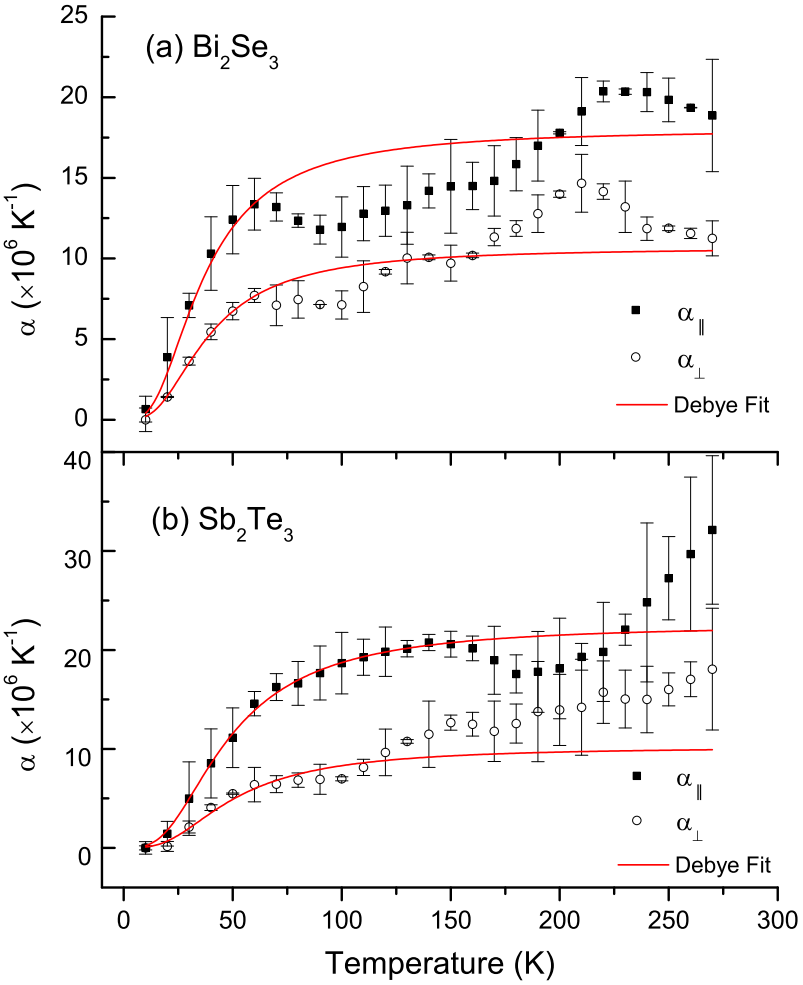

Figure 8: Linear thermal expansion coefficients of (a) Bi_2Se_3 and (b) Sb_2Te_3 as a function of temperature. Red lines represent best fits using Debye model. The data well agree with the Debye T^3 law at low temperatures, while considerable deviation is evidenced at above 150 K.

temperature dependence of $\alpha(T)$, it is instructive to introduce the Grüneisen relation

$$c_v\gamma = \kappa\beta, \tag{3}$$

where c_v is the specific heat, γ is the Grüneisen parameter, κ is the bulk modulus, and $\beta = 2\alpha_{\parallel} + \alpha_{\perp}$ is the volumetric thermal expansion coefficient. Usually, γ and κ are only weakly dependent on the temperature, indicating that the thermal expansion coefficient has the same temperature dependence as the specific heat. This relationship ($\alpha(T)$ vs. $c_v(T)$) remains valid for anisotropic materials [19], therefore we can

apply Debye model to fit our data

$$\alpha = \alpha_0(\frac{T}{\Theta_D})^3 \int_0^{\Theta_D/T} \frac{x^4 e^x dx}{(e^x-1)^2}, \quad (4)$$

where α_0 is a temperature independent fitting parameter, and Θ_D is the Debye temperature. Good agreement is achieved in the low temperature regime, as shown by the solid lines in Fig. 8, consistent with that observed in Bi_2Te_3 [7]. The obtained Debye temperature (from fitting both $\alpha_\parallel$ and $\alpha_\perp$) is $\Theta_D = 160$ K for Bi_2Se_3 and $\Theta_D = 200$ K for Sb_2Te_3, close to the literature values (182 K and 160 K, respectively) [69]. At above 150 K, the experimental results deviate from the Debye model. Similar anomalous behavior is also evident in Bi_2Te_3 [26], but the origin is not conclusive [7]. There are two possible explanations: (1) This is due to higher-order anharmonic effects. Generally, the anharmonicity of the bonding forces in a crystal is characterized by the Grüneisen parameter. Higher-order anharmonic effects may lead to a nontrivial temperature dependence $\gamma(T)$, giving rise to anomalous $\alpha_\parallel(T)$ and $\alpha_\perp(T)$ through the Grüneisen relation. This scenario is used to explain the thermal expansion of tellurium [44, 33] and Bi_2Te_3 [79]. (2) The deviation could be due to the breaking of the van der Waals bond between two Se-Se (Te-Te) layers, as proposed in Ref. [79] and [26] for Bi_2Te_3. The van der Waals binding energy is typically in the range of 0.4-4 kJ/mole, while the energy of thermal motion at room temperature is about 2.5 kJ/mole, suggesting that the degradation of the van der Waals bond may cause the anomaly in $\alpha(T)$ at levitated temperatures. These two reasons may also explain the differences in $\alpha(T)$ between Bi_2Se_3 and Sb_2Te_3, but further experimental and theoretical work is needed to fully understand it.

Finally, we summarize the room temperature thermal expansion parameters of Bi_2Se_3, Sb_2Te_3 and Bi_2Te_3 in Table 1, as a reference for future study of TIs and device engineering. The thermal expansion coefficients for Bi_2Se_3 and Sb_2Te_3 are taken from Fig. 8, which are in good agreement with the values documented in the materials handbook [69]. Grüneisen parameters are calculated from Eqn. 3. Specific

Table 1: Room temperature thermal expansion coefficient and Grüneisen parameter for Bi_2Se_3, Sb_2Te_3 (at 270K) and Bi_2Te_3 (at room temperature)

	$\alpha_\parallel$ ($\times 10^{-5}$ K^{-1})	$\alpha_\perp$ ($\times 10^{-5}$ K^{-1})	β ($\times 10^{-5}$ K^{-1})	c_p (J/K/mol)	κ (GPa)	γ
Bi_2Se_3	1.9 ± 0.3	1.1 ± 0.1	4.1	124.3[69]	48.4[99]	1.4
Sb_2Te_3	3.2 ± 0.7	1.8 ± 0.6	6.8	128.8[69]	44.8[49]	2.3
Bi_2Te_3	2.1[69]	1.4[69]	4.9	124.4[72]	37.4[45]	1.5[45]

heat at constant pressure (c_p) of the materials is better documented in the literature, and thus used in the calculation (The difference between c_p and c_v is negligible, compared with the uncertainty of our measurements). For Bi_2Te_3 the values are extracted from various previous works.

2.3 Raman-active optical phonons in Bi_2Se_3 and Sb_2Te_3 crystals

Phonons are the collective excitations in the periodic, elastic arrangement of atoms. It is an abstract description of the quantized vibrational mode in the crystal lattice. It is essential to understand the dynamics of phonons in TI materials, particularly the phonon-phonon and electron-phonon interactions, in order to achieve the best device performance. Raman spectroscopy proves to be a powerful tool in exploring phonon dynamics in new materials. In Raman measurements, a monochromatic light, usually laser, is incident on the material and interacts with the phonons, causing a shift in energy of the reflected photons. Valuable information about the phonons in the material can be extracted from the Raman shift.

The study of optical phonons in Bi_2Se_3 and Sb_2Te_3 by Raman spectroscopy have been well documented in the literature [86, 87], but only at room temperature. Accurate measurements of the temperature dependence of the phonons are still lacking. In collaboration with Dr. Dmitry Smirnov's group at the NHMFL, we measure the temperature dependent Raman spectra in a backscattering geometry. The wavelength of the laser light is 532 nm and the focal spot size is about 20 μm in diameter. During

the measurement, the laser was sent into an optical fiber that guides the excitation to the sample stage mounted in a helium-flow variable temperature cryostat. The scattered light collected by a f/0.73 lens was directed into a collection fiber, and then guided to a spectrometer (Princeton Instruments Trivista Triple-Stage Spectrometer) equipped with a liquid-nitrogen-cooled CCD camera. The camera is capable of acquiring signal in the spectral range from 110 to 1000 cm^{-1} with a spectral resolution of $\sim$1 cm^{-1}. The collected spectra were normalized to the background signal from a mirror to compensate for the effects of parasitic light scattering in the optical fibers. The Raman shift frequency was calibrated with reference to the spectra measured on an elemental sulfur reference sample. To correct for instrumental broadening, the peak widths were obtained following the procedure in Ref. [103]. At each measurement point, the temperature was stabilized for approximately 20 minutes to ensure accurate temperature dependent measurements. At a few temperatures the spectra were measured during both cooling down and warming up, and we found no difference in the spectra within the experimental uncertainty.

Bi_2Se_3 and Sb_2Te_3 have 12 optical phonons, out of which four modes are Raman active, $2E_g + 2A_{1g}$, and the corresponding frequencies are $\sim$30-200 cm^{-1} [86, 87]. We show the room temperature Raman spectra at different excitation power levels in Fig. 9. For Bi_2Se_3, the high frequency E_g^2 and A_{1g}^2 modes are detected at 131.5 cm^{-1} and 175.5 cm^{-1}, respectively. For Sb_2Te_3, the E_g^2 phonon frequency is at the low-frequency onset of the apparatus, so only the A_{1g}^2 mode at 168.8 cm^{-1} is detectable. It is worth noting that care needs be taken with the excitation power to avoid burning the crystal surface. We find the higher limit is $\sim 10^3$ W/cm^2 for the Raman peaks to be insensitive to the power level. All the temperature dependent spectra presented below were obtained at power densities of 670 W/cm^2 or less.

We show the typical Raman spectra measured at different temperatures between 300 K and 5 K in Fig. 10. For both materials, the temperature dependence of the

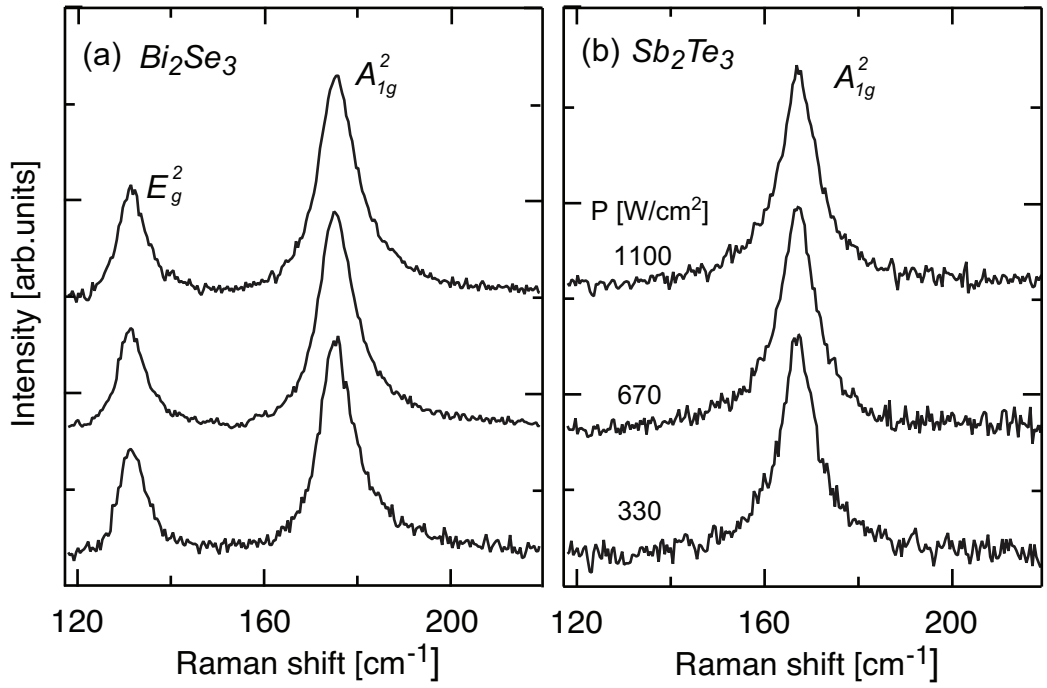

Figure 9: 300 K, background corrected Raman spectra of Bi_2Se_3 and Sb_2Te_3 measured at different excitation power levels. The spectra are shifted vertically for clarity. Adapted from Ref. [50].

phonon spectra is very similar: as the temperature decreases, the phonon peak exhibits blue shift and line narrowing. Since the peak for A_{1g}^2 phonons dominate the spectra, we will focus on the temperature dependence of this mode from here on. The peak position and FWHM of the A_{1g}^2 phonons are extracted from Lorentzian fits, and the best fits are displayed as the dashed lines in Fig. 10.

Theoretically, a second order expansion of the lattice potential in normal coordinates gives the harmonic approximation of the bare phonon frequency ω_0. Higher order anharmonic terms are useful when describing the phonon-phonon coupling. This coupling causes renormalization of the phonon energy and lifetime, assuming the decay of zone-center optical phonon into two or more acoustic phonons. In the simplest case, the optical phonon decays into two phonons with equal energies and opposite momenta. This is the so-called symmetrical three-phonon coupling model [57], and it has been shown to provide a fairly accurate description of the phonon

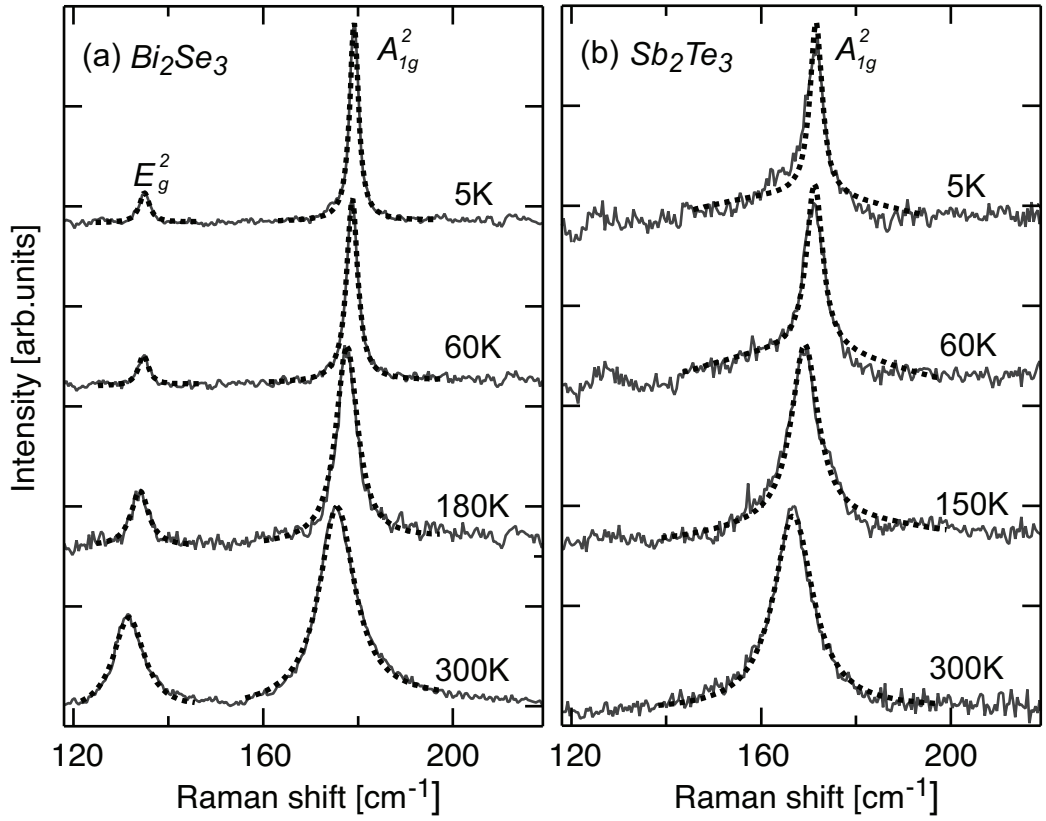

Figure 10: Background corrected, normalized Raman spectra of Bi_2Se_3 and Sb_2Te_3 measured at various temperatures. Dashed lines are Lorentzian fits to the experimental data. The spectra are shifted vertically for clarity. Adapted from Ref. [50].

temperature dependence in diamond [68]. For other materials, generalized models have been suggested, to account for anharmonic effects due to the thermal expansion and/or asymmetric decay into two or more different phonons [71, 5, 105]. The temperature dependence of the phonon frequency $\omega(T)$ is commonly expressed as

$$\omega(T) = \omega_0 + \Delta\omega^{(1)}(T) + \Delta\omega^{(2)}(T), \tag{5}$$

where ω_0 is the bare harmonic frequency, $\Delta\omega^{(1)}$ is the anharmonic, correction solely due to the thermal expansion of the crystal lattice, and $\Delta\omega^{(2)}$ is the anharmonic phonon-phonon coupling contribution. The thermal expansion contribution $\Delta\omega^{(1)}(T)$ is given by

$$\Delta\omega^{(1)}(T) = \omega_0 \left[\exp\left(-\gamma \int_0^T \left[\alpha_c(T') + 2\alpha_a(T') \right] dT' \right) - 1 \right], \tag{6}$$

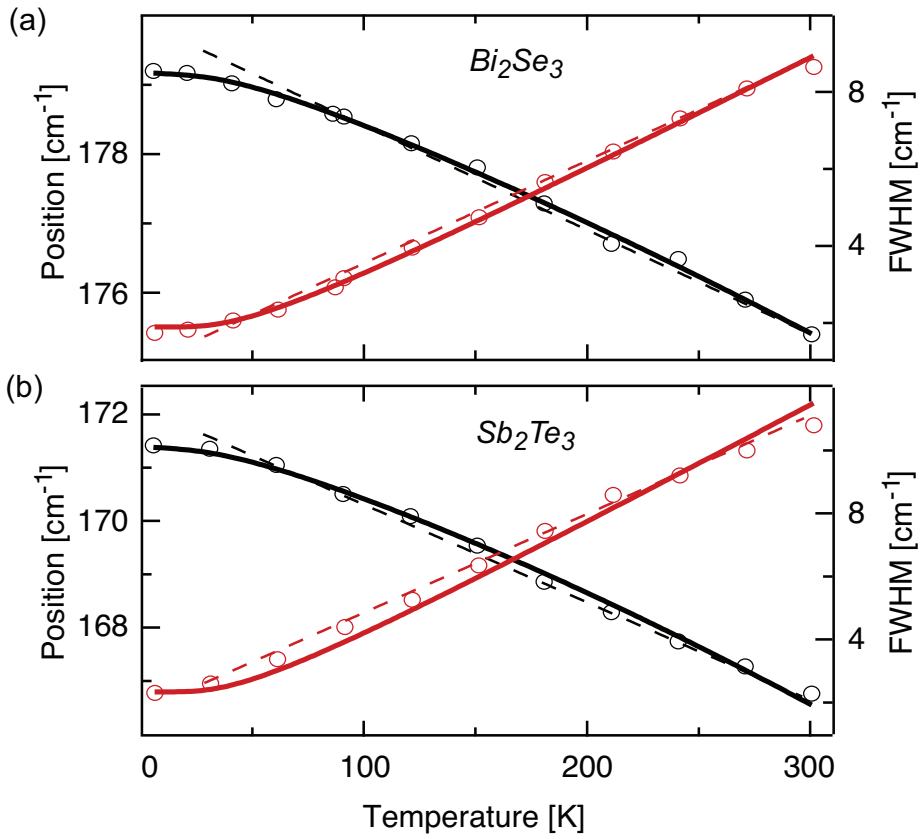

Figure 11: Temperature dependence of the A_{1g}^2 phonons in (a) Bi_2Se_3 and (b) Sb_2Te_3. Symbols are peak position (black) and linewidth (red) extracted from the experimental data. Solid lines are fits to data using the symmetrical three-phonon coupling model including thermal expansion contribution. Dashed lines are linear fits to data in the 90-300 K range. Adapted from Ref. [50].

where γ is the mode Grüneisen parameter, and $\alpha_a(T)$ and $\alpha_c(T)$ are the coefficients of linear thermal expansion along the a and c axes: $\alpha_L = \frac{1}{L}\frac{dL}{dT}$ (Eqn. 2).

Using the XRD data from the previous section, we find that the temperature dependence of lattice parameters in Bi_2Se_3 can be approximated between 10 K and 270 K with better than 0.8% accuracy by the following polynomials: $a(T) = 4.13 + 1.59\times10^{-5}T + 8.87\times10^{-8}T^2$, and $c(T) = 28.48 + 2.26\times10^{-4}T + 6.86\times10^{-7}T^2$. For Sb_2Te_3, the polynomial approximation with better than 1.5% accuracy in the same temperature range is given by: $a(T) = 4.24 + 9.3\times10^{-6}T + 1.25\times10^{-7}T^2$, and $c(T) = 30.18 + 3.5\times10^{-4}T + 7.4\times10^{-7}T^2$. Estimated Grüneisen parameters at 270 K are

1.4 for Bi_2Se_3, and 2.3 for Sb_2Te_3 (Table 1).

Analysis of the data in Fig. 11 shows that the thermal expansion contribution term $\Delta\omega^{(1)}(T)$ is responsible for ∼40% of the total phonon frequency change with temperature. Further, the observed temperature dependence can be well described within a symmetrical three-phonon coupling approximation, in which the optical phonon frequency $\omega(T)$ and linewidth $\Gamma(T)$ are modeled as

$$\omega(T) = \omega_0 + \Delta\omega^{(1)}(T) + A\left[1 + n(\omega_1) + n(\omega_2)\right], \tag{7}$$

$$\Gamma(T) = B\left[1 + n(\omega_1) + n(\omega_2)\right], \tag{8}$$

$\omega_1 = \omega_2 = \omega_0/2$, $n(\omega) = \left[\exp\left(\hbar\omega/k_BT\right) - 1\right]^{-1}$, and A and B are fitting parameters. Note that the linewidth is a function of anharmonic coupling only, but does not depend on the thermal expansion contribution. Figure 11 the best fits (solid lines) to the temperature dependent peak position and linewidth of the A_{1g}^2 phonons using Eqn. 7 and 8. Good agreement with the data is achieved.

Finally, we note that at temperatures above 90 K, there is a linear relationship between the frequency and linewidth of the A_{1g}^2 phonons and temperature. $\omega(T) = \omega_0^* + \frac{d\omega}{dT}T$, $\gamma(T) = \gamma_0^* + \frac{d\gamma}{dT}T$. The overall peak frequency change is about 4 cm^{-1} in the temperature range between 90 K and 300 K, and thus could be used as an effective local thermometer. The metrology based on the linewidth measurements could be more accurate because of the larger relative variation, though it would require the use of a high-resolution spectrometer. The extracted values of the linear fit and the symmetrical three-phonon coupling model are summarized in Table 2.

To conclude this Chapter, we have measured the thermal expansion parameters of Bi_2Se_3 and Sb_2Te_3 crystals in a wide temperature range from 10 K to 270 K. The extracted linear thermal expansion coefficients are found in consistent with the Debye model at low temperatures, but deviate at above 150 K. The result is crucial for interpreting the temperature dependent Raman shift in these materials. We find that

Table 2: Temperature dependence of the A_{1g}^2 phonons: fitting parameters using the linear model (left) and the symmetrical three-phonon coupling model (right). Adapted from Ref. [50].

	Linear fit (90-300 K)				3-phonon decay model		
	ω_0^* (cm^{-1})	$d\omega/dT$ (cm^{-1}/K)	γ_0^* (cm^{-1})	$d\gamma/dT$ (cm^{-1}/K)	ω_0 (cm^{-1})	A (cm^{-1})	B (cm^{-1})
Bi_2Se_3	179.9(6)	-0.015	0.8	0.026	179.8(8)	-0.7	1.89
Sb_2Te_3	172.2(1)	-0.018	1.62	0.031	172.1	-0.7	2.33

the evolution of the A_{1g}^2 phonons as a function of temperature can be well explained by the anharmonic decay of optical phonons and the material thermal expansion. Above 90 K, the temperature dependence of the A_{1g}^2-phonon Raman peak frequency and linewidth can be very well approximated by a linear function, thus offering a convenient thermometer in Bi_2Se_3 and Sb_2Te_3-based devices in a wide temperature range.

CHAPTER III

THEORY OF POINT CONTACT SPECTROSCOPY

Point contact spectroscopy is an experiment technique that involves using a sharp tip to probe the sample surface and measuring the conductance of the interface at different applied bias voltages. In point contact measurement, usually either the tip or the sample is superconducting, and the tip is in direct contact with the sample. This is in contrast with scanning tunneling spectroscopy, where both the tip and the sample could be non-superconducting, and there is a vacuum gap between the tip and the sample. The point contact spectroscopy has proved to be a useful tool in exploring superconducting materials, particularly unconventional superconductors [24]. It provides both the energy- and the momentum-resolved spectroscopic information at the interface of two materials (usually one is known, the other is unknown). It has been widely used in determining the pairing symmetry of p-wave and d-wave superconductors, and quantitative agreement with theory has been achieved [64, 70, 94, 21]. In this Chapter, we explore the physical process of Andreev reflection [3], which governs the point contact transport at the normal metal/ $s-$wave conventional superconductor interface. We introduce the Blonder, Tinkham, Klapwijk (BTK) model [14] that quantitatively describes the conductance spectra of the interface. We also introduce a modification to the BTK model, which deals with spin polarized currents.

3.1 Point contact Andreev reflection at normal metal/ superconductor interface

We consider a normal metal (N) (or a highly doped semiconductor) brought into direct contact with a superconductor (S). We are interested in the electronic transport properties of the N/S interface: if we apply a voltage V across the N/S interface, what

will be the current I?

According to the Bardeen, Cooper and Schrieffer (BCS) theory for superconductivity [6], a pair of electrons can be attracted to each other through the exchange of phonons. This pair of electrons is called a Cooper pair. A finite energy, or temperature, is required to break the Cooper pairs. Below the superconducting transition temperature (T_c), an energy gap (Δ) is opened up in the density of states at the Fermi surface. Only Cooper pairs can reside inside the gap, and no single particle state exists. The Cooper pairs are in superfluid state and thus conduct with no resistance.

Consider an electron incident from the normal metal to the superconductor. If the incident energy is larger than the gap ($E = eV > \Delta$), normal transmission occurs. But if the incident energy is smaller than the gap ($E < \Delta$), the electron cannot enter the gap in single particle state, so it seems transmission is prohibited. However, while studying the thermal conductivity of superconductors, Andreev [3] realized that an incident electron from the N side can pair with another electron to form a Cooper pair and travel into the superconductor. Charge must be conserved in this process, so a hole is reflected at the interface back to N. Momentum must also be conserved, so if the Cooper pair is in singlet state, the hole must trace back the path of the incident electron [8]. Intuitively then, this hole provides another conducting channel which cannot be distinguished from the electron conducting channel. As a result the electrical conductance of the N/S interface when $eV < \Delta$ should be twice as much as when $eV > \Delta$. This process is called the Andreev reflection, and is depicted in Fig. 12.

Although Andreev reflection was discovered in the 1960s, a detailed calculation of the conductance spectra was not done until 1982, when Blonder, Tinkham and Klapwijk solved the Bogoliubov-de Gennes equation at the N/S interface [14]. We shall closely explore the BTK model starting from the next section.

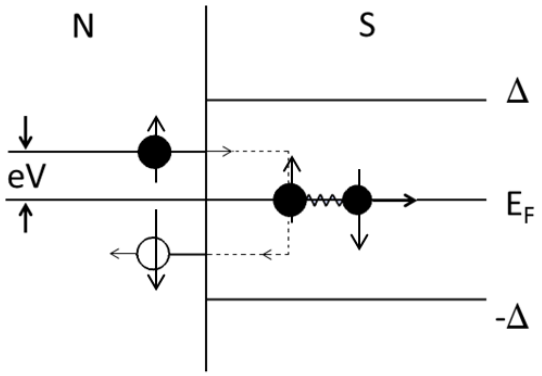

Figure 12: The Andreev reflection process at a barrierless N/S interface. For an incoming electron with energy $eV < \Delta$, a Cooper pair is formed in order to enter the superconducting gap. Charge and momentum conservation order a hole to be retro-reflected back to the normal metal. The hole provides an additional conducting channel and thus doubles the interfacial conductance. For incoming electrons with energy $E > \Delta$, normal transmission occurs.

3.2 The Blonder, Tinkham, Klapwijk model

3.2.1 Solution to the Bogoliubov-de Gennes Equation

The N/S interface system is an inhomogeneous system. A theory often used to deal with such inhomogeneous system is the Ginzburg-Landau theory. Unfortunately the Ginzbuig-Landau theory does not explicitly include quasiparticles and thus is not a microscopic theory. An microscopic approach is to use the Bogoliubov transformation to make the BCS mean-field Hamiltonian spatially dependent. The resulting Bogoliubov-de Gennes (BdG) Equation can be written as:

$$i\hbar\frac{\partial f}{\partial t} = (-\frac{\hbar^2\nabla^2}{2m} - \mu(x) + V(x))f(x,t) + \Delta(x)g(x,t), \tag{9a}$$

$$i\hbar\frac{\partial g}{\partial t} = -(\frac{\hbar^2\nabla^2}{2m} - \mu(x) + V(x))g(x,t) + \Delta(x)f(x,t), \tag{9b}$$

where m is the electron mass, $\Delta(x)$ is the energy gap and $\mu(x)$ is the chemical potential, which, for the BCS superconductor is equal to the Fermi energy E_F. $f(x,t)$ and $g(x,t)$ are the wave functions for electron-like and hole-like quasiparticles, respectively. It is easy to see that $f(x,t)$ and $g(x,t)$ are time reversal symmetric when $\Delta = 0$. In this case, Eqn. 9a and Eqn. 9b are no more than the Schrödinger equations

for electrons and holes.

When $\Delta \neq 0$, Eqn. 9a and Eqn. 9b are coupled. Blonder, Tinkham and Klapwijk [14] proposed a simple model that solves the BdG equation at N/S interface. Specifically, BTK considers the simplest case where $\Delta(x)$ is a constant in S and there is no external potential $V(x)$. In such a case the plane wave trial solution can be used ($\tilde{u}$ and $\tilde{v}$ are normalizing coefficients):

$$f = \tilde{u}e^{ikx - iEt/\hbar}, \tag{10a}$$

$$g = \tilde{v}e^{ikx - iEt/\hbar}. \tag{10b}$$

The BdG equation then becomes:

$$E\tilde{u} = (\frac{\hbar^2\nabla^2}{2m} - E_F)\tilde{u} + \tilde{v}, \tag{11a}$$

$$E\tilde{v} = -(\frac{\hbar^2\nabla^2}{2m} - E_F)\tilde{v} + \tilde{u}. \tag{11b}$$

Solving for E we get

$$E^2 = (\frac{\hbar^2k^2}{2m} - E_F)^2 + \Delta^2. \tag{12}$$

This is the dispersion relation which gives the functional relation between energy E and crystal momentum k. This dispersion relation is plotted in Fig. 13. We can see that there is an energy gap of size Δ, and inside the gap there is no quasiparticle states, while outside the gap there are four quasiparticles for a given energy E, marked as $\pm k^+$ and $\pm k^-$. $k^\pm$ is defined as

$$\hbar k^\pm = \sqrt{2m}[E_F \pm (E^2 - \Delta^2)^{1/2}]^{1/2}, \tag{13}$$

and we also define

$$u_0^2 = \frac{1}{2}[1 + \frac{(E^2 - \Delta^2)^{1/2}}{E}] = 1 - v_0^2. \tag{14}$$

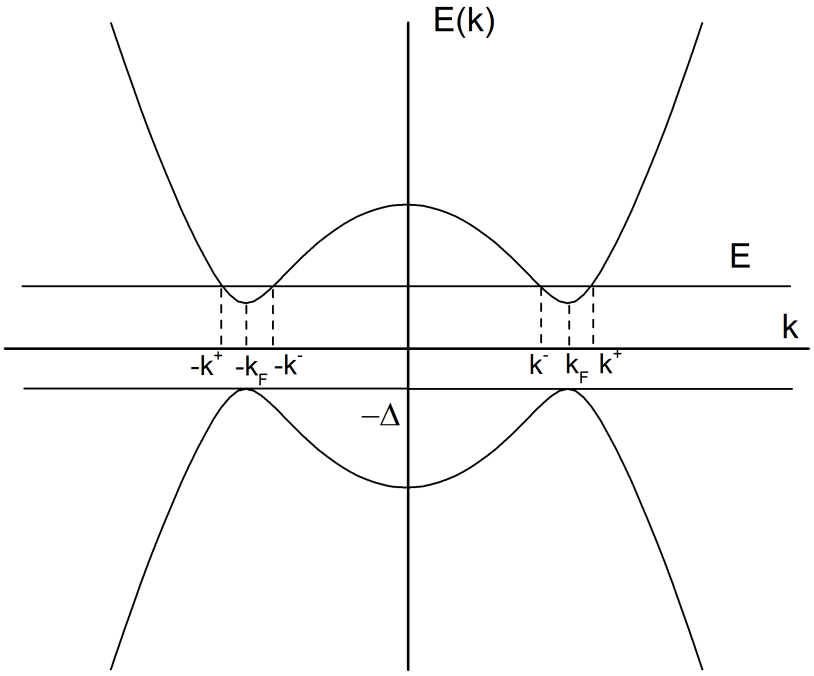

Figure 13: Band structure of a superconductor under the BTK model: $E(k) = \pm\sqrt{(\hbar^2k^2/2m - E_F)^2 + \Delta^2}$. For $E > \Delta$ the four quasiparticle states are marked in the figure at $\pm k^+$ and $\pm k^-$. In this figure $E_F/\Delta = 10$. This ratio is much larger in a realistic system but does not change the shape of the band structure qualitatively.

The BTK solution to the BdG equation then becomes

$$\Psi_{\pm k^+} = \begin{pmatrix} u_0 \\ v_0 \end{pmatrix} e^{\pm ik^+x}, \tag{15a}$$

$$\Psi_{\pm k^-} = \begin{pmatrix} v_0 \\ u_0 \end{pmatrix} e^{\pm ik^-x}. \tag{15b}$$

Our next task is to pick appropriate boundary conditions to match the solution on the N side to the solution on the S side.

3.2.2 Matching conditions at the N/S interface

BTK assumes that there is only elastic scattering at the N/S interface, and models the interfacial potential as a Dirac delta function with strength H (i.e. $V(x) = H\delta(x)$). The reflection and transmission process at the interface when $E > \Delta$ is depicted in Fig. 14. Here, we consider an electron incident from the $-x$ direction (state "0"

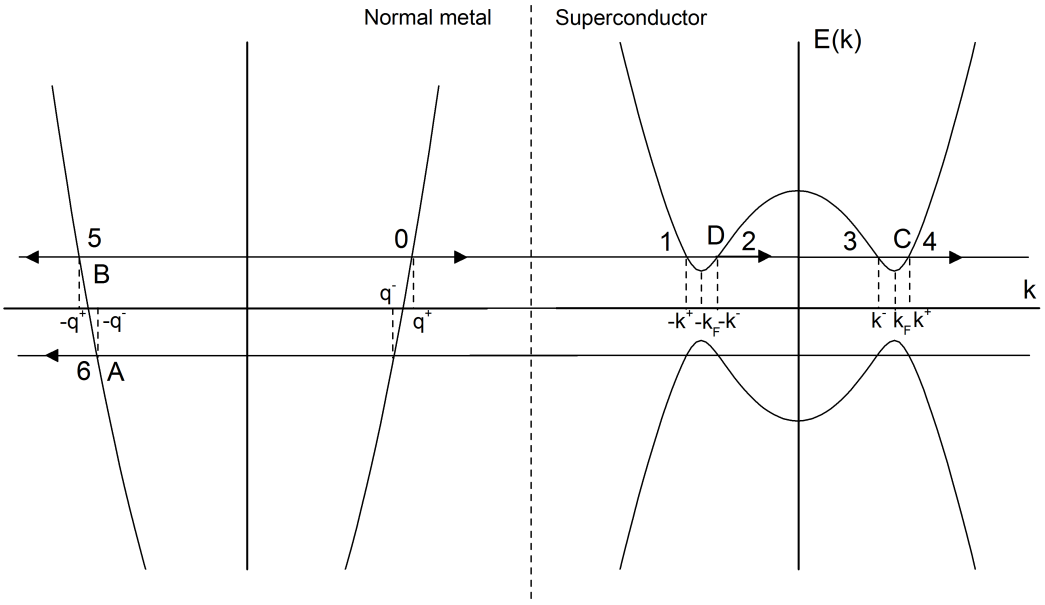

Figure 14: Scattering process at N/S interface when incident energy E is larger than the superconducting gap Δ. The incident electron is marked as "0". There are six possible quasiparticle states, marked at "1" to "6". To have the correct direction of group velocity, the possible transmitted states are "2" and "4", and possible reflected states are "5" and "6". The corresponding probability currents are denoted as A, B, C, and D. Note that state "6" is a hole, and represents the Andreev reflection. After Ref. [14].

in Fig. 14). The group velocity is defined as $\partial E/\partial k$; the transmitted particles are expected to have group velocity of the same sign as the incident electron, while the reflected particles have group velocity of the opposite sign. So possible transmitted states are "4", which is normal transmission without crossing the Fermi surface, and "2", which crosses the Fermi surface. Possible reflected states are "5", which is normal reflection, and "6", which is the Andreev reflection. The wave functions for the scattering process can be summarized as

$$\Psi_{inc} = \begin{pmatrix} 1 \\ 0 \end{pmatrix} e^{iq^+x},$$

$$\Psi_{refl} = a \begin{pmatrix} 0 \\ 1 \end{pmatrix} e^{iq^-x} + b \begin{pmatrix} 1 \\ 0 \end{pmatrix} e^{-iq^+x},$$

$$\Psi_{trans} = c \begin{pmatrix} u_0 \\ v_0 \end{pmatrix} e^{ik^+x} + d \begin{pmatrix} v_0 \\ u_0 \end{pmatrix} e^{-ik^-x}, \tag{16}$$

where $\hbar q^{\pm} = \sqrt{2m(E_f \pm E)}$ is the wave vector in the normal metal. The boundary condition for the Dirac potential is given by

$$\Psi_{inc}(0) + \Psi_{refl}(0) = \Psi_{trans}(0), \tag{17a}$$

$$\frac{\hbar^2}{2m}(\Psi'_{trans}(0) - \Psi'_{inc}(0) - \Psi'_{refl}(0)) = H\Psi(0), \tag{17b}$$

where Eqn. 17a ensures the continuity of wave function at $x = 0$ and Eqn. 17b is the boundary condition for derivatives of wave functions for a Dirac delta potential.

The BTK model assumes small quasiparticle excitations so that $k^+ = k^- = q^+ = q^- = k_F$. In this case, by plugging Eqn. 16 into the boundary conditions, we get the solution:

$$a = \frac{u_0 v_0}{\gamma}, \tag{18a}$$

$$b = -\frac{(u_0^2 - v_0^2)(Z^2 + iZ)}{\gamma}, \tag{18b}$$

$$c = \frac{u_0(1 - iZ)}{\gamma}, \tag{18c}$$

$$d = \frac{iv_0 Z}{\gamma}, \tag{18d}$$

where the dimensionless parameter Z is defined as $Z = H/\hbar v_F$ and γ is defined as $\gamma = u_0^2 + (u_0^2 - v_0^2)Z^2$. Note that the parameter Z is directly proportional to the interface barrier strength H. In the limit of $Z = 0$, we find that $b = 0$. Physically, this means there are no electrons reflected, and all reflection is Andreev reflection.

Table 3: Summary of the transmission and reflection probability currents obtained from the BTK model. A is the probability of Andreev reflection, B of ordinary reflection, C of transmission without crossing the Fermi surface, and D of transmission with crossing the Fermi surface. $\gamma^2 = [u_0^2 + Z^2(u_0^2 - v_0^2)]^2, u_0^2 = 1 - v_0^2 = \frac{1}{2}1 + [(E^2 - \Delta^2)/E^2]^{1/2}$. After Ref. [14].

	A	B	C	D
Normal state	0	$\frac{Z^2}{1+Z^2}$	$\frac{1}{1+Z^2}$	0
Superconducting				
$E < \Delta$	$\frac{\Delta^2}{E^2+(\Delta^2-E^2)(1+2Z^2)^2}$	$1 - A$	0	0
$E > \Delta$	$\frac{u_0^2 v_0^2}{\gamma^2}$	$\frac{(u_0^2-v_0^2)Z^2(Z^2+1)}{\gamma^2}$	$\frac{u_0^2(u_0^2-v_0^2)(1+Z^2)}{\gamma^2}$	$\frac{v_0^2(u_0^2-v_0^2)Z^2}{\gamma^2}$
No barrier (Z=0)				
$E < \Delta$	1	0	0	0
$E > \Delta$	v_0^2/u_0^2	0	$1 - A$	0
Strong barrier $(Z^2(u^2 - v^2) \gg 1)$				
$E < \Delta$	$\frac{\Delta^2}{4Z^2(\Delta^2-E^2)}$	$1 - A$	0	0
$E > \Delta$	$\frac{u_0^2 v_0^2}{Z^4(u_0^2-v_0^2)^2}$	$1 - \frac{1}{Z^2(u_0^2-v_0^2)}$	$\frac{u_0^2}{Z^2(u_0^2-v_0^2)}$	$\frac{v_0^2}{Z^2(u_0^2-v_0^2)}$

The transmission and reflection probability currents can be calculated from the coefficients above. We have:

$$A = a^* a = \frac{u_0^2 v_0^2}{\gamma^2}, \tag{19}$$

$$B = b^* b = \frac{(u_0^2 - v_0^2) Z^2 (Z^2 + 1)}{\gamma^2}, \tag{20}$$

$$C = c^* c (u_0^2 - v_0^2) = \frac{u_0^2 (u_0^2 - v_0^2)(1 + Z^2)}{\gamma^2}, \tag{21}$$

$$D = d^* d (u_0^2 - v_0^2) = \frac{v_0^2 (u_0^2 - v_0^2) Z^2}{\gamma^2}, \tag{22}$$

Turning to the case where the incident electron energy $E < \Delta$, since there is no quasiparticle states within the gap, we have $C = D = 0$. A and B can be calculated in a similar manner as above, and the result is

$$A = \frac{\Delta^2}{E^2 + (\Delta^2 - E^2)(1 + 2Z^2)^2} = 1 - B. \tag{23}$$

The probability currents we obtained in this subsection are important for all numerical calculations using the BTK model. For this reason we summarize the results in Table 3.

3.2.3 Conductance spectra at the N/S interface

After getting the probability currents (19) to (22), the final step is to calculate the electric current, which is a measureable physical quantity. When a voltage is applied, the quasiparticle system is not in equilibrium, which means we need to find the self-consistent solution to some suitable Boltzmann equation. To avoid the complexity of doing so, BTK argues that in a point contact measurement, electrons travel ballistically from the normal metal to the superconductor, so that electrons on either side is described by the *equilibrium* Fermi-Dirac distribution. This argument is explained in Fig. 15. In the ballistic regime, the contact radius is much less than the electron mean free path. The electron will then flow without scattering and gain a kinetic energy of eV through the contact.

In mathematical terms, the distribution function for electrons on the S side is $f_0(E)$, and that for the electrons on the N side is $f_0(E - eV)$, where $f_0(E) = 1/(e^{(E-E_F)/kT)} + 1)$ is the Fermi-Dirac distribution. The current can then be calculated as

$$\begin{aligned} I =& 2N(0)ev_F S \int_{-\infty}^{+\infty} f(E)dE \\ =& 2N(0)ev_F S \int_{-\infty}^{+\infty} [f_0(E-eV) - \\ & (A(1-f_0(E-eV)) + Bf_0(E-eV) + (C+D)f_0(E)]dE \\ =& 2N(0)ev_F S \int_{-\infty}^{+\infty} [f_0(E-eV) - f_0(E)][1+A-B]dE. \end{aligned} \tag{24}$$

In the above equation, S is the cross section area of the contact, $N(0)$ is the one spin density of state, and v_F is the Fermi velocity. In the derivation we used the properties that $f_0(-E) = 1 - f_0(E)$ for the Andreev reflected holes and $A + B + C + D = 1$ due to conservation of probability.

Experimentally, it is usually easier to accurately measure dI/dV rather than to

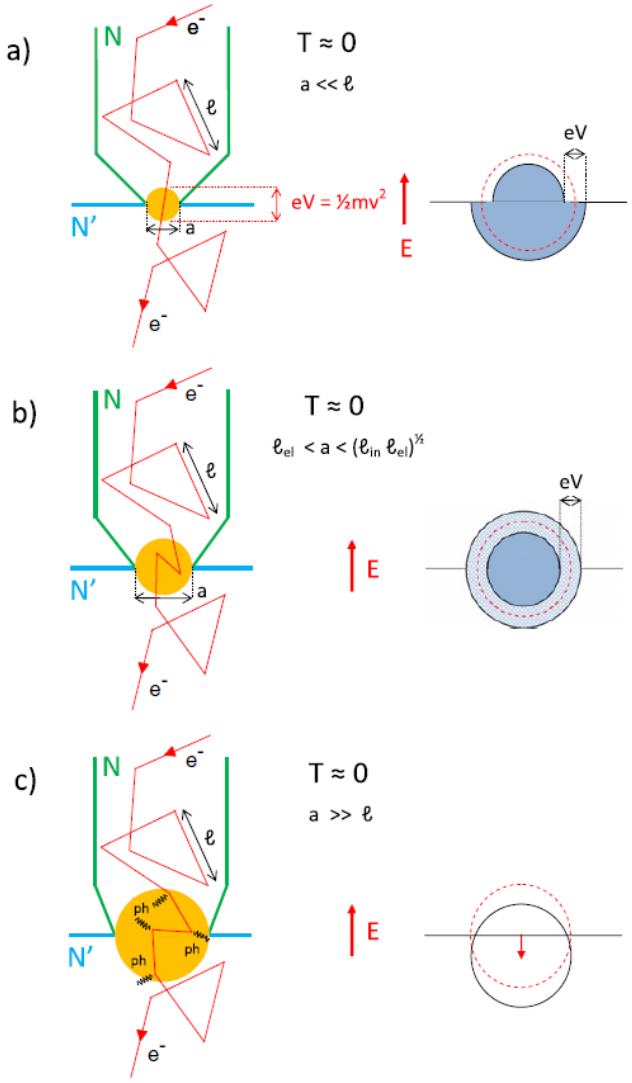

Figure 15: Regimes of conduction in a point contact. On the left side are the schematic diagrams of electrons traveling through the contact while on the right side are the electron distribution functions at the point contact. (a) In the ballistic regime, the Fermi surface is formed by two half spheres with difference in radii equals to eV. (b) In the diffusive regime, electrons are redistributed by elastic scattering events. Momentum information is lost. (c) In the thermal regime, both elastic and inelastic scattering occur, as is usual for normal transport. a represents the size of the contact, l_{el} is the mean free path for elastic scattering, and l_{in} the mean free path for inelastic scattering. Adapted from Ref. [20].

measure I directly. That is

$$\frac{dI}{dV} = 2N(0)ev_F S \int_{-\infty}^{+\infty} \frac{df_0(E-eV)}{dV}[1+A-B]dE. \tag{25}$$

To get rid of the constant coefficient in front of the integral, which is not measureable

experimentally, we normalize the conductance spectra to the normal state conductance. The normal state conductance is calculated using Eqn. 25 with $\Delta = 0$:

$$\frac{dI}{dV}_{norm} = \frac{2N(0)ev_F S}{1+Z^2}. \tag{26}$$

Finally we have the normalized conductance as

$$dI/dV_{normalized} = (1+Z^2)\int_{-\infty}^{+\infty} \frac{df_0(E-eV)}{dV}[1+A-B]dE. \tag{27}$$

Equation 27 should be considered as the final result of the BTK model. It can be evaluated numerically and compared to the experiment dI/dV vs. V curves. There are only three tunable parameters in Eqn. 27: the temperature T, the superconducting gap Δ, and the Z parameter which is proportional to the surface barrier strength. Since T and Δ can be determined experimentally, the only fitting parameter in Eqn. 27 is Z.

Before wrapping up this section, we give some representative plots of the conductance spectra from the BTK model. In Fig. 16, we plot the conductance spectra at different Z value on the left panel, and the corresponding transmission and reflection probabilities A, B, C and D on the right panel. The calculation is done using Eqn. 27 and the information in Table 3. We see that in the case of transparent interface ($Z = 0$), the reflection is purely Andreev, and the transmitted electron does not cross the Fermi surface. In the limit of strong surface barrier ($Z^2(u^2 - v^2) \gg 1$), there is no Andreev reflection and we have a quantum tunneling process.

In Fig. 17, we show the conductance spectra at different temperatures. Higher temperature smears out the features in the conductance curve. A temperature lower than 0.2 times the superconducting transition temperature T_c is favored, in order to observe all features of the conductance spectra.

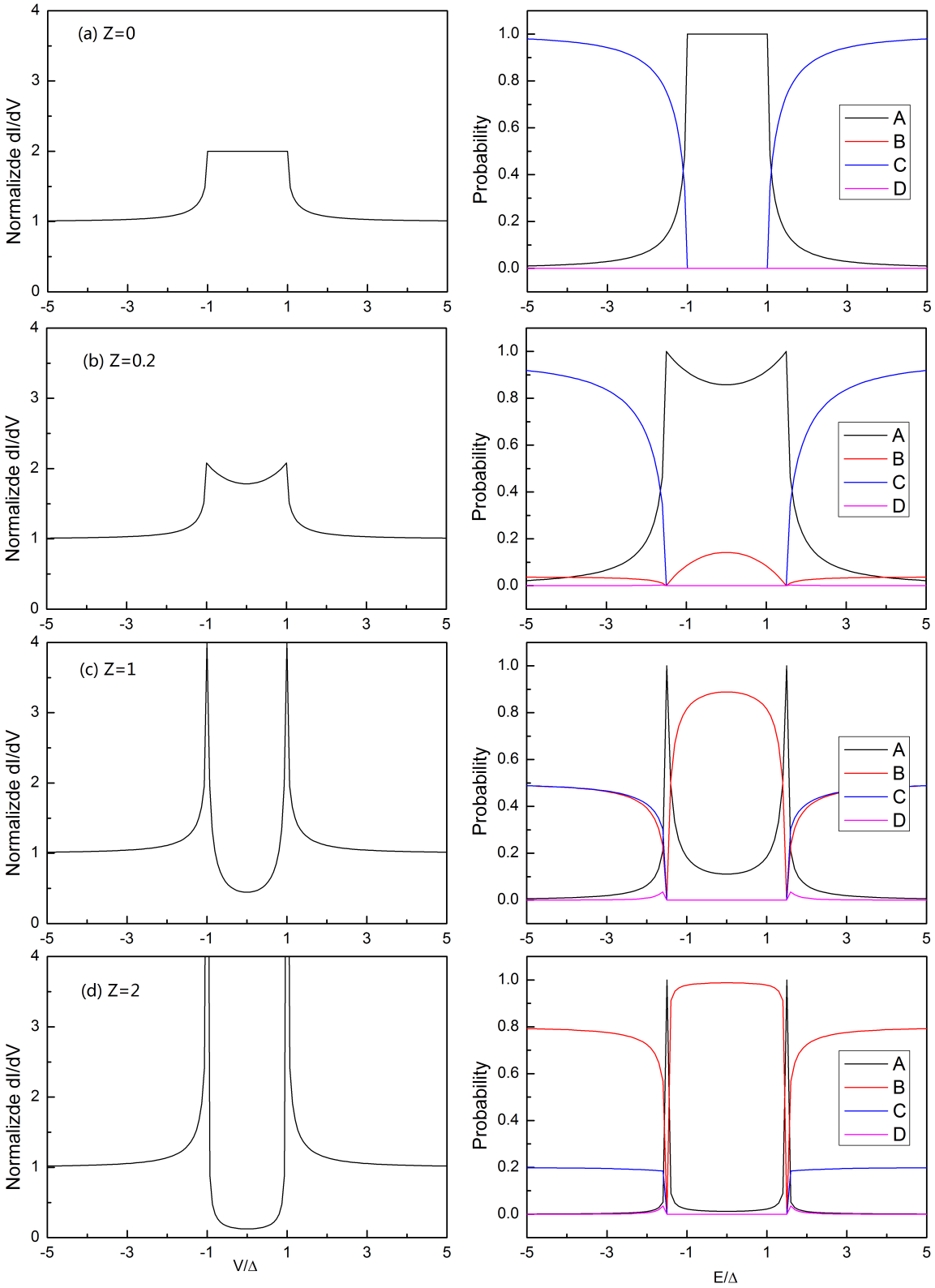

Figure 16: Left panel: normalized conductance spectra calculated using the BTK model at N/S interface, from (a) $Z = 0$ to (d) $Z = 2$. Right panel: corresponding transmission and reflection probabilities.

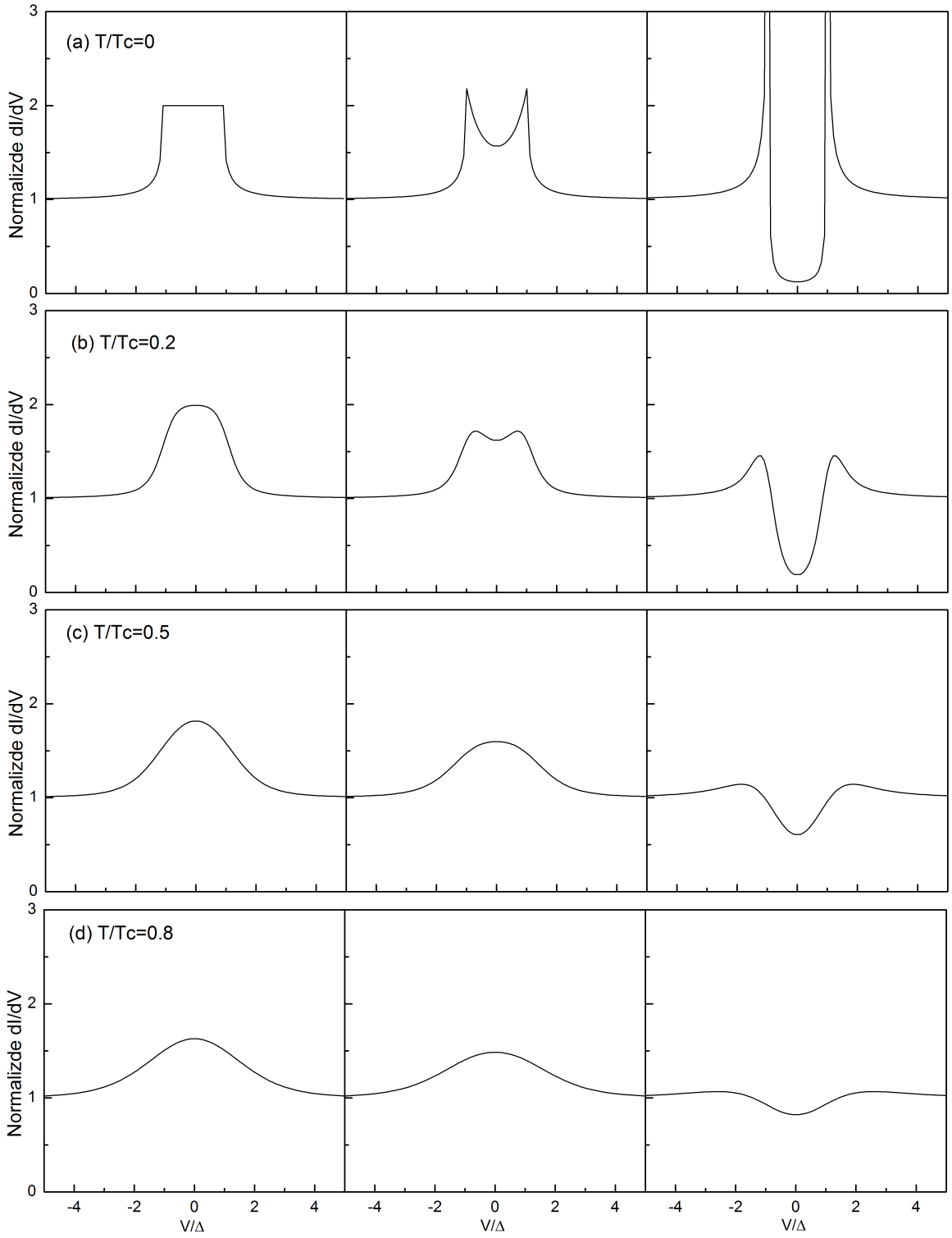

Figure 17: Temperature dependence of the normalized conductance spectra calculated using the BTK model at N/S interface. Left: Z=0, center: Z=0.3, right: Z=2. The ratio of temperature to the superconducting transition temperature T/T_c is (a) 0, (b) 0.2, (c) 0.5, and (d) 0.8.

3.3 Quasiparticle life time correction to the BTK model

The BTK model explains some simple experiments very well [13], but it often predicts much sharper features than experimentally observed. This is because the BTK model only considers elastic scattering at the N/S interface, but in reality there is also inelastic scattering happening at the interface, sometime due to the presence of an oxidation layer. A widely adopted way to incorporate inelastic scattering to the BTK model was proposed by Plecenik and coworkers [81]. They added an inelastic scattering term in the expression for quasiparticle wave function in the BdG equation:

$$i\hbar\left(\frac{\partial f(x,t)}{\partial t}\right) = i\hbar\left(\frac{\partial f(x,t)}{\partial t}\right)_{field} + i\hbar\left(\frac{\partial f(x,t)}{\partial t}\right)_{inelastic}, \tag{28}$$

and treated the inelastic scattering as the following:

$$i\hbar\left(\frac{\partial f(x,t)}{\partial t}\right)_{inelastic} = -\frac{i\hbar}{\tau}f(x,t), \tag{29}$$

where τ is the lifetime of the quasiparticles between collisions. A similar set of equations is used for $g(x)$ too. The larger Γ is, the shorter τ is, meaning that the interface is more disordered and more inelastic scattering is happening. With a substitution $\Gamma = \hbar/\tau$, the BdG equation becomes

$$\begin{aligned} i\hbar\frac{\partial f}{\partial t} &= (-\frac{\hbar^2\nabla^2}{2m} - \mu(x) + i\Gamma + V(x))f(x,t) + \Delta(x)g(x,t), \\ i\hbar\frac{\partial g}{\partial t} &= -(\frac{\hbar^2\nabla^2}{2m} - \mu(x) - i\Gamma - V(x))g(x,t) + \Delta(x)f(x,t). \end{aligned} \tag{30}$$

The BdG coherence factors u_0 and v_0 can be solved as the following (compared to Eqn. 14):

$$u_0^2 = \frac{1}{2}[1 + \frac{[(E+i\Gamma)^2 - \Delta^2]^{1/2}}{E+i\Gamma}] = 1 - v_0^2. \tag{31}$$

The BCS quasiparticle density of states in this case is

$$N(E,\Gamma) = \mathrm{Re}[\frac{E+i\Gamma}{\sqrt{(E+i\Gamma)^2 - \Delta^2}}]. \tag{32}$$

Here, the only modification to the standard BTK model is that the energy now has an imaginary part ($E \to E + i\Gamma$). There is no need to modify the expressions for A, B, C, and D, so computationally this modification is very easy to implement.

We plot some representative results of the BTK model with the quasiparticle life time correction in Fig. 18. We can see that as the ratio of Γ/Δ gets larger, the amplitude of the conductance gets smaller, and the spectra become more spread in energy. This effect cannot be reproduced by the standard BTK model under any combination of parameters. Experimentally, it is common to have $\Gamma/\Delta < 0.5$, although wide gap distribution sometimes occur and a large ratio of $\Gamma/\Delta \sim 1$ is needed.

3.4 Spin polarized BTK model

As described in Chapter 1, the spin and momentum is locked on the surface of a topological insulator. Consider a point contact measurement using topological insulator as the normal metal, and a superconducting tip. If the bulk of the TI is truly insulating (ideal case), the electron current would only flow to the ground connected to the TI surface. The current have a definite momentum direction, thus should be spin polarized. If the TI is doped, then part of the current will flow through the bulk, and the current becomes partially spin polarized. For this reason it is relevant to explore an extension to the standard BTK model that considers spin polarized current. This is our task for this section.

Consider a half-metal/S interface (Fig. 19). Electrons at the Fermi surface of a half-metal have only one spin direction; the density of states for the other spin direction is zero. Because a Cooper pair can only be formed by two electrons of opposite spins, the electrons in the half-metal cannot enter the superconducting gap as Cooper pairs. The Andreev reflection process is completely prohibited in this case, and the conductance of the interface when the applied voltage is within the gap is zero. This is in contrast to the case of N/S interface we discussed in Section 3.1, where the conductance within the gap is doubled comparing to the normal state.

Since polarized and unpolarized current undergo different physics processes, for

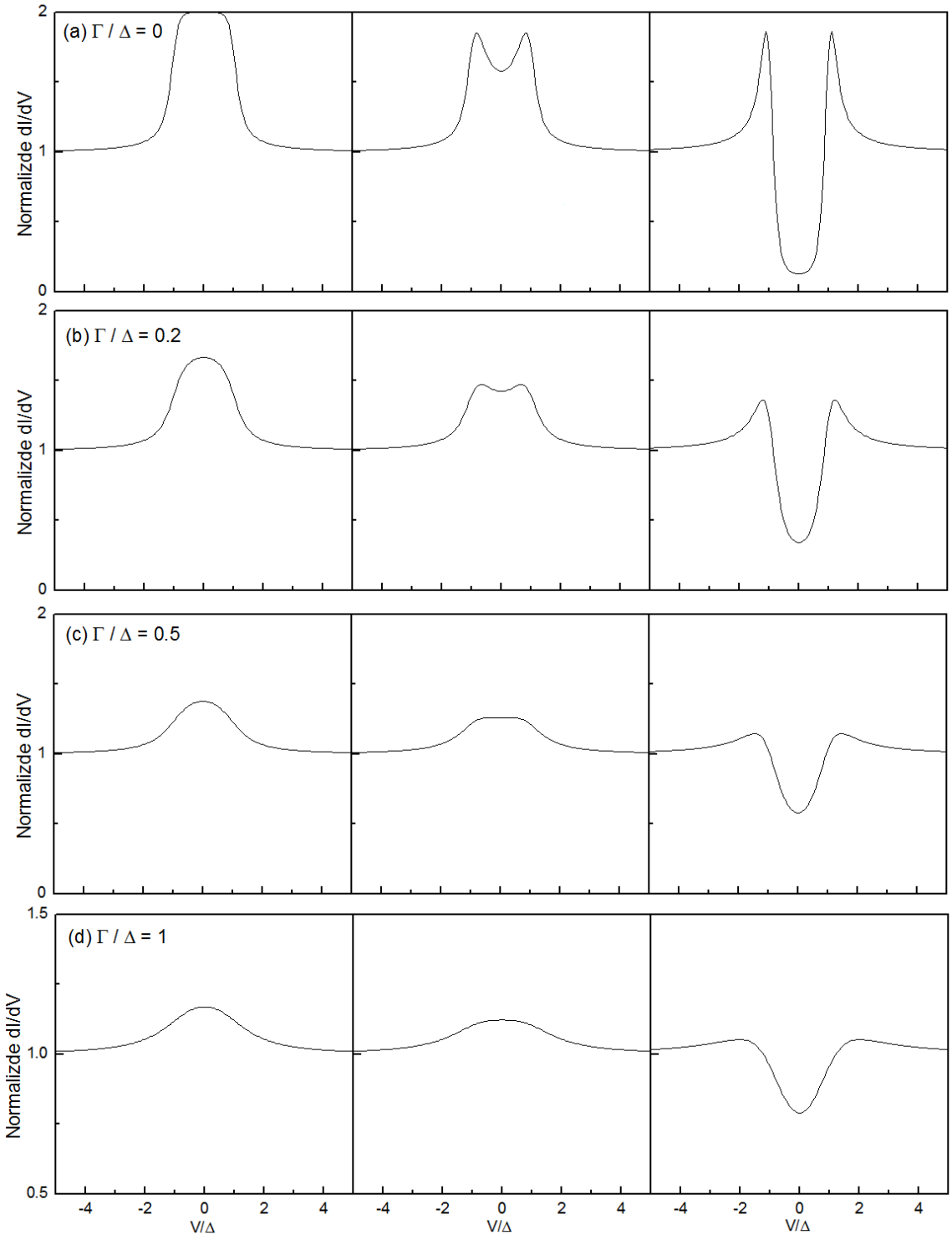

Figure 18: The normalized conductance spectra calculated using the BTK model with quasiparticle lifetime correction. Left: Z=0, center: Z=0.3, right: Z=2. The ratio of Γ/Δ is (a) 0, (b) 0.2, (c) 0.5, and (d) 1. The temperature in these plots is fixed at $k_BT/\Delta = 0.1$.

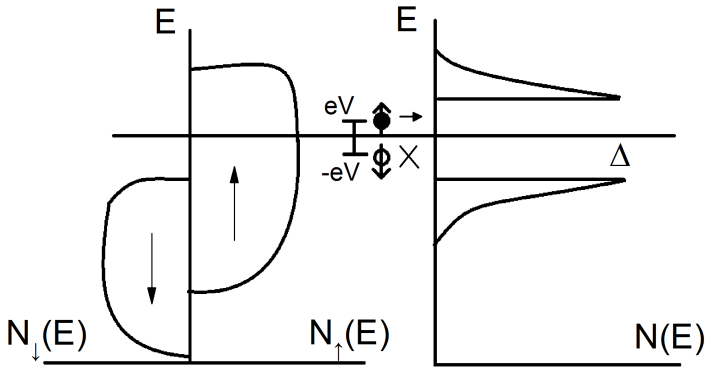

Figure 19: Andreev reflection process at half metal/S interface. Because there is no density of states for spin down holes, a Cooper pair cannot be formed; the Andreev reflection is prohibited.

the general case of partially spin polarized current, we need to decompose the current into two parts:

$$I = I_\uparrow + I_\downarrow = 2I_\downarrow + (I_\uparrow - I_\downarrow) = \frac{2I_\downarrow}{I_\uparrow + I_\downarrow} I + \frac{I_\uparrow - I_\downarrow}{I_\uparrow + I_\downarrow} I, \tag{33}$$

where $I_\uparrow$ is the electric current of spin-up electrons, and $I_\downarrow$ is the current of spin-down electrons. We define the spin polarization as

$$P = \frac{I_\uparrow - I_\downarrow}{I_\uparrow + I_\downarrow}. \tag{34}$$

This is a reasonable definition, since $P = 1$ for fully polarized system and $P = 0$ for unpolarized system. Using this definition, the total current can now be written as

$$I = (1 - P)I + PI, \tag{35}$$

where the first term is unpolarized current, and the second term is fully polarized current.

Taking the derivative of (35) with respect to bias voltage, we get a similar expression for the interfacial conductance:

$$\frac{dI}{dV} = (1 - P)(\frac{dI}{dV})_u + P(\frac{dI}{dV})_p. \tag{36}$$

Table 4: Summary of the Andreev and normal reflection probabilities obtained from the spin polarized BTK model. A_u and B_u are for unpolarized current; A_p and B_p are for fully polarized current.

	A_u	B_u	A_p	B_p
$E \leq \Delta_1$	$\frac{\Delta^2}{E^2+(\Delta^2-E^2)(1+2Z^2)^2}$	$1-A_u$	0	1
$\Delta_1 < E < \Delta_2$	$\frac{u_{01}^2 v_{01}^2}{\gamma_1^2}$	$1-A_u$	0	1
$E > \Delta_2$	$\frac{u_{01}^2 v_{01}^2}{\gamma_2^2}$	$\frac{(u_{02}^2-v_{02}^2)^2 Z^2(1+Z^2)}{\gamma_2^2}$	0	$\frac{(u_{02}^2-v_{02}^2)^2 Z^2(1+Z^2)}{\gamma_3^2}$

$u_{01}^2 = \frac{1}{2}(1+\sqrt{(E^2-\Delta_1^2)/E^2}) = 1-v_{01}^2$
$u_{02}^2 = \frac{1}{2}(1+\sqrt{(E^2-\Delta_2^2)/E^2}) = 1-v_{02}^2$
$\gamma_1^2 = (u_{01}^2 + Z^2(u_{01}^2 - v_{01}^2))^2$
$\gamma_2^2 = u_{01}^2 v_{02}^2 + (u_{01}^2 - v_{02}^2)(u_{02}^2 + Z^2 + (u_{02}^2 - v_{02}^2)Z^2(1+Z^2))$
$\gamma_3^2 = (u_{02}^2 - v_{02}^2)(u_{02}^2 + Z^2 + (u_{02}^2 - v_{02}^2)Z^2(1+Z^2))$

The two derivatives, $(dI/dV)_u$ and $(dI/dV)_p$ then need to be treated separately.

Here we employ the modified BTK model proposed by Strijkers and coworkers [101]. They argue that Eqn. 27 is still valid, so are the coefficients in Table 3 for the unpolarized part of the current. For the fully polarized current, as discussed above, the Andreev reflection is prohibited, so $A_p = 0$. Conservation of probability requires $A_p + B_p + C_p + D_p = 1$, so B, C and D needs to be renormalized.

Another complication considered in the Strijkers modification is the proximity effect. Proximity effect refers to the phenomenon that the Cooper pairs from the superconductor have a coherence length ξ, and thus can penetrate into the normal metal, making the top ξ depth of N superconducting too. Let's call the gap of this proximity induced layer Δ_1, and the gap of the original superconductor Δ_2. On one hand, the quasiparticle must have $eV > \Delta_2$ in order to enter the inducing superconductor; on the other hand the Andreev reflection will be limited to $eV < \Delta_1$, since the proximity induced superconducting layer is now in direct contact to the normal metal. We now need to match the boundary condition for the BdG equation at two interfaces. The calculation is rather tedious, and the result is summarized in Table 4.

We plot some representative conductance spectra from the spin polarized BTK model in Fig. 20. On the left panel we show the progression of the conductance curves with increasing P. We see the normalized zero bias conductance drops from 2 when $P = 0$ to 0 when $P = 1$. We assumed there is no proximity effect in this example. On the right panel we show how the proximity effect changes the conductance curves. We see the induced gap introduces distinct features at Δ_1. The inclusion of fitting parameters Γ, P and Δ_1 greatly increases the flexibility of the BTK model.

The standard BTK model assumes that the superconducting gap Δ is a constant, thus the angular momentum of the Cooper pair is zero (s-wave). This constraint can be loosened to calculate the point contact spectra for p-wave and d-wave superconductors [48]. For anisotropic gap functions, the Andreev reflection no longer happens, since there are density of states available inside the gap. Nevertheless, the BTK method to solve the BdG equation is still valid, and we will go into the details of the calculation in Chapter 6. Good agreement has been found between the d-wave BTK model and experiment [21].

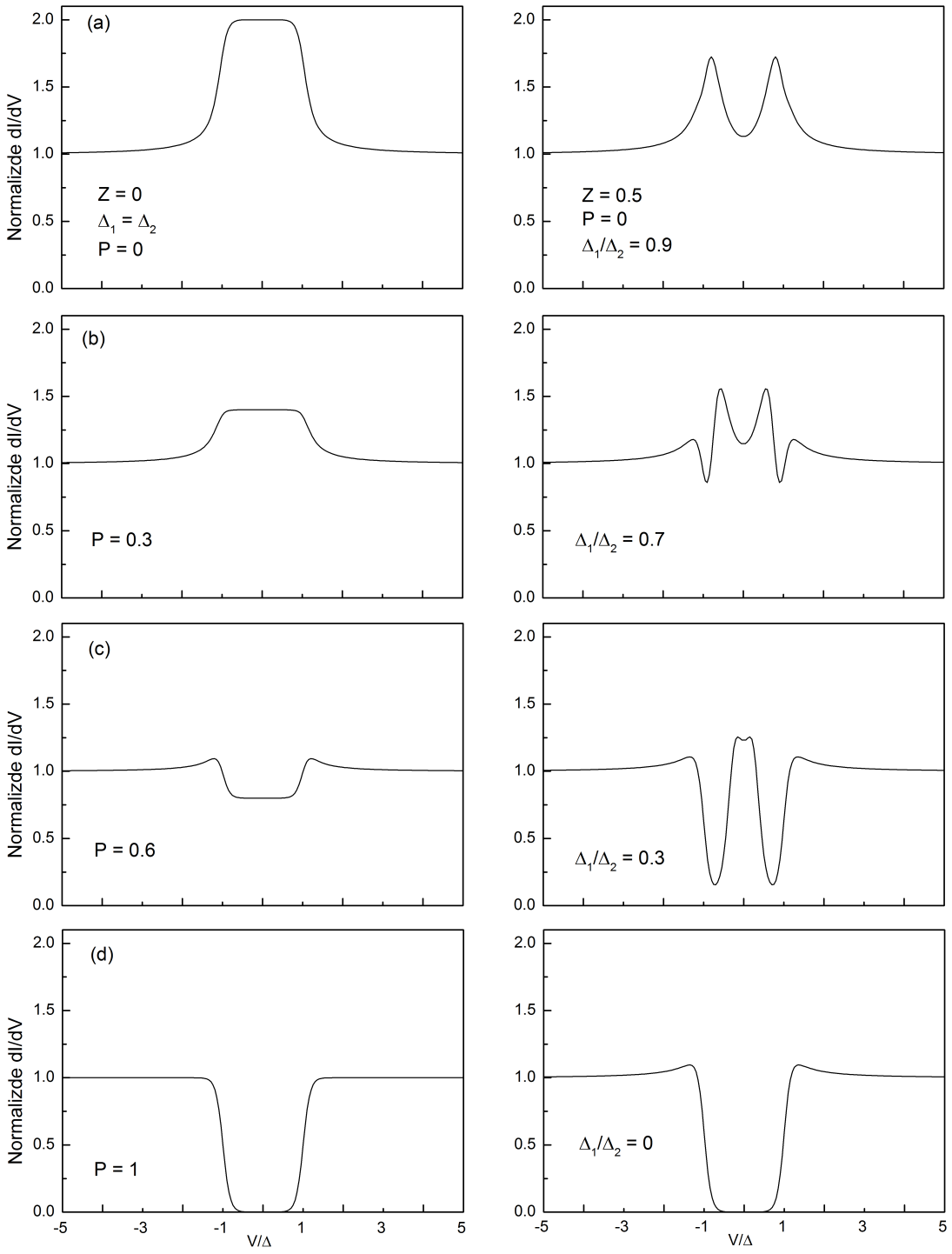

Figure 20: Conductance spectra calculated from the spin polarized BTK model. Left panel: the normalized zero bias conductance goes from 2 when $P = 0$ (a) to 0 when $P = 1$ (d). A transparent interface ($Z = 0$) and no proximity effect ($\Delta_1 = \Delta_2$) is assumed. Right panel: proximity induced gap Δ_1 limits the voltage range that Andreev reflection can happen. We pick $Z = 0.5$ and $P = 0$ in these plots. For all plots the temperature $T = T_c/10$.

CHAPTER IV

EXPERIMENT METHODS

4.1 Preparation of metal tip for point contact measurement

From the discussion in the previous chapter, we see that it is critical for the electron transport to enter the ballistic regime, so that both energy and momentum information is preserved. Experimentally, how small the tip diameter needs to be so that the transport will be ballistic? To answer this question, we need to take a closer look to the regimes of transport through a small metallic constriction (Fig. 15).

The Ohm's law rules in the thermal regime, and Maxwell gives the resistance of small metallic constriction as

$$R_{max} = \frac{\rho}{2r}, (l \ll r) \tag{37}$$

where ρ is the resistivity of the metal, l is the electron mean free path and r is the size of the contact. In the ballistic regime, the resistance is given by Sharvin [96] as

$$R_{shar} = \frac{4\rho l}{3\pi r^2}, (l \gg r) \tag{38}$$

while Wexler [112] gives a formula for the intermediate regime:

$$R_{wex} = \frac{4\rho l}{3\pi r^2} + \frac{\rho}{2r}(l \sim r). \tag{39}$$

Here we define the boundary of ballistic transport as the intersection of Maxell and Sharvin limits:

$$R_{max} = R_{shar}. \tag{40}$$

The mean free path l needed in the Sharvin formula can be estimated using the Drude model:

$$\rho l = \frac{\hbar}{e^2}(\frac{3\pi^2}{n^2})^{1/3} \tag{41}$$

For a typical metal, $n \sim 10^{29}/m^3$ and $\rho \sim 1\mu\Omega$cm, we plot the relation between contact size and contact resistance in this case in Fig. 21. We see the criterion $R_{max} = R_{shar}$ is met when $r \sim 100$nm. So the maximum tip diameter we can accept is ~ 100 nm.

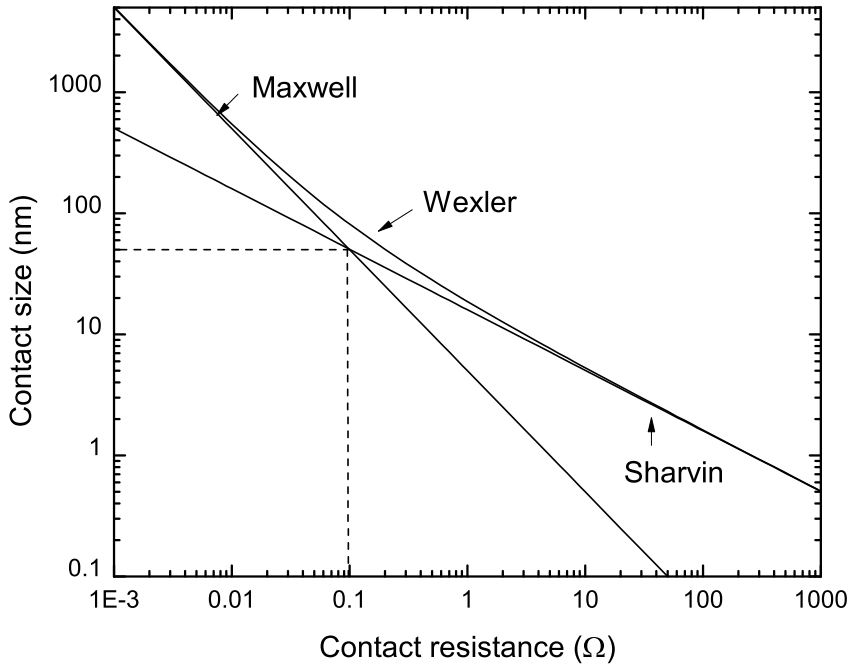

Figure 21: Contact resistance of small metallic restriction from thermal regime to ballistic regime. The boundary of ballistic regime is defined as the intersection of Maxwell and Sharvin limits.

Three methods are frequently used to prepare metal tips of this quality: Mechanical cutting is the easiest, but usually produces multiple tips and has poor reproducibility. Thermal field treatment in ultrahigh vacuum (UHV) environment can produce single atom sharp tip, but is both complicated and time-consuming [75]. The third method is electrochemical etching, which is practical, reliable and produces tips of sufficient quality. In this work, we use electrochemical etching to make niobium and gold tips. The following two paragraphs give detailed discussions of the experiment setup for each material.

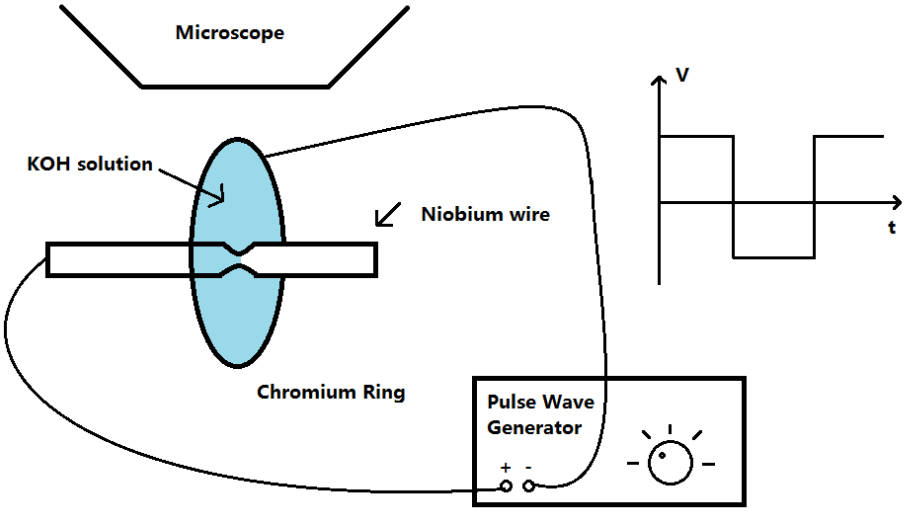

Figure 22: Preparation system for niobium tip. A square wave is generated from a homemade wave generator (using an Arduino circuit board) and applied between the niobium wire and the chromium ring. A thin layer of KOH solution is applied on the ring. The electrochemical etching process etches away the niobium. Details of the process is described in the text.

We choose niobium as a tip material because niobium is an $s-$wave superconductor with a relatively high T_c of 9.3 K. This makes niobium an ideal probe for normal metallic materials as well as other (possibly unconventional) superconductors. The niobium tip is prepared using a scanning tunneling microscopy (STM) tip preparation system. A schematic of the system is shown in Fig. 22. A droplet of 6 mol/L potassium hydroxide (KOH) solution is carefully put on a chromium ring of a few millimeters diameter and is suspended on the ring due to surface tension. 0.005" diameter niobium wire (99.8% purity, California Fine Wire Company) is then sent to penetrate through the droplet, and a 5 V square wave is applied between the wire and the ring. The electrochemical reaction etches away the niobium that is in the KOH droplet, and forms a neck region on the wire. The reaction continues until the wire breaks off. Afterward, a lower voltage of 1 V is applied to fine etch the tip. The process is monitored under optical microscope (maximum resolution $\sim$ 1

μm, until the best possible sharpness is achieved. The tip is then examined under scanning electron microscope (SEM) (maximum resolution $\sim$ 20 nm), to determine if the sharpness met the ballistic transport criterion discussed above.

We also prepare non-superconducting gold tip for the point contact measurement, which is used as a probe for the topological superconductor samples. Unfortunately even with the aide of external voltage, gold does not react with KOH. We use a different setup here following that described in Ref. [85] (Fig. 23). Specifically, we mix 37% HCl and ethanol at 1 to 1 volume ratio in a beaker. A stainless steel ring is placed at the surface of the solution and used as cathode. 0.01" gold wire (99.999% purity, ESPI metals) is dipped into the center of the ring, and serves as the anode. A dc voltage of about 2 V (from Agilent E3610A dc power supply) is applied to keep the reaction going at a slow rate, until the gold wire immersed in the solution drops off. The tip is then observed under optical microscope and SEM, if the diameter of the tip is below 100 nm, it can be used for the measurement. Otherwise the process is repeated.

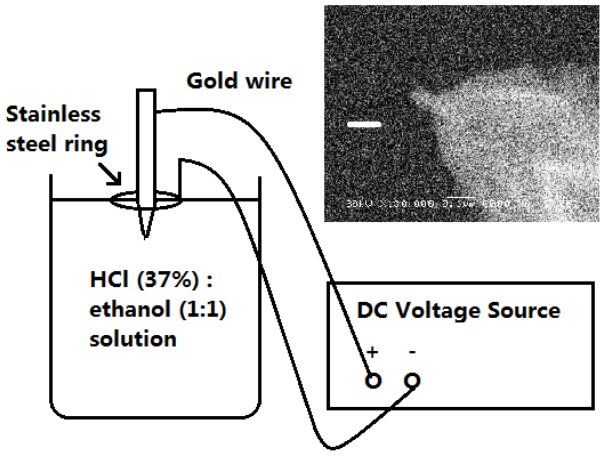

Figure 23: Preparation system for gold tip. A ring made of stainless steel is placed at the surface of 1:1 37% HCl to ethanol solution. A gold wire is immersed in the solution through the center of the ring. A dc voltage of $\sim$ 2 V is applied between the gold wire and the ring. By fine tuning the dc voltage, very sharp tip can be made. The inset on the right is an SEM image of a gold tip made using this method. The white scale bar is 100 nm.

4.2 Piezo controlled nanopositioning system

In point contact measurement, it is critical to have a reliable way to engage the tip to the sample, and to have precise control of the contact resistance. From Fig. 21 we see that we must have contact resistance $> 0.1\ \Omega$ to enter the ballistic transport regime. In addition to precise movement control in the z direction, it would also be useful to have the ability to move in the $x - y$ direction, so that multiple points on the sample can be measured in one cool down procedure.

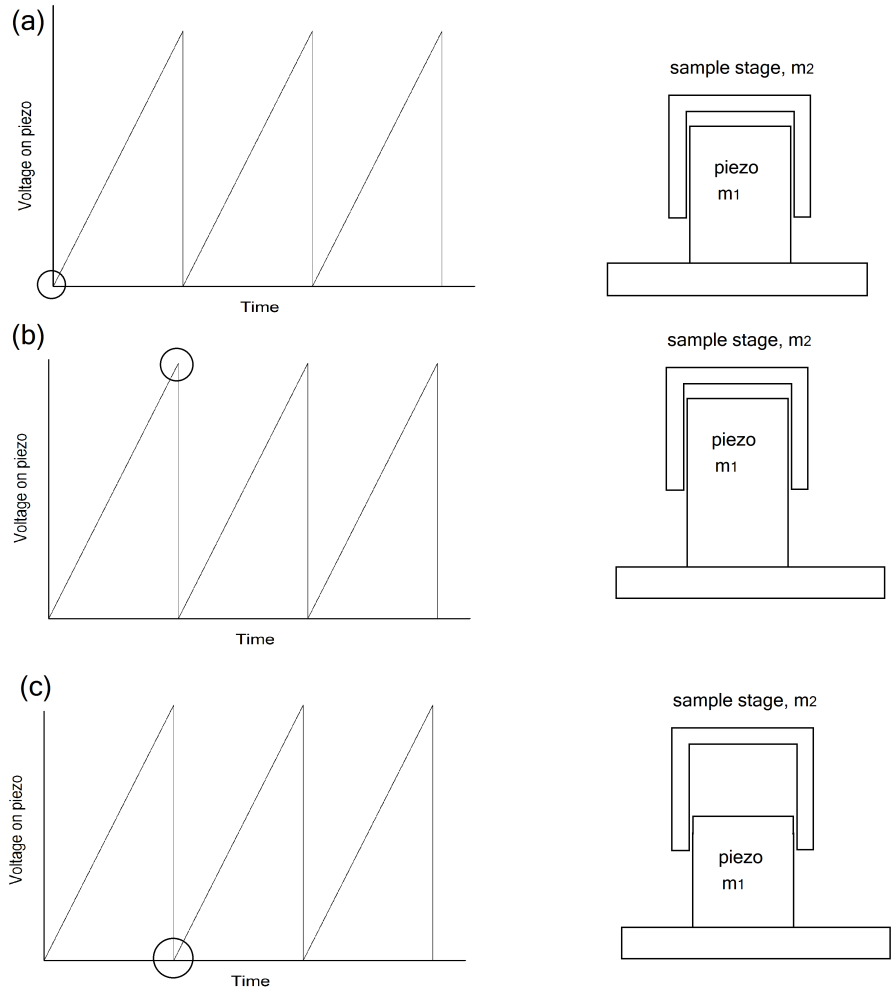

Figure 24: Operating principle of piezo controlled nanopositioner. (a) to (b): the piezo material slowly extends as the applied voltage increases, pushing the sample stage upwards. (c): the applied voltage on the piezo abruptly drops to 0, the piezo retracts, but the sample stage stays still due to inertia.

To achieve these purposes, we built a nanopositioning system using piezo controlled linear nanopositioners (attoCube Systems, ANPz30 for z direction movement and ANPx50 for x direction movement). The operating mechanism of piezo controlled nanopositioner is shown in Fig. 24. The piezoelectric material m_1 has the property that its length changes with applied voltage. The sample stage m_2 is sleeved onto the piezo and is held in place due to friction. A sawtooth wave voltage is applied to the piezo. During the slow extension of the piezo, m_1 and m_2 has no relative movement due to friction. But when the piezo is rapidly retracted, static friction is not enough to provide for the inertial force, so m_2 stays in place. This is much like the tablecloth trick we all have seen. By repeating this process, the sample stage m_2 is pushed up in a step-wise fashion, and by fine tuning the voltage, step size of as small as 10 nm can be achieved.

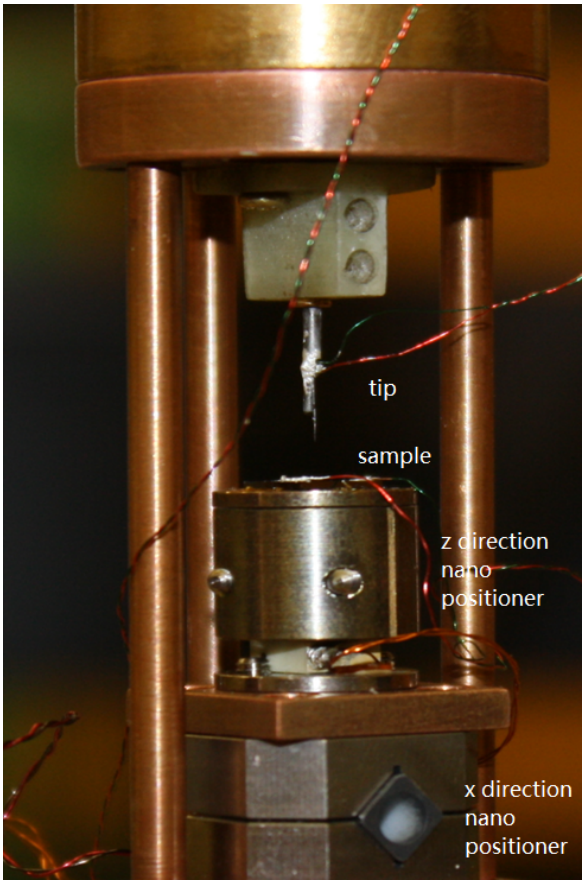

Figure 25: Picture of the nanopositioning system for point contact experiment.

We stack together two nanopositioners, one can move in the z direction, and the other can move in the x direction. A picture of the system is shown in Fig. 25. The sample is mounted on top of the z nanopositioner, and the tip is fixed a small distance above the sample. Once loaded in place, the z nanopositioner is used to engage and disengage the sample to and from the tip, and the x nanopositioner is used to move the sample horizontally. The system is thermal anchored to a cryogenic fridge which has a large mass. This helps to eliminate any mechanical vibration noise from the environment. The system is then loaded into in a vacuum chamber, to ensure there is no condensation of ice or any other gases, which is essential for creating low temperature environment and for having a stable point contact. When approaching the sample to the tip, the z nanopositioner first works in continuous mode, and the tip/sample contact resistance (which is infinity initially) is monitored by a feedback control loop. The approach process stops immediately when the contact resistance is smaller than a pre-determined value, say 100 kΩ. Although large contact resistance means smaller contact footprint, the contact is usually unstable at resistance larger than a few hundred ohms. To reach a stable contact, the z nanopositioner is then operated in step mode manually, until a reasonable contact resistance that is both stable and in the ballistic transport regime is reached.

4.3 Helium-3 cryogenic fridge and superconducting magnet system

The typical transition temperature of topological superconductor is about 1 K, and lower temperature is always favored, since it helps to reduce thermal smearing of the measured spectra. Thus all measurements in this dissertation are performed in a helium-3 fridge (Janis Research Company, model HE-3-SSV-14T) which can maintain a 300 mK cryogenic environment. A highly simplified schematic of the helium-3 fridge is shown in Fig. 26.

The boiling point of liquid is a decreasing function of the vapor pressure above

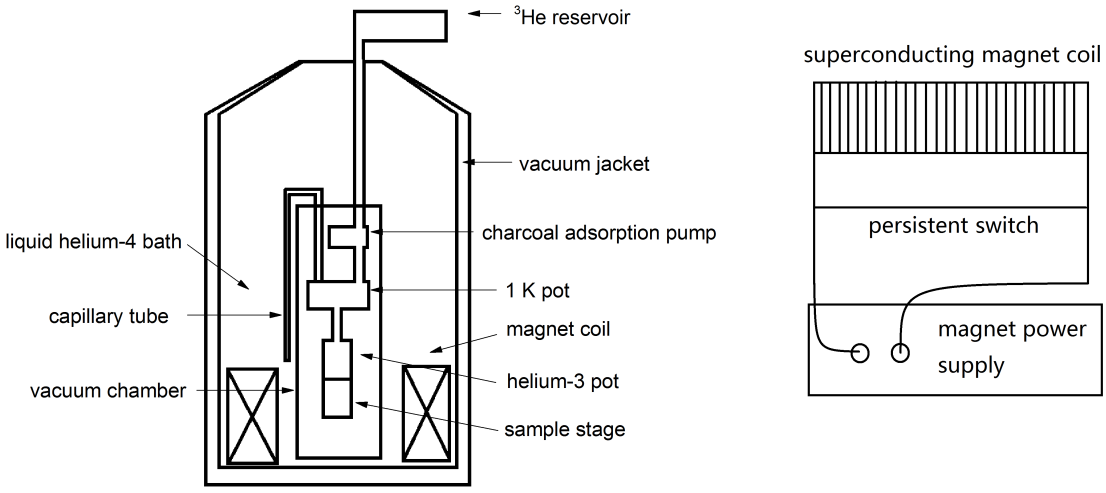

Figure 26: Schematics of the helium-3 fridge (left) and the magnet system (right).

the liquid surface. Helium-3 fridge operates by taking advantage of this physical principle. Helium-3 is a rare isotope of helium and is produced through tritium decay. The production of tritium requires high flux of neutron and its half decay life is only 12 years. This makes helium-3 an extremely precious resource. Thus the helium-3 is sealed in a closed system in the fridge. During the cool down, liquid regular helium-4 is sucked from the bath into the so called 1 K pot through a capillary tube. A mechanical pump is used to pump the liquid helium-4 surface in the 1 K pot. This cools down the 1 K pot to a temperature of about 1.1 K, which is lower than the boiling point of helium-3 (3.2 K). Liquid helium-3 is then condensed and collected in the helium-3 pot. Finally, by pumping on the liquid helium-3 surface in the helium-3 pot using the charcoal adsorption pump, a temperature of 300 mK can be reached. The sample stage and the wiring are both thermally anchored to the helium-3 pot, and reach the same temperature when in equilibrium. The fridge can hold at the base temperature for about 48 hours without mechanical pumping before all liquid evaporates from the helium-3 pot.

To study the magnetic field dependence of point contact spectra, a magnet is required. The cryogenic system we use is equipped with a 14 Tesla superconducting

magnet. A schematic of the magnet is shown in the right panel of Fig. 26. The magnet coil is made of superconducting wires, and is connected to the power supply (American Magnetics Inc., model 4Q05100PS). The magnet is immersed in liquid helium bath and is thus in superconducting state. The magnet coil is short-circuited by a persistent switch, which is made of superconductor. A small heater is used to control whether the persistent switch is superconducting or not. When the heater is on, the persistent switch is resistive, and the current from the power supply flows into the zero resistance magnet coil. By slowly ramping up the current, a magnetic field is created inside the coil. When desired magnetic field is reached, the heater is turned off, and the persistent switch becomes superconducting. Because the magnet coil has an inductance L, the current from the power supply now goes through the persistent switch. The power supply current can then be ramped down to zero, without changing the current in the superconducting coil. This way the magnetic field is persisting in the superconducting magnet coil, which requires no power consumption and has minimum electrical noise.

4.4 Electronic setup

We use 4-terminal configuration to measure the conductance of the tip/sample interface. A simplified version of the electronic setup for the measurement is shown in Fig. 27. As one can see in the left panel, two leads are attached to the tip, and two leads are attached to the sample. A current is sent from the tip to the ground on the sample, while the voltage difference between the tip and the sample is measured. This 4-terminal measurement setup eliminates the contact resistance of the wire to the sample and gives an accurate measurement of the tip/sample contact resistance.

A simplified measurement circuit is shown in the right panel of Fig. 27. A dc current I_{dc} is generated from an HP 3325A function generator and sent through the point contact to the ground. The dc bias V_{dc} across the point contact produced by this

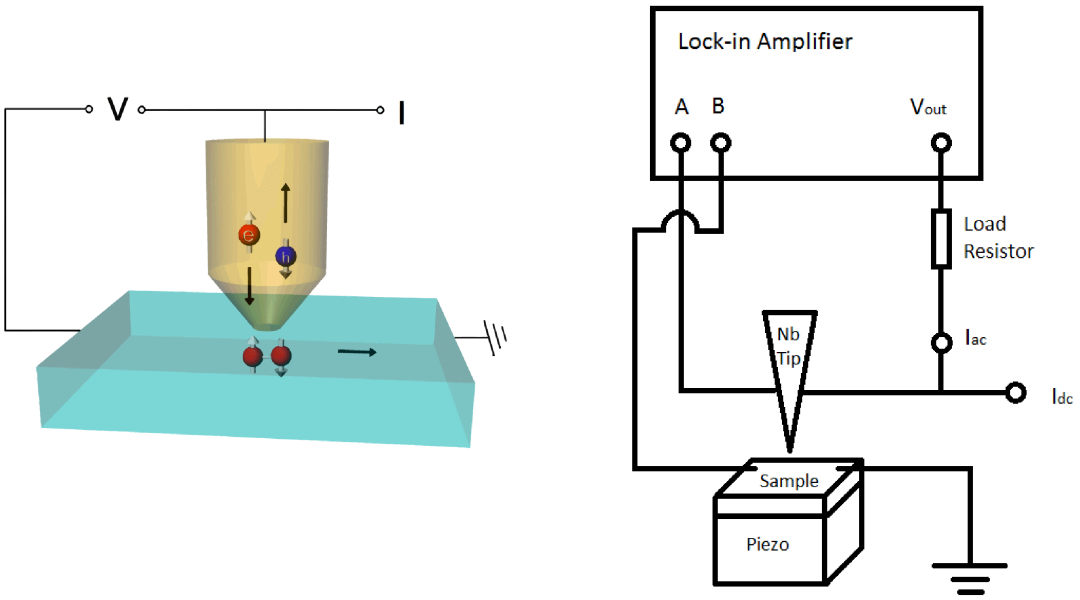

Figure 27: The electronic setup for point contact measurement. Standard 4-terminal measurement and ac+dc lock-in technique is used to obtain the differential conductance spectra (dI/dV vs. bias voltage) of the tip/sample contact.

current is measured by a multimeter (Keithley, model 2000). In principle one could plot I_{dc} vs. V_{dc} and then carry out the derivative dI_{dc}/dV_{dc} to get the point contact spectra, but this method is often noisy because the Fourier transform of a dc voltage contains signals from *all* frequencies. A better method is to measure dI/dV directly. In order to do this, an ac voltage of 0.1 V, 1 kHz from the "sine out" output of the lock-in amplifier (Stanford Research Systems, model SR830) is sent through a 1 MΩ load resistor. This load resistor is much larger than any other resistor in the circuit, so it effectively converts the voltage output of the lock-in amplifier into a current output. This ac current component is superimposed to the dc current, so the total current sent through the tip to the sample ground is $I = I_{dc} + I_{ac}(f)$, where f is the frequency of the ac current. The corresponding response voltage $V_{ac}(f)$ can be picked up by the lock-in amplifier, even in a very noisy background. Since $dI/dV \approx \Delta I/\Delta V = I_{ac}/V_{dc}$, when I_{ac} is small enough, I_{ac}/V_{ac} is an excellent estimation of dI/dV. By plotting I_{ac}/V_{ac} as a function of V_{dc}, the point contact conductance spectrum is obtained.

CHAPTER V

PROXIMITY INDUCED SUPERCONDUCTIVITY IN TOPOLOGICAL INSULATOR BI_2SE_3

5.1 Summary of previous work

Recently several experimental groups [119, 111, 115, 61] have demonstrated the possibility to induce superconductivity in 3D topological insulators via the proximity of s-wave superconductor. Yang and coworkers [119] investigated the conductance spectra of superconducting Sn/Bi_2Se_3 junctions down to 250 mK. They used photolithography to fabricate Sn contacts on exfoliated Bi_2Se_3 flakes, and the contact size is a few microns. They observed a number of conductance anomalies below the T_c of Sn, including a gap smaller than that of the Sn, and a zero bias conductance peak (ZBCP) that increases at lower temperatures. They argued that the smaller gap comes from a proximity induced superconducting phase of Bi_2Se_3, and the ZBCP is a manifestation of the resonant bound states between incoming and reflecting wave functions at the interface, which is characteristic of a superconductor with $p_x + ip_y$ symmetry. Since the contact size is much larger than the mean free path, quantitative comparison between their conductance spectra and the BTK theory is difficult.

Wang and coworkers [111] fabricated $NbSe_2/Bi_2Se_3$ heterostructure using molecular beam epitaxy (MBE). Superconductor $NbSe_2$ is used as the substrate for MBE growth of high quality Bi_2Se_3 thin film. The local density of states (LDOS) of the Bi_2Se_3 thin film is studied using *in situ* scanning tunneling spectroscopy (STS) and a gap like feature is found in the dI/dV spectra, with the gap size is smaller than that of $NbSe_2$. The spectra can be fit well by a proximity effect model, and suggest that the Bi_2Se_3 films become superconducting due to the proximity effect of $NbSe_2$ substrate.

Since STS is a pure tunneling measurement, they did not observe the ZBCP (see Chapter 6 for extended discussions), and the nature of the induced superconductivity remains unexplored. Xu and coworkers [115] performed similar STS measurement on Bi_2Te_3 thin films grown on $NbSe_2$, and also observed a smaller gap, presumably resulting from proximity effect. They also profiled the zero bias conductance through a magnetic vortex core, to search for the Majorana bound state. Although a ZBCP was indeed observed in this case, they cannot rule out the possibility that the ZBCP is coming from states other than the MFs.

Finally, multiple-point-contact spectroscopy study of 3D topological insulator Bi_2Se_3 has also been reported in the literature [61], where an array of 40 gold coated spring loaded spherical tips of 0.5 mm diameter was pressed onto either Bi_2Se_3 or Bi_2Te_2Se films. The segregated Bi islands on the sample surface are expected to be superconducting and thus may induce superconductivity in the sample. Robust ZBCP was observed in the dI/dV spectra and could be assigned to the Majorana bound state. However, the results are also inconclusive due to the limitation of the measurement apparatus (averaging over 40 large-diameter point contacts) and the poor quality of the samples (Bi inclusions or segregation to the surface).

As a remark, a reduced superconducting gap (in addition to the parent superconducting gap) is clearly evident from the above mentioned pioneering works. However, the exact nature (p-wave vs. s-wave; surface vs. bulk) of the induced superconductivity remains elusive. Therefore, a true point contact measurement on high quality TI single crystal is needed, to further understand the proximity effect on TI. In this Chapter, we present such a point contact spectroscopy study of Bi_2Se_3 single crystals, using a superconducting niobium (Nb) tip. We also present an extension to the BTK model based on the Fu-Kane Hamiltonian [31].

5.2 Results and discussion

We perform the point contact Andreev reflection spectroscopy study of Bi_2Se_3 single crystals using a superconducting Nb tip. The Bi_2Se_3 crystal surface is exfoliated by scotch tape before mounting to the sample stage, to minimize the effect of air doping [82]. Two copper leads are silver pasted onto the sides of the sample, and the remaining two copper leads are silver pasted onto the tip, to perform a 4-terminal measurement of the interface resistance. The systems is then loaded into the helium-3 fridge and cooled down. Figure 28(a) shows the normalized point contact resistance (with respect to the normal-state resistance R_N of the Nb/Bi_2Se_3 junction) as a function of temperature for different interfacial barrier strengths. Here, the interfacial barrier strength is controlled by carefully engaging the z direction nanopositioner in single step mode. As one can see in Fig. 28(a), for all barrier strengths there is a drop in resistance at ~ 9 K, which corresponds to the superconducting transition of Nb. Interestingly, we also find that when the interface is sufficiently transparent, a significant drop in resistance occurs between 1-4 K, well below the T_c of Nb. This is suggestive of formation of proximity induced superconducting states at the interface. Figure 28(b) shows the temperature dependence of the contact resistance at different magnetic field, for a 15.9 Ω contact. We see the second resistance drop persists in a moderate magnetic field up to 1 T. This could be related to the critical field of the proximity induced superconductivity. When the interface is relatively resistive (≥ 40 Ω), no abrupt resistance drop is observed with decreasing temperature, suggesting the barrier is too strong for proximity effect to manifest.

The point contact spectra (dI/dV vs. bias voltage) of Nb/Bi_2Se_3 junction are measured at different temperatures and shown in Fig. 29. We find that when the interface resistance is high [Fig. 29(a)], the measured point contact spectra is characterized by a conductance dip at zero bias voltage and two broad coherent peaks at

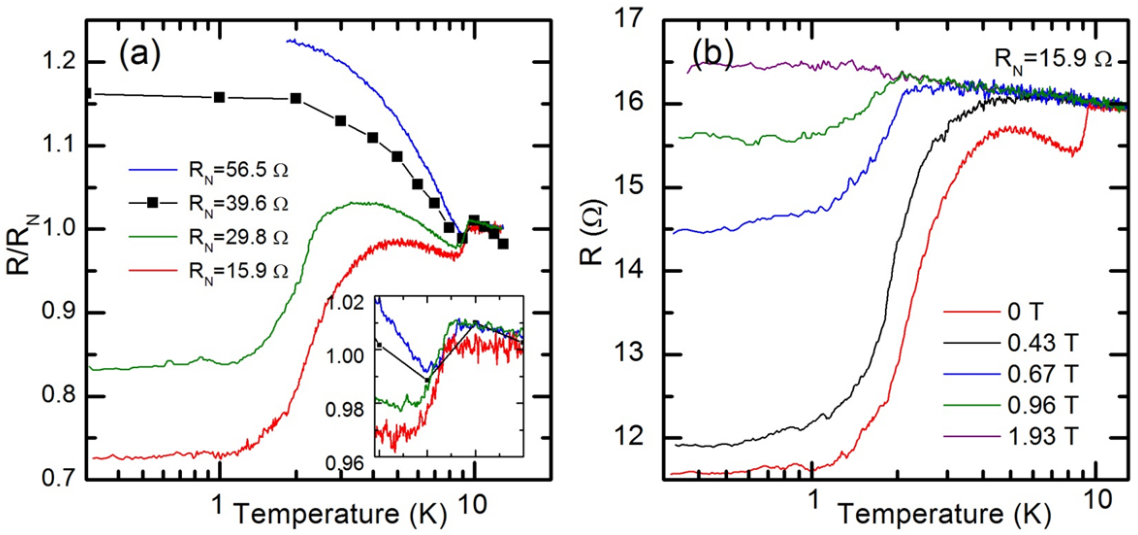

Figure 28: (a) Normalized point contact resistance (at zero external voltage bias) of Nb/Bi_2Se_3 junction as a function of temperature for different interfacial barrier strengths. Inset: zoom-in view of the data around the T_c of Nb. (b) Normalized point contact resistance as a function of temperature at selected magnetic fields for the lowest interface resistance in (a), $R_N = 15.9\ \Omega$. The magnetic field is applied perpendicular to the *ab* plane of Bi_2Se_3.

$\pm\Delta/e$, where Δ is the superconducting gap of Nb. This line shape can be quantitatively described by the spin polarized BTK model we presented in Chapter 3. The best fits to data using the spin polarized BTK model are shown as the red dashed lines in Fig. 29(a). The fitting parameters are as the following: For $T = 2$ K, $\Delta_1 = 1.35$ mV, $\Delta_2 = 1.45$ mV, $Z = 0.29$ and $P = 0.52$; for $T = 5$ K, $\Delta_1 = 1.32$ mV, $\Delta_2 = 1.45$ mV, $Z = 0.3$ and $P = 0.5$; for $T = 8$ K, $\Delta_1 = 0.53$ mV, $\Delta_2 = 0.6$ mV, $Z = 0.3$ and $P = 0.5$. The proximity induced gap (Δ_1) we obtained from the model is always slightly smaller than the gap of Nb (Δ_2), which is expected and consistent with the observation by other groups mentioned in the previous section. The interface barrier strength Z is consistently around 0.3, and the spin-polarization P is around 0.5. Although one would expect the electric current to be fully polarized ($P = 1$) on the surface of Bi_2Se_3 due to the spin-momentum locking, recent spin-resolved ARPES measurements find that the value of P is actually widespread [46], while recent first-principles calculation suggests P ~ 0.5 owing to strong spin-orbit entanglement [120].

Moreover, since the Fermi level of our Bi_2Se_3 crystal is in the conduction band, the bulk of the material is conducting too. Thus it shall not be surprising that part of the current is bulk current and not spin-polarized.

When the Nb tip is further pressed onto the Bi_2Se_3 surface, that is, when the effective tip diameter gets comparable to the expected mean free path of Bi_2Se_3 surface states, an anomalous conductance peak appears at zero bias and becomes stronger at lower temperatures. Such a zero-bias conductance peak was not seen in control experiments performed on normal-metal thin films (Au or Cu). It also cannot be attributed to the magnetic and Kondo scattering effects [4, 98], since no splitting of the density of states is observed when a magnetic field is applied (owing to the large g-factor of Bi_2Se_3, $g = 32$ [59], Zeeman splitting is expected to be very large).

To further investigate whether the features we observed in the conductance spectra are indeed related to the peculiar surface states of TI, we performed the same measurement on a highly doped Bi_2Se_3 crystal. Copper is added in the growth process as the dopant, and in this case the Fermi level is expected to be high in the conduction band, where the surface state has already merged into the bulk band [see Fig. 6(c)]. The results are presented in Fig. 30. For this sample, there is no qualitative difference between the spectra taken on the higher barrier interface and low barrier interface. There is no sign of the ZBCP even for most transparent junction achievable. Moreover, the line shape cannot be fitted well by the spin polarized BTK model. In fact, we find that the standard BTK model with quasiparticle lifetime correction is sufficient to describe the data. The best fits at selected temperatures are shown as the red dashed lines in Fig. 30. The fitting parameters are as the following: For $T = 2$ K, $\Delta = 1.5$ mV, $Z = 1.3$ and $\Gamma = 0.6$ mV; for $T = 5$ K, $\Delta = 1.4$ mV, $Z = 1$ and $\Gamma = 0.8$ mV; for $T = 7$ K, $\Delta = 1.3$ mV, $Z = 1$ and $\Gamma = 1$ mV. Note that due to copper segregation, the quality of the doped sample is not as good, and the oxidized copper may form an oxidation layer at the surface of the sample. So it

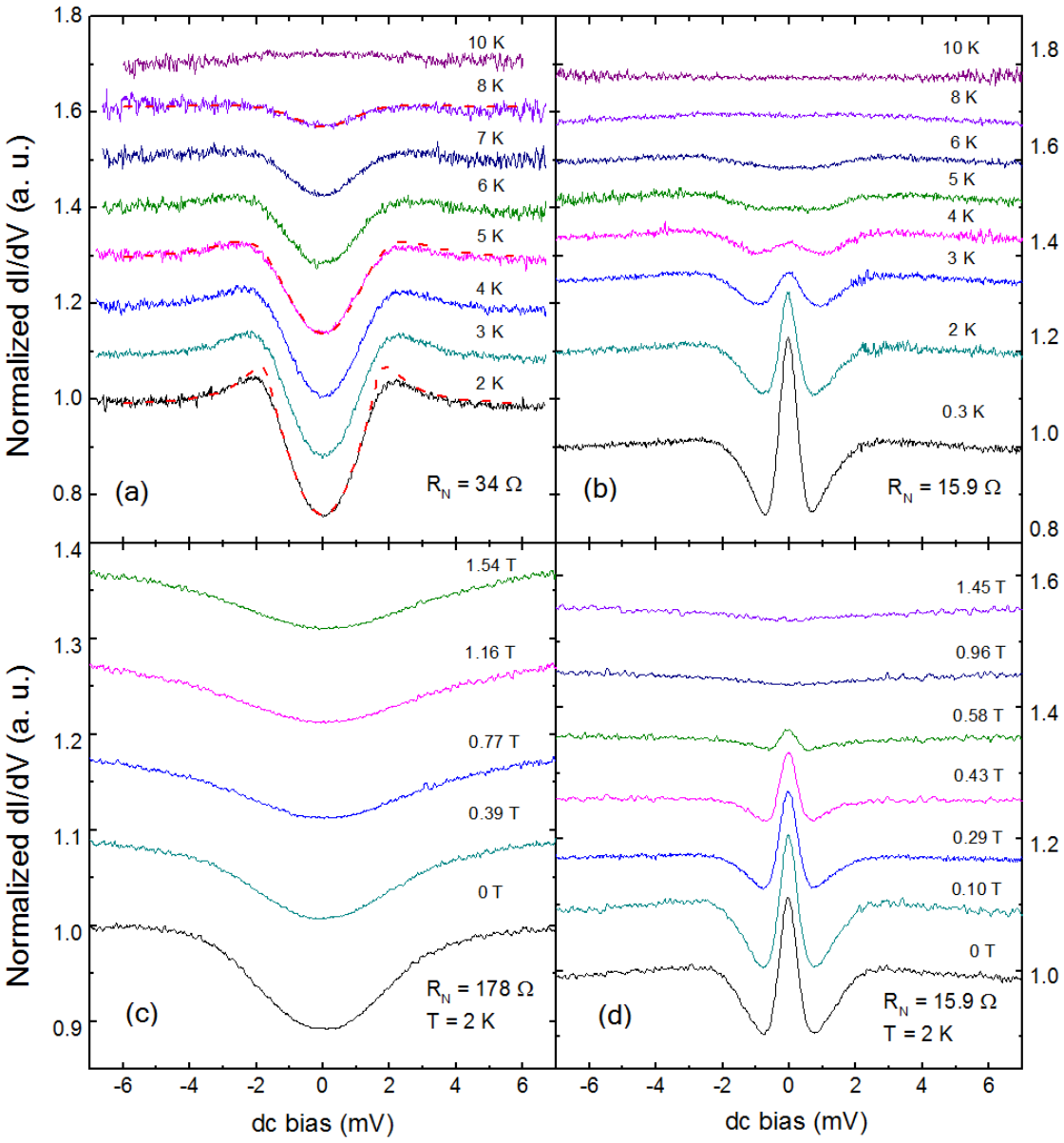

Figure 29: Point contact spectra of Nb/Bi_2Se_3 junction for (a) high barrier strength ($R_N = 34\ \Omega$) and (b) low barrier strength ($R_N = 15.9\ \Omega$) at different temperatures. The red dashed lines in panel (a) at 2 K, 5 K and 8 K are best fits to the spin polarized BTK model. Fitting parameters are described in the main text. The magnetic field dependence of the conductance spectra are shown in panel (c) for high barrier strength ($R_N = 178\ \Omega$) case and (d) for low barrier strength ($R_N = 15.9\ \Omega$) case. Spectra are shifted vertically for clarity.

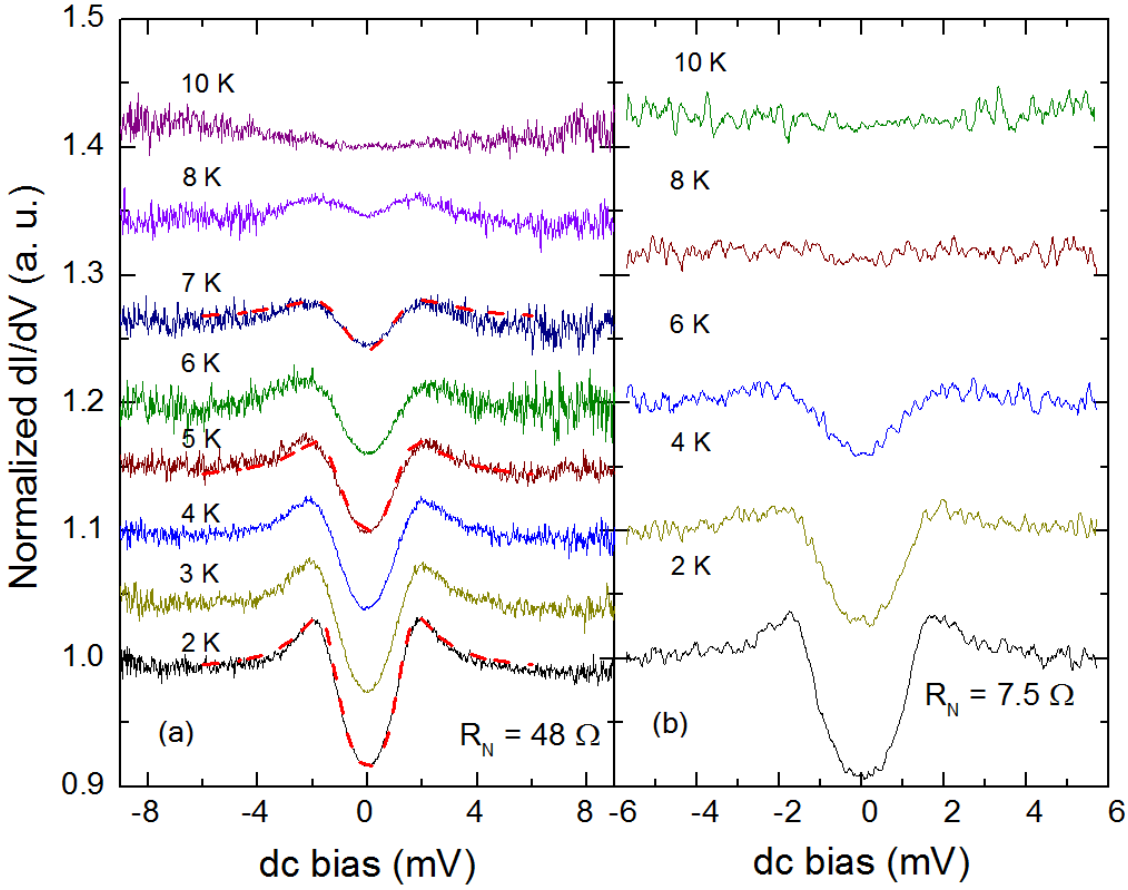

Figure 30: Point contact spectra of Nb/doped Bi_2Se_3 junction for (a) high barrier strength ($R_N = 48\ \Omega$) and (b) low barrier strength ($R_N = 7.5\ \Omega$) at different temperatures. The red dashed lines in panel (a) are best fits to the data using the BTK model with quasiparticle lifetime correction. Fitting parameters are given in the main text. Spectra are shifted vertically for clarity.

is not surprising that we have a relatively large Z (tunneling limit) and Γ (inelastic scattering dominates) in the model. Based on the lack of ZBCP and good agreement to the standard BTK model, we conclude that for the highly doped Bi_2Se_3 sample the transport is dominated by bulk electrons, and the conductance spectra we measured for the "undoped" Bi_2Se_3 with a pronounced ZBCP may indeed carry information about the surface band.

5.3 Extended BTK model for TI/S interface

To give a more quantitative description of the ZBCP originated from the surface state, we extend the BTK model to specifically consider the Hamiltonian of the TI with proximity induced superconductivity. When an s-wave superconductor is deposited on the surface of TI, the Cooper pairs can tunnel into the surface state. Following the groundbreaking work by Fu and Kane [31], the Hamiltonian of the TI can be written as

$$H_0 = \psi^\dagger(-iv\vec{\sigma}\cdot\nabla - E_F)\psi, \tag{42}$$

where $\psi = (\psi_\uparrow, \psi_\downarrow)^T$ are electron field operators, $\vec{\sigma} = (\sigma^x, \sigma^y)$ are Pauli spin matrices, v is the Fermi velocity, and E_F is the Fermi energy. When an s-wave superconductor is in the proximity, the Hamiltonian becomes

$$H = -iv\tau^z\sigma\cdot\nabla - E_F\tau^z + \Delta_0(\tau^2\cos\phi + \tau^y\sin\phi), \tag{43}$$

where Δ_0 is the size of the induced gap, which is somewhat smaller than the parent superconducting gap, $\vec{\tau}$ are Pauli matrices that mix the ψ and $\psi^\dagger$ blocks of Ψ. The excitation spectrum of this Hamiltonian is

$$E_{\mathbf{k}} = \pm\sqrt{(\pm v|\mathbf{k}| - E_F)^2 + \Delta_0^2}. \tag{44}$$

For $E_F \gg \Delta_0$ the low energy spectrum resembles that of a spinless $p_x + ip_y$ superconductor, as shown in Fig. 31(a).

To solve the BdG equation and calculate the point contact spectra, we follow the procedure proposed by Beenakker [9]. The original calculation was done for graphene, but the low energy dispersions are identical for the Dirac fermions in both systems, except for that the TI does not have the valley degeneracy. An intriguing implication of the low energy spectrum in Eqn. 44 is that when E_F is sufficiently small, *specular* Andreev reflection can happen, in which case an electron from the conduction band is converted to a hole in the valence band [Fig. 31(b)]. Specular Andreev reflection is clealy not possible for normal metals (see Fig. 14).

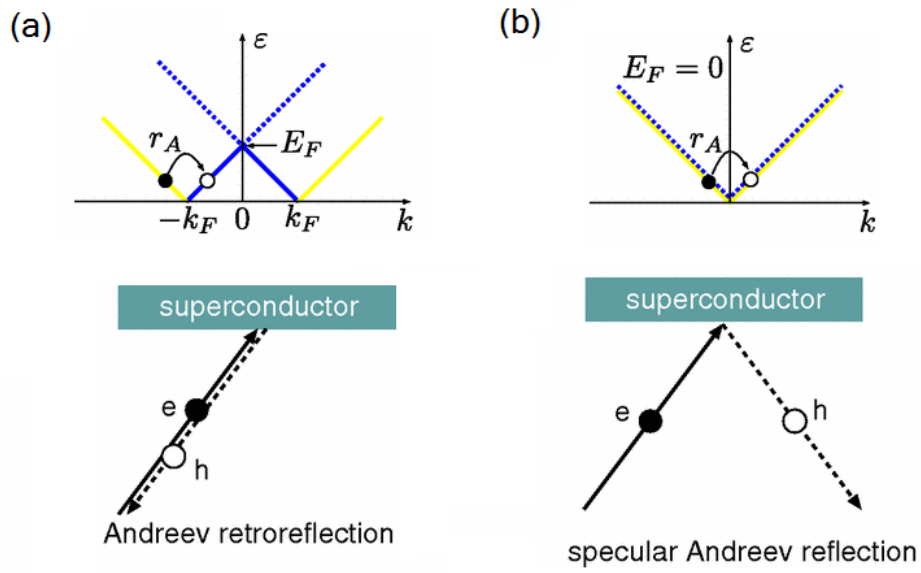

Figure 31: (adapted from Ref. [9]) The low energy dispersion of TI when $E_F \gg \Delta_0$. Yellow lines are for electron excitations and blue lines for hole excitations. The reflection process at the TI/S interface is represented by the arrow marked as r_A, and the real space picture is depicted in the bottom panel. When $E_F = 0$ [panel (b)], the electrons in the conduction band are converted to holes in the valence band, resulting in specular Andreev reflection.

The conductance spectra resulting from our calculations [125] are summarized in Fig. 32. Panel (a) shows the spectrum when the ratio of the Fermi energy to the proximity induced gap $E_F/\Delta_0 = 2$, and panel (b) is for $E_F/\Delta_0 = 100$. In either case, there is a ZBCP present in the conductance spectrum. For our experiment, the natural doping of Bi_2Se_3 typically sets the E_F near the bottom of the bulk conduction band. The band gap for Bi_2Se_3 is ~ 300 meV, and the superconducting gap for Nb is 1.5 meV, so we have $E_F/\Delta_0 \gtrsim 100$. While the observation of the ZBCP in our experiment data is consistent with the calculation, we do not observe the plateau-like shape below Δ_0/e in our data. This could be due to the thermal, or quasiparticle life time broadening. A more detailed model that considers these effects is needed to enable quantitative comparison to our data.

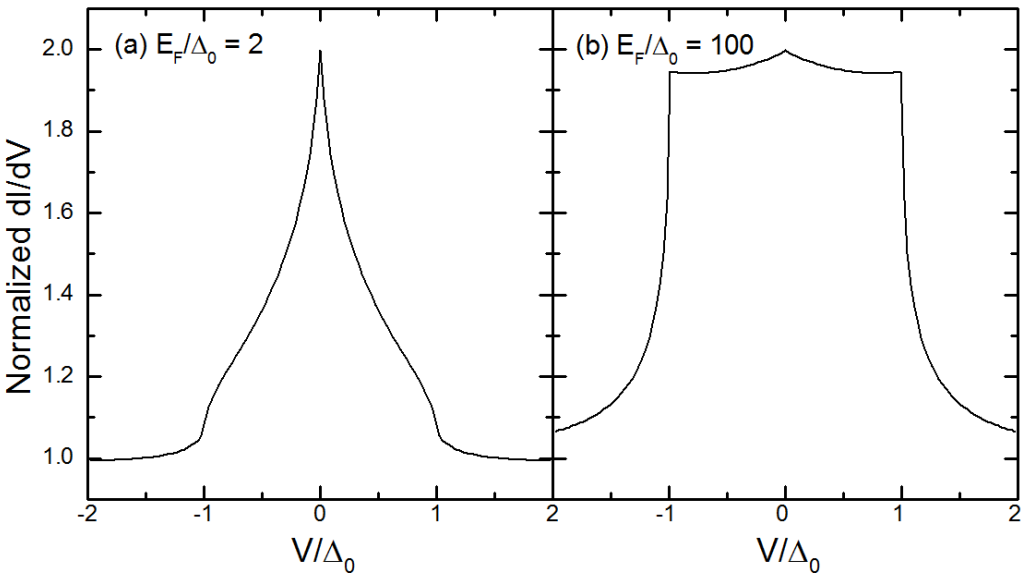

Figure 32: Calculated normalized conductance spectra for TI/S interface. (a) $E_F/\Delta_0 = 2$, (b) $E_F/\Delta_0 = 100$. In either case we observe nearly perfect Andreev reflection and thus a conductance peak at zero bias. The two spectra may look similar when temperature smearing and quasiparticle life time broadening are taken into consideration.

CHAPTER VI

PAIRING SYMMETRY OF CANDIDATE TOPOLOGICAL SUPERCONDUCTORS

6.1 Point contact spectroscopy of $Cu_{0.25}Bi_2Se_3$ using gold tip

Recall from the Chapter 2 that Bi_2Se_3 is made from double layers of $BiSe_6$ octahedra and has excellent layered structure. As a result, the doping of this material can be both substitutional and intercalative. Which kind of doping dominates is determined nominally by the elemental ratios. It is found [39] that single crystals of $Bi_{2-x}Cu_xSe_3$ prepared for $x = 0$ to 0.15 are never superconducting, while single crystals of $Cu_xBi_2Se_3$ are superconducting in a narrow window of $x = 0.1$ to 0.3. The carrier in $Cu_xBi_2Se_3$ is n type and the carrier concentration is found to be one order of magnitude higher than that of Bi_2Se_3.

The $Cu_{0.25}Bi_2Se_3$ single crystal studied in this work was prepared by Dr. Y. S. Hor at Missouri University of Science and Technology. Stoichiometric amounts of copper (99.99%), bismuth (99.999%) and selenium (99.999%) were melted in a sealed quartz tube, followed by slow cooling from 850 °C to 620 °C and finally quenching in cold water. Transport characterization [65] reveals that the superconducting transition starts from ∼3.3 K and the zero resistance state is reached at ∼1.2 K (See Fig. 33). The nominal superconducting fraction is found to be ∼35%, consistent with the phase diagram of $Cu_xBi_2Se_3$ reported by Kriener *et al.* [63]. The as-grown sample has a silver, shiny metallic surface, but turns into golden color after only one day, if exposed in air. This is likely due to copper segregation on the surface. To avoid the possible effect of copper segregation and surface oxidation, we used scotch tape to peel a fresh

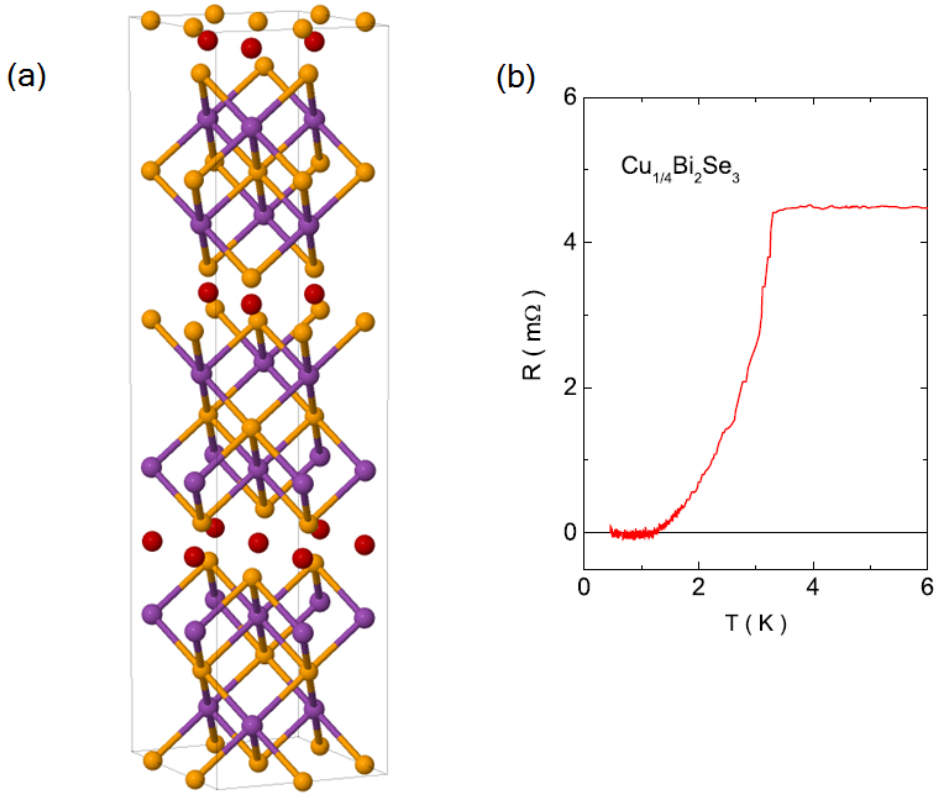

Figure 33: (a) Crystal structure of $Cu_xBi_2Se_3$. Purple balls represent bismuth atoms, orange balls represent selenium, and red balls represent copper. The copper is intercalated between the Bi_2Se_3 quintuple layers. (b) (adapted from Ref. [65]) The temperature T dependence of the sample resistance R. Zero resistance is observed below 1.2 K.

surface of the $Cu_{0.25}Bi_2Se_3$ right before the experiment. The freshly peeled sample was sealed into the sample chamber and pumped to high vacuum within 20 minutes.

Figures 34(a) and 34(b) present the typical point contact spectra measured at 0.27 K. For certain surface locations, we observed a pronounced ZBCP. The ZBCP is a sign of Andreev bound state (ABS) and indicative of unconventional superconductivity, which we shall discuss in detail later. For the other locations, however, only a broad dip is seen at low bias voltages. The dashed line in Fig. 34(c) is an attempt to fit the data to the standard BTK model described in Chapter 3. Clearly the s-wave model

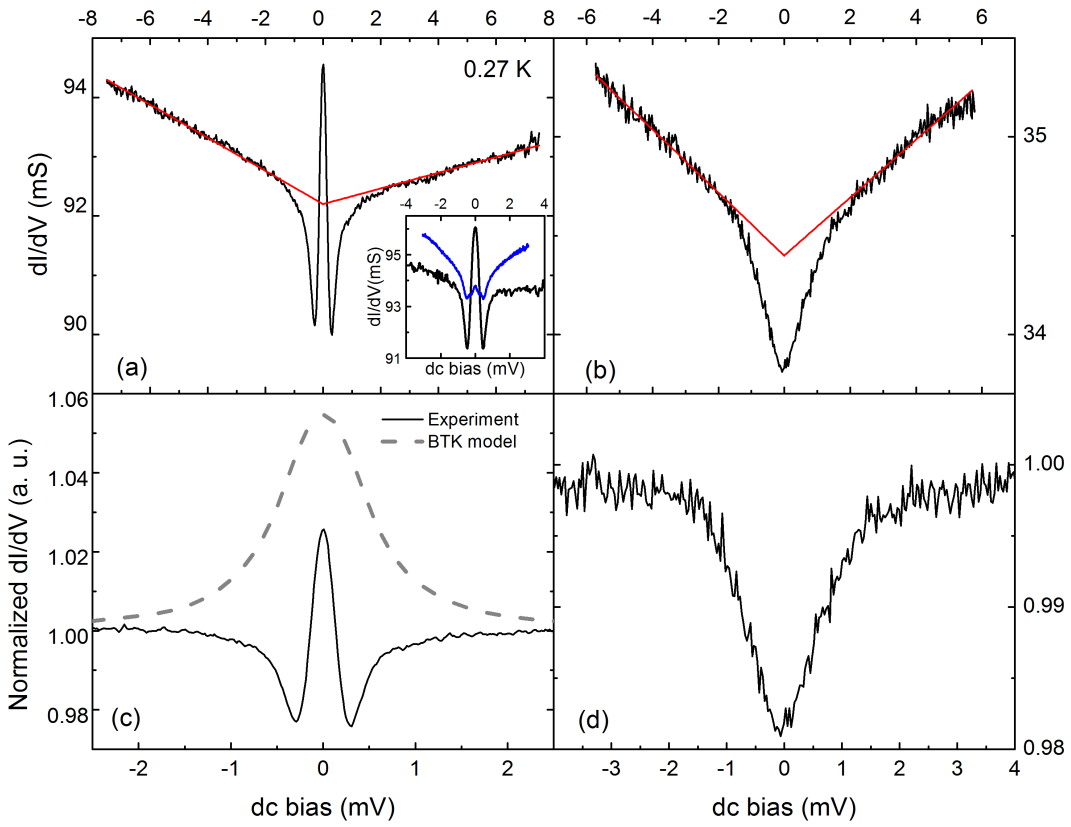

Figure 34: Typical dI/dV spectra of the point contact on (a) superconducting and (b) non-superconducting regions of the $Cu_{0.25}Bi_2Se_3$ surface. Inelastic tunneling through the interfacial barrier gives rise to the asymmetric, linear background (red lines) in the spectra. Inset: The background exhibits different slopes at different measurement locations, presumably due to different barrier strengths. Panels (c) and (d): Normalized dI/dV spectra after removal of the background in (a) and (b). The dashed line in panel (c) is an attempt to fit the data to the BTK model.

does not capture the two conductance dips at around the gap energy, and does not describe the data well.

It is worth noting that a linear background occurs in all the spectra that we have measured; it is nearly independent of temperature, and it varies from place to place on the $Cu_{0.25}Bi_2Se_3$ surface. Such a background was also observed in previous studies of $Cu_xBi_2Se_3$ [54, 89], but its origin was not explained. Here, we attribute it to inelastic tunneling at the tip/sample interface, following the model of Kirtley and coworkers [52, 53, 51]. This model was initially developed to explain a similar background in

the point contact spectra of high T_c cuprates. Since the $Cu_xBi_2Se_3$ sample is very sensitive to its environment, it is not surprising that oxidation barriers can form on the surface. A broad, flat distribution of energy-loss modes in the barrier could lead to the asymmetric, linear background appearing in the dI/dV spectra

$$(dI/dV)_{inelastic} \approx \int_0^{eV} F(E)dE. \tag{45}$$

Here, eV is the electron energy and $F(E) \approx$ constant is the spectral distribution of inelastic scattering modes. The removal of the linear background is necessary to determine the baseline for the normal state resistance for data fitting purposes. In Figs. 34(c) and 34(d), we plot the point contact spectra after removal of the background. The spectra are normalized with respect to the dI/dV values at high bias voltages (normal state) in order to compare with theory.

Figures 35(a) and 35(b) show the temperature and magnetic field dependence of the ZBCP after background subtraction. We find that the ZBCP only occurs at temperatures below the T_c of $Cu_{0.25}Bi_2Se_3$ and in a magnetic field below the upper critical field (B_{c2}=1.7 T for $Cu_{0.29}Bi_2Se_3$) [62], while the other type of spectral line shape, as shown in Figs. 34(b) and 34(d), is only weakly dependent on the temperature and the magnetic field (Fig. 35(c)). Therefore, we conclude that Figs. 34(a) and 34(b) represent the point contact spectra on the superconducting and non-superconducting regions of the sample, respectively. In addition, the spectra shown in Figs. 34(b) and 34(d) exhibit a pseudogap-like feature, *i.e.*, the reduction of the density of states at low bias voltages, which appears to be enhanced by the magnetic field [Fig. 35(c)]. Similar behavior has also been observed by Sasaki and coworkers [89] on the superconducting region at $T>T_c$, suggesting that the *non-superconducting* region referred herein may become superconducting at lower temperatures. We note that the observed magnetic field dependence is unexpected, markedly different from the pseudogap behavior in high-temperature superconductors. Further experimental and theoretical work is needed to understand this observation.

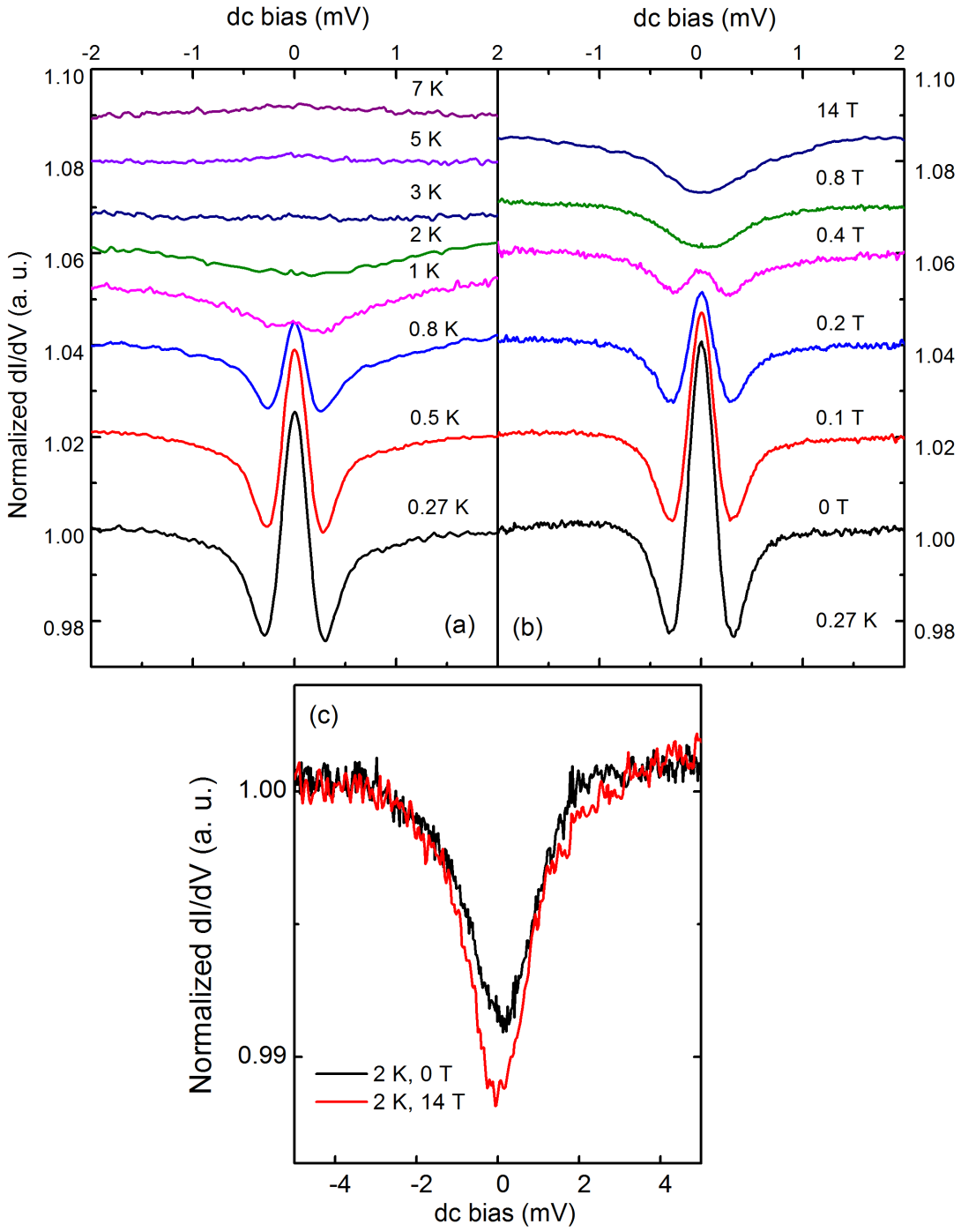

Figure 35: (a) Temperature and (b) magnetic field dependence of the point-contact spectra on the superconducting region of the sample. The spectra are normalized with respect to the dI/dV values at 4 mV, and shifted vertically for clarity. (c) dI/dV spectra obtained on the non-superconducting region of the sample at 0 T (black) and 14 T (red). An asymmetric, linear background has been subtracted from all the spectra. The magnetic field applied is perpendicular to the ab plane.

Before building a model based on the unconventional superconductivity to explain the ZBCP, it is prudent to discuss other possible scenarios. An often cited reason for the conductance enhancement at zero bias is the heating effect [97]. The argument is that in the diffusive/thermal regime of transport, the contact resistance comes from the Sharvin resistance R_{shar}, the Maxwell resistance R_{max} and the resistance of the superconductor, which is zero below the critical current. When the current through the point contact reaches the critical current, the resistance of the superconductor rapidly increases so a dip in the conductance appears. This effect from critical current can dominate the Andreev current in the diffusive/thermal regime. However, our measurement is done in the ballistic regime, because the typical contact resistance in our measurement is $\sim 10\ \Omega$, which translate to a contact diameter of $d \approx 12$ nm using the Sharvin formula Eqn. 38, and is much smaller than the electron mean free path l of gold ($l \approx 38$ nm at room temperature and is expected to be much longer at low temperatures). In addition, the conductance dips resulting from heating effect is usually located at bias voltage larger than the gap of the superconductor, which is not what we have observed. Finally, heating effects are not responsible for the asymmetric, linear background prominent at high bias voltages, because one would expect a decrease in conductance due to heating rather than an increase. As such, we deem the heating effect irrelevant to our case.

Reflectionless tunneling [10, 109] could also cause ZBCP in the differential conductance spectra. Reflectionless tunneling refers to the normal reflection of electrons at the N/S interface. Elastic scatterers in the normal metal generate multiple reflections at the interface. Due to the phase conjugation of electrons and holes, quantum interference happens constructively, and causes the enhancement of conductance above the classical value. However, a small magnetic field will destroy the phase conjugation and thus destroy the ZBCP. In our case the ZBCP survives to reasonably high magnetic field, so reflectionless tunneling cannot explain the ZBCP.

Yet another possible interpretation for the ZBCP is the magnetic scattering [4]. In this case, there are non-interacting magnetic impurities localized at the N/S interface. An electron can go from N to S with a spin exchange with impurity. The calculation done by Appelbaum [4] shows that this interaction will lead to an enhanced conductance. However, the ZBCP originated from this scenario will split in magnetic field [98], which is not observed in our measurements. So magnetic scattering is also irrelevant to our observation.

6.2 Extended BTK model for N/p-wave S interface

We now turn to the problem of building a quantitative model to explain the ZBCP seen in Fig. 34(c). Recently, advanced theories have been developed to describe the pairing symmetry of $Cu_xBi_2Se_3$ [28, 35, 89, 41]. Specifically, the microscopic model to describe the band structure of $Cu_xBi_2Se_3$ has been proposed [28]. It is shown that if both short and long range interactions are modeled, the symmetry of the Hamiltonian of the material supports four distinct kinds of superconducting gaps. To become a TSC, a superconductor must be: i) time-reversal-invariant (TRI), ii) centrosymmetric, iii) has odd-parity pairing symmetry with a full superconducting gap, and iv) encloses an odd number of TRI momenta by the Fermi surface. It turns out that three of the four possible gaps of $Cu_xBi_2Se_3$ are conventional, only one of them is topological. The exact nature of the superconducting gap of $Cu_xBi_2Se_3$ depends on whether the interorbital attraction exceeds the intraobital attraction, which is hard to control experimentally. Since the exact form of the interaction is not known in this material, theoretically one could assume pairing in all bands is possible and consider all possible types of pairing symmetries. This presents a challenge computationally. Experimentally, however, we find that no direct evidence of multiple bands is observed in point contact spectra, which suggests that an effective *single-band* model might be sufficient to describe $Cu_xBi_2Se_3$. This situation is similar to encountered

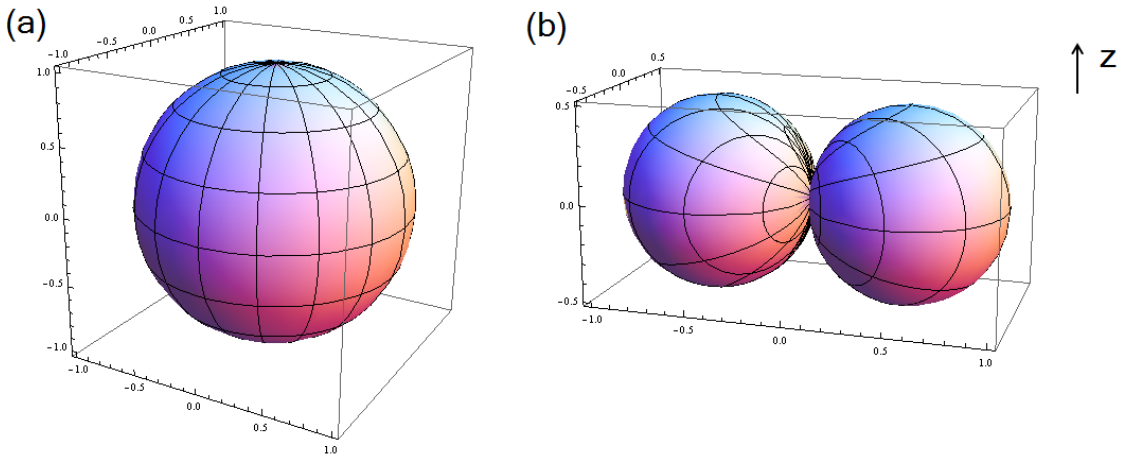

Figure 36: Illustration of the pairing potential for (a) s-wave and (b) a p-wave superconductor. For the conventional s-wave superconductor, the potential is spherically symmetric, and the Cooper pair carries no angular momentum. But for the p-wave superconductor, the potential is anisotropic.

high-temperature superconductors, where a somewhat complicated three-band theory is replaced by an effective single-band model [122] to explain experimental results. Therefore, it is enlightening to compare our data with existing single-band tunneling theory for triplet p-wave pairing.

For the sake of approximation, we ignore the hexagonal symmetry of the crystal and choose a simple triplet pairing potential:

$$\Delta = \begin{pmatrix} \Delta_{\uparrow\uparrow} & \Delta_{\uparrow\downarrow} \\ \Delta_{\downarrow\uparrow} & \Delta_{\downarrow\downarrow} \end{pmatrix} = \begin{pmatrix} \Delta_0 \sin\theta e^{i\phi} & 0 \\ 0 & 0 \end{pmatrix}, \tag{46}$$

where the up and down arrows are spin indices, Δ_0 is the superconducting gap in the bulk, and θ and ϕ are the polar angle and azimuthal angle, respectively. The pairing potential takes a 2×2 matrix form because different spin combination experiences different potential. An illustration of the anisotropy of the pairing potential is shown in Fig. 36.

Since the superconducting gap is anisotropic, it is necessary to consider the relative position of the tunneling direction and the gap. In the point contact measurement, the tip is in direct contact with the sample, so not only out-of-plane tunneling can

happen, but also in-plane tunneling, in which case the tunneling occurs from the tip to its neighboring sample surface areas (possibly through step edges). Figure 37 sketches the both kinds of tunneling configurations considered herein: (a) with tunneling in x direction and the N/S interface being the zy plane (in-plane tunneling), and (b) with tunneling in z direction and the N/S interface being the xy plane (out-of-plane tunneling).

A hallmark of the tunneling process at N/S interface when S is unconventional is the so called Andreev bound state [22]. Consider a normal metal/triplet superconductor interface as shown in Fig. 38. An electron in N is Andreev reflected at the N/S interface by a pairing potential having, say, positive sign. The retroreflected hole is then specularly reflected at the boundary of N, and incident to the N/S interface again. This time the hole is Andreev reflected as an electron by the pairing potential with negative sign. The reflected electron traces back the trajectory of the hole and completes the cycle. The electron is thus bounded in this loop with two Andreev reflections and so comes the name Andreev bound state. It can be shown [24] that the energy of the ABS is discrete and takes the form

$$E_n = \frac{\hbar\pi v_F}{2d_N}(n + \frac{1}{2}), \tag{47}$$

where v_F is the Fermi velocity, d_N is the thickness of the normal metal, and n is an integer number. This result is obtained on a topologically trivial superconductor, and there is no energy level at $E = 0$. However, in TSC, due to the additional π Berry phase, the energy level becomes

$$E_n = \frac{\hbar\pi v_F}{2d_N}n, \tag{48}$$

with a zero energy state, in which case the conditions for having Majorana fermions are met. In the dI/dV conductance spectrum, the zero energy state will manifest itself as a conductance peak at zero bias voltage. While this is a tempting result, unfortunately for any realistic system d_N is a macroscopic length, so the separation

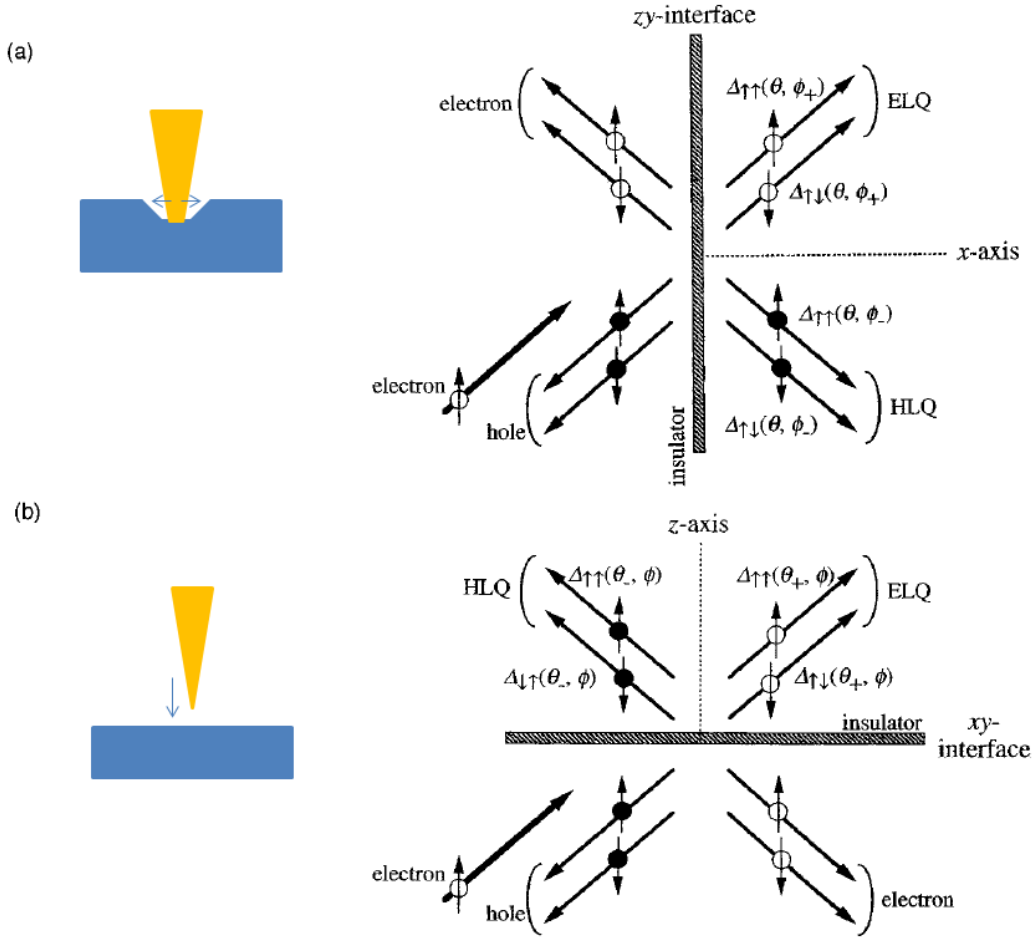

Figure 37: Schematics of reflection and transmission processes of quasiparticles at N/S interface for (a) in-plane tunneling and (b) out-of-plane tunneling. There are four processes at the interface: normal reflection of electrons, Andreev reflection of holes, and transmission of electron like quasiparticles (ELQ) and hole like quasiparticles (HLQ). Open circles represent electrons, solid circles represent holes, and arrows represent spin directions. θ and ϕ are the polar and azimuthal angles, respectively. Right panel of the figure is adapted from Ref. [118].

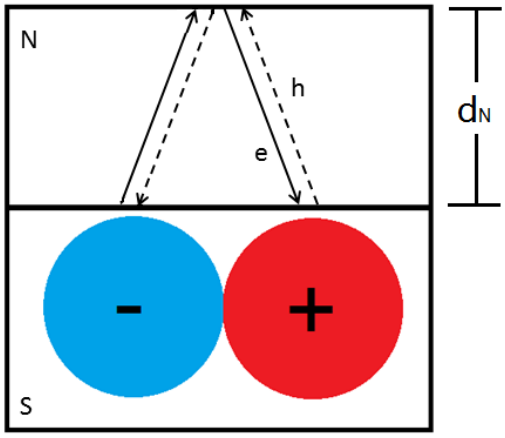

Figure 38: Formation of the Andreev bound state. Two Andreev reflections happen at the N/S interface and form a complete loop. d_N is the length of the normal metal. Letter e marks the electron and h marks the hole.

between energy levels $\hbar\pi v_F/2d_N \sim 0$, and the energy spectrum of the ABS is quasi-continuous. This means there is practically no difference between Eqn. 47 and 48. In fact, even in the topologically trivial ABS, the ZBCP will show up in the conductance spectra [43].

To quantitatively calculate the conductance spectra, the standard BTK model needs to be extended. As in the BTK model, we still assume the interface potential is a Dirac delta function, and there is only elastic scattering so k_F is the same on either side. Then the boundary condition at the N/S interface remains the same. Unlike the BTK model, the gap function Δ in the BdG equation is no longer a constant. Also, the conductance σ is dependent on the angles θ and ϕ, which needs to be considered in the trial solution (compared to Eqn. 10a and 10b):

$$f(\mathbf{k},\mathbf{r}) = \tilde{u}(k,r)e^{i\mathbf{k}\cdot\mathbf{r}-iEt/\hbar}, \tag{49a}$$

$$g(\mathbf{k},\mathbf{r}) = \tilde{v}(k,r)e^{i\mathbf{k}\cdot\mathbf{r}-iEt/\hbar}. \tag{49b}$$

The rest of the calculation is in principle the same as the BTK model, where the boundary conditions are matched to get the tunneling coefficients A, B, C, and D, except that one has to carry out one more integration over all possible transmission/

reflection directions. We follow the calculations of Yamashiro and coworkers [118], where the normalized conductance is evaluated as the following for in-plane tunneling:

$$\sigma(E) = \frac{\int_{\pi/2-\delta}^{\pi/2}\int_{-\pi/2}^{\pi/2}(\sigma_{S\uparrow}+\sigma_{S\downarrow})\sigma_N \sin^2\theta\cos\phi d\theta d\phi}{\int_{\pi/2-\delta}^{\pi/2}\int_{-\pi/2}^{\pi/2} 2\sigma_N \sin^2\theta\cos\phi d\theta d\phi}, \tag{50}$$

and for out-of plane tunneling:

$$\sigma(E) = \frac{\int_{\pi/2-\delta}^{\pi/2}\int_{0}^{2\pi}(\sigma_{S\uparrow}+\sigma_{S\downarrow})\sigma_N \sin\theta\cos\theta d\theta d\phi}{\int_{\pi/2-\delta}^{\pi/2}\int_{0}^{2\pi} 2\sigma_N \sin\theta\cos\theta d\theta d\phi}, \tag{51}$$

where $\sigma_{S\uparrow}$ and $\sigma_{S\downarrow}$ are the conductance of the superconducting state for spin up and spin down particles respectively, σ_N is the conductance of the normal state, and E is the energy of the quasiparticle measured from the Fermi energy. Notice that the integration is done not over the entire space, but limited to $\pi/2-\delta < \theta < \pi/2$, which means that we are restricting the z component of the crystal momentum, in order to get a two-dimensional Fermi surface.

The normal state tunneling conductance is given by

$$\sigma_N = \begin{cases} \frac{\sin^2\theta\cos^2\phi}{\sin^2\theta\cos^2\phi+Z^2}, & \text{in-plane} \\ \\ \frac{\cos^2\theta}{\cos^2\theta+Z^2}. & \text{out-of-plane} \end{cases} \tag{52}$$

The conductance of the superconducting state for our chosen gap function (Eqn. 46) is

$$\sigma_{S\uparrow} = \frac{1+\sigma_N|\Gamma|^2+(\sigma_N-1)|\Gamma|^4}{|1-e^{-2i\phi}(\sigma_N-1)\Gamma^2|^2}, \tag{53}$$

$$\Gamma = \frac{E-\sqrt{E^2-\Delta_0^2\sin^2\theta}}{|\Delta_0\sin\theta|}, \tag{54}$$

for in-plane tunneling, and

$$\sigma_{S\uparrow} = \frac{1+\sigma_N|\Gamma|^2+(\sigma_N-1)|\Gamma|^4}{|1+(\sigma_N-1)\Gamma^2|^2}, \tag{55}$$

for out-of-plane tunneling. In the meantime, $\sigma_{S\downarrow}$ is unity because of the lack of effective pair potential. With these information, Eqn. 50 and 51 can be evaluated,

the final step is to integrate over all energy E to get the normalized conductance spectra that can be measured experimentally:

$$dI/dV = D_0 \int_{-\infty}^{+\infty} dE\ \sigma(E) \left[\frac{-\partial f(E+eV)}{\partial E} \right], \tag{56}$$

where $f(E)$ is the Fermi-Dirac distribution as usual, and we added a scale parameter D_0 to rescale the calculated spectra with respect to measured data. Physically, this scale parameter can be explained as the transmission probability of quasiparticles along the contact normal direction [64].

In Fig. 39 we plot some representative results of Eqn. 50 to 55 at different barrier strength Z. Left panel shows the results for in-plane tunneling, and right panel shows the results for out-of-plane tunneling. Calculations are done assuming the incident electrons from the N side have equal probabilities of spin up and spin down, and δ is chosen as $\pi/20$ to get a 2D Fermi surface. Note that for the in-plane tunneling, there is a robust ZBCP, regardless of the barrier strength. Moreover, the magnitude of the zero bias conductance *increases* with the barrier strength, which is drastically different from the result of standard BTK model (recall the Z dependence in Fig. 16). For the out-of-plane tunneling on the other hand, there is no ZBCP, and the conductance spectra look much like the pure tunneling spectrum. However, the zero bias conductance in this case converges to 0.5 at high Z, rather than 0. This is because of the density of states for spin down quasiparticles, as we have chosen $\Delta_{\downarrow\downarrow} = 0$. This behavior is peculiar to nonspherical superconducting gaps.

Insights can be gain about the origin of the ZBCP by investigating Eqn. 53 to 55. At zero bias, $\Gamma(0) = \sqrt{-\Delta_0^2 \sin^2\theta}/|\Delta_0 \sin\theta| = i$, if $\phi = 0$ and Z is large, then $\sigma_N \sim 0$, and the denominator of Eqn. 53 vanishes. This does not happen for Eqn. 55. This divergence causes the enhancement of $\sigma(0)$ in Eqn. 50 for in-plane tunneling. It should be noted that this ZBCP is a universal property of anisotropic superconductors, if the pair potentials change sign at the Fermi surface [118]. For example, the ZBCP is also predicted and observed in point contact spectra of d-wave [104, 21] superconductors.

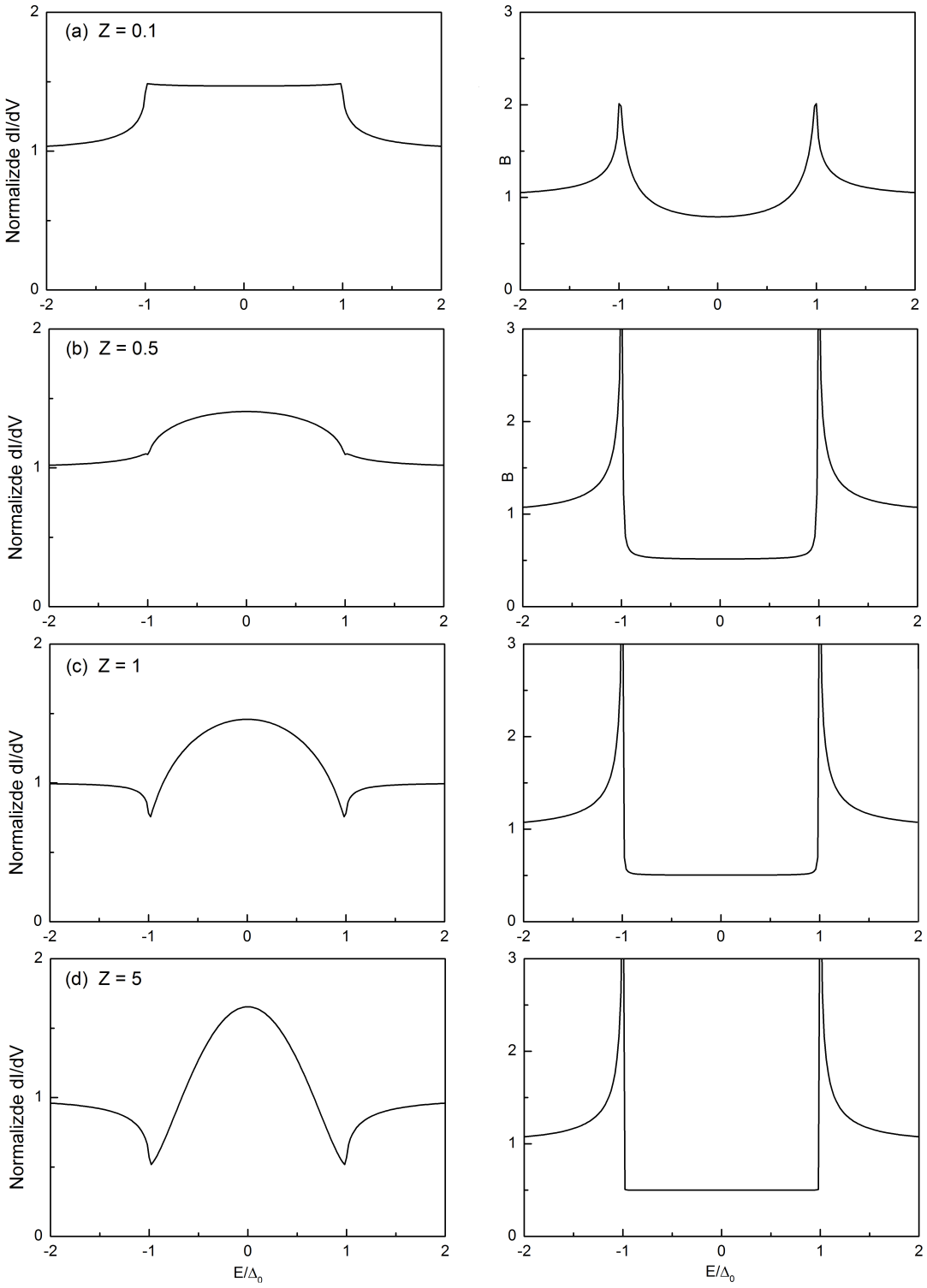

Figure 39: Calculated normalized conductance spectrum of normal metal/ triplet superconductor interface, with (left panel) in-plane tunneling and (right panel) out-of-plane tunneling. The spectrum is calculated at different interface barrier strength, from (a) $Z = 0.1$ to (d) $Z = 5$.

Thus, the observation of ZBCP alone only suggests unconventional superconductivity, but cannot be used to determine the exact form of the pairing potential.

The best fit using the in-plane tunneling model described above to the data in Fig. 34(c) is shown in Fig. 40(a). The ZBCP and the positions of the dI/dV minima are well captured using D_0=0.071, Δ_0=0.32 meV, and Z=10. The good agreement between the data and the model signifies the unconventional nature of the superconductivity in $Cu_xBi_2Se_3$. There are some discrepancies between the modeled curve and the data, and there could be several reasons for this:

i) The simple linear background modeled using Eqn. 45 is only an approximation. A more comprehensive model considering the distribution of inelastic scattering current [51] will alter the extracted spectrum slightly.

ii) Inelastic scattering events also cause a finite quasiparticle lifetime. This can be coped by adding an imaginary part to the quasiparticle energy in the BTK model [81], and will cause a broadening effect on the spectrum.

iii) The simple pairing potential described in Eqn. 46 ignored the crystal symmetry and did not consider gap nodes, a comprehensive model specifically designed for the material may capture the observed data better.

One useful piece of information we can extract from the model fit is the superconducting gap in the bulk Δ_0. We repeat the fitting process to the dI/dV spectra measured at different temperature $T < T_c$. We find that the extracted gap values are always slightly larger than the corresponding energies of the dI/dV minima in the point contact spectra. Figure 40(b) plots the temperature dependence of $\Delta_0(T)$, which appears linear in temperature. It is well known from the BCS theory that for an s-wave superconductor, the temperature dependence of the gap is the solution to

$$\int_0^{\hbar\omega_c} \frac{\tanh\frac{1}{2}\beta(\xi^2+\Delta^2)^{1/2}}{(\xi^2+\Delta^2)^{1/2}} d\xi = \text{constant}, \tag{57}$$

where $\hbar\omega_c$ is some cutoff energy away from Fermi energy, and $\beta = 1/k_BT$. This temperature dependence is plotted in Fig. 40(b) as the red dashed line. We see the

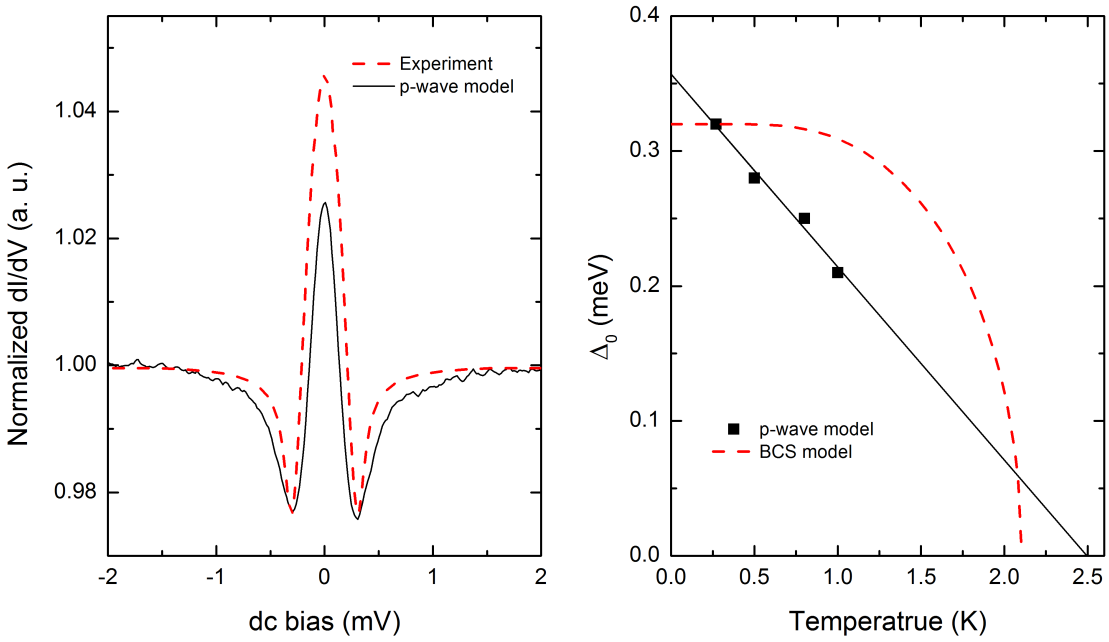

Figure 40: (a) Fit using the single-band p-wave model described in the main text to the data in Fig. 34(c). (b) Temperature dependence of the superconducting gap (filled squares) extracted from the single-band p-wave model, and compared with the expected values from the s-wave BCS theory (dashed red line). The solid black line is guidance to the eyes.

observed temperature dependence of $\Delta_0(T)$ of $Cu_xBi_2Se_3$ clearly cannot be described by the s-wave model.

6.3 Point contact spectroscopy of $Sn_{1-x}In_xTe$ using gold tip

Experiment evidences we gathered on $Cu_xBi_2Se_3$ point to unconventional superconductivity. However the sample suffers from an important material issue, that is its inhomogeneity. The volume fraction is only 35%, and as we observed in the point contact spectra, not all locations on the sample surface are superconducting (Fig. 34). Recently $Sn_{1-x}In_xTe$ single crystals have been proposed as another possible topological superconductor with odd-parity pairing [90, 92]. This material has a much better crystal quality [25], shows no sign of oxidation in air, and has sharper superconducting transition [Fig. 41 (a)]. We carry out the point contact spectroscopy study of the

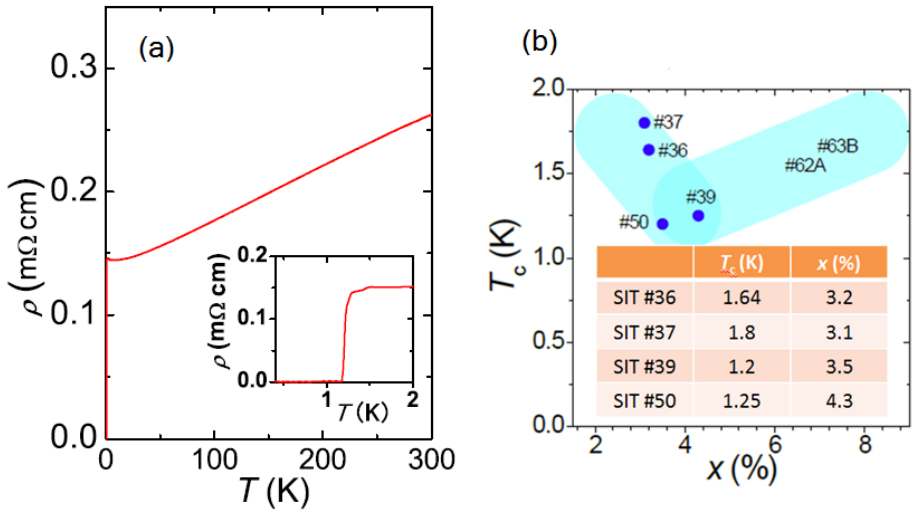

Figure 41: (a) (adapted from Ref. [90]) Temperature dependence of the resistivity of a $Sn_{0.955}In_{0.045}Te$ sample. The inset is a magnified view near 1 K, where a sharp superconducting transition is evident. (b) Summary of the characterization results of several large-size $Sn_{1-x}In_xTe$ single crystals. As the concentration of In increases, the T_c first decreases then increases.

gold/$Sn_{1-x}In_xTe$ junctions. The $Sn_{1-x}In_xTe$ samples are grown by Dr. Yoichi Ando's group at the Osaka University. Figure 41 (b) summarizes the material characterization results for a patch of samples, from which several large-size crystals (suited for point contact spectroscopy measurements) are selected.

The temperature and magnetic field dependences of the conductance spectra at the gold/$Sn_{1-x}In_xTe$ interface are presented in Fig. 42. We observed a pronounced ZBCP on all samples we tested and at all locations we measured (with interface resistance from a few ohms to one hundred ohms). This reassures us that the ZBCP is not sporadic behavior but an intrinsic property of the materials. Comparing the conductance spectra on $Sn_{1-x}In_xTe$ to those taken on $Cu_xBi_2Se_3$ (Fig. 35), we find that the overall line shapes are very similar, and the conductance dips at $\sim \pm 0.2$ mV match the superconducting gap of $Sn_{1-x}In_xTe$. However, one drastic difference is the amplitude of the ZBCP. On $Cu_xBi_2Se_3$, the zero bias conductance is only a few percentage higher than the normal state conductance, but on $Sn_{1-x}In_xTe$, it is

more than 3 times the normal state conductance. A similar behavior was observed on $Sn_{1-x}In_xTe$ by Sasaki and coworkers using a soft point contact technique [90], and the reason was not explained. Within the BTK framework, even in the case of perfect Andreev reflection, the zero bias conductance can only go up to twice as much as the normal state conductance. As such, the unusual amplitude of the ZBCP on $Sn_{1-x}In_xTe$ is another sign of the unconventional superconductivity.

In the p-wave model we used for the $Cu_xBi_2Se_3$, we only considered the flat band dispersion as a function of the momentum parallel to the surface. To fully understand the ZBCP, a 3D tunneling theory specifically considering the band structure of the TSCs is needed. Yamakage and coworkers did some pioneering work in this area [116, 117]. They calculated the tunneling conductance of normal metal and $Cu_xBi_2Se_3$ junctions for the possible pairing symmetries. They showed that in the presence of ABSs (and thus MFs), it is possible to have ZBCP even if the material has a 3D full superconducting gap, and the amplitude of the ZBCP is not limited to twice the normal state conductance. The band structures and pairing symmetries of $Cu_xBi_2Se_3$ and $Sn_{1-x}In_xTe$ are very similar, so their result is qualitatively applicable to explain the conductance spectra we observed on $Sn_{1-x}In_xTe$, although a quantitative fit to the data is difficult due to computational complexity.

Finally, we note that, instead of a perpendicular magnetic field, it is very enlightening to apply a parallel magnetic field (parallel to the sample surface) and measure the magnetic field dependence of the point contact spectra. Such geometry allows for the study of the effects of magnetic fields on the electron spins without affecting their orbital motion, in which case the interplay of Zeeman fields and spin-orbit fields with components in the same direction may produce novel parity violating superconductivity and quasiparticle excitations [95, 102]. According to the calculation done by Svetlichnyy and coworkers [102], the density of states for spin up and spin

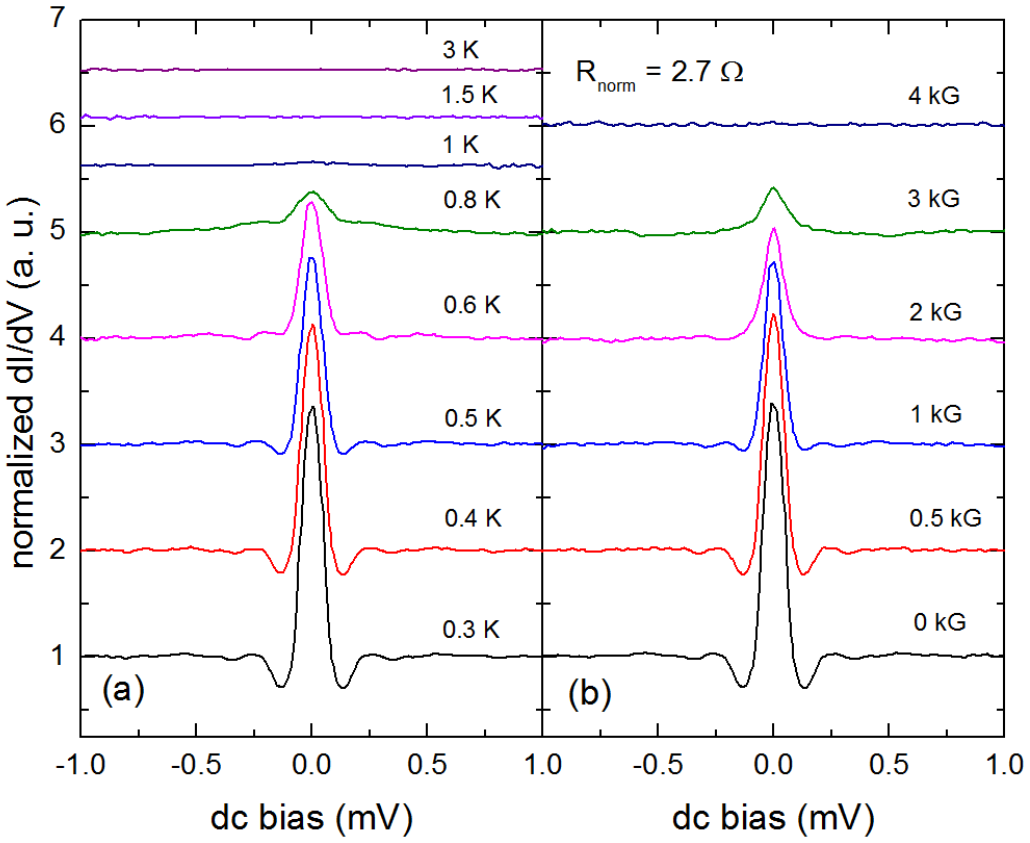

Figure 42: (a) Temperature and (b) magnetic field dependences of the point contact spectra at the gold/$Sn_{1-x}In_xTe$ interface.

down electrons in a centrosymmetric superconductor is non-degenerate when a parallel magnetic field is turned on, which in principle would give rise to a magnetic field dependent splitting of the coherent peaks (or dips) in the point contact spectra. We performed such a parallel magnetic field measurement as shown in Fig. 43, the measurement is done using a gold tip on the $Sn_{1-x}In_xTe$ sample. We see a smooth depression of the coherence dips at around 0.75 meV but there is no sign of any splitting as predicted by the theory. There could be several reasons for this: i) The point contact spectroscopy measurement is not spin-resolved. A spin-resolved measurement such as spin-ARPES or spin-STS is needed to observe the difference in the density of states. ii) The magnetic field required to observe the splitting is higher than the critical field of $Sn_{1-x}In_xTe$. If this is the case, a different material system is needed

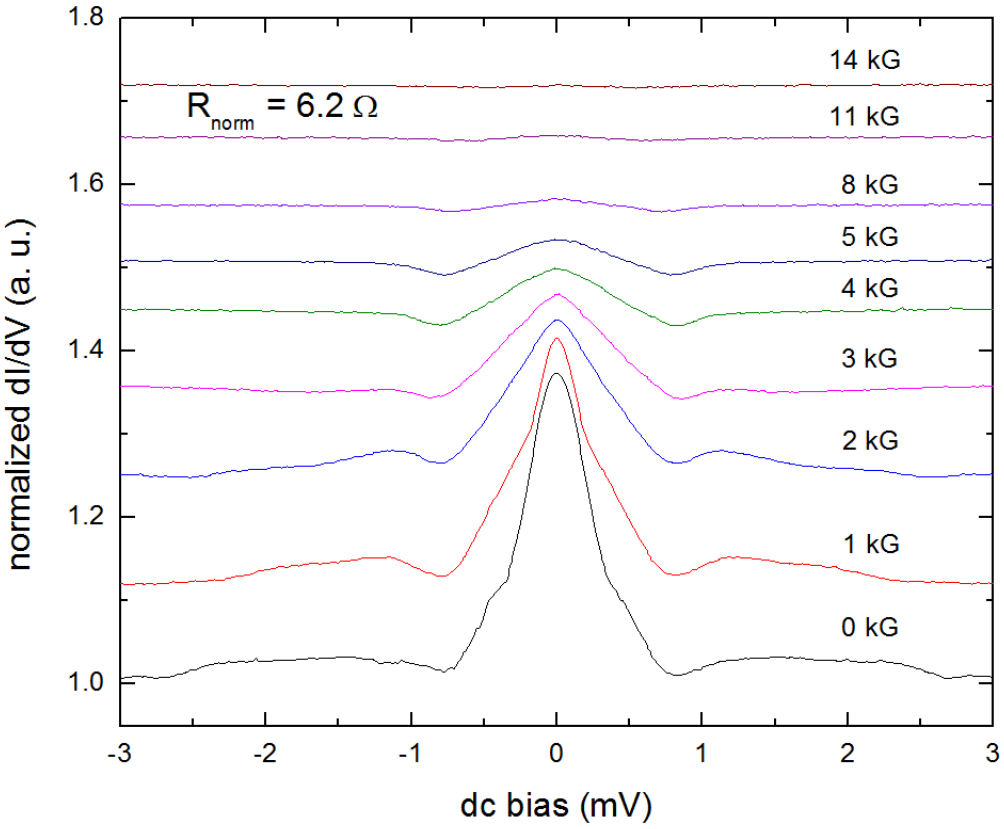

Figure 43: Point contact spectra at the gold/$Sn_{1-x}In_xTe$ interface with a magnetic field applied parallel to the surface of $Sn_{1-x}In_xTe$.

to observe the stated effect. iii) The model built in Ref. [102] used a 2D Hamiltonian, thus the result may not be applicable to the 3D TSCs.

6.4 Point contact spectroscopy of TSCs using niobium tip

When an s-wave superconductor (e.g., Nb) is in close proximity to a p- or d-wave superconductor, an unusual Josephson effect may occur due to the incompatibility of the pairing symmetries. Specifically, for a conventional s-wave Josephson junction, the supercurrent between two s-wave superconductors is expected to first increase and then saturate as the temperature is lowered below the T_c. For an s-wave/d-wave junction, however, the supercurrent may decrease depending on the relative

orientation of the anisotropic d-wave "lobes" of the order parameter of the unconventional superconductor with respect to the symmetric s-wave order parameter of the conventional superconductor [100]. Since supercurrent appears as a sharp zero-bias conductance peak in point contact spectra, a decrease in supercurrent can be revealed in the reduction of the peak height or the emergence of a dip.

In this section we explore the point contact spectroscopy measurement of TSCs using niobium tip. Niobium is a type-II s-wave superconductor, with a relatively high T_c of 9.3 K. As a control experiment, we first measured the point contact conductance spectra using a niobium tip on a tantalum thin film. Tantalum is also an s-wave superconductor, with a T_c of $\sim$4 K for bulk material and 1.4 K for our thin film [121]. The tantalum film is deposited on a piece of glass using electron beam deposition, to ensure film quality. The V-I curve of the Nb/Ta junction is shown in Fig. 44. One can see that the V-I characteristics deviates from the linear Ohmic behavior below the T_c of Ta. Under such condition, current can flow dissipationlessly through the junction, even when no bias voltage is applied. This dissipationless current is called the supercurrent. If the $Cu_xBi_2Se_3$ and $Sn_{1-x}In_xTe$ samples also have s-wave pairing symmetry, then we would expect to see a similar supercurrent behavior from the point contact spectroscopy.

Figure 45 shows our data for the Nb/$Cu_{0.25}Bi_2Se_3$ interface. We did not observe the zero resistance supercurrent state as in the Nb/Ta junction. Instead, when the normal state contact resistance is relatively high [Fig. 45(a) and (b)], we saw a clear ZBCP. Interestingly, as we go to lower normal state resistance [Fig. 45(c), R_N = 35 Ω], the amplitude of the peak shows a non-monotonic temperature dependence. That is, as temperature increases from 0.28 K to 0.8 K, the zero bias conductance becomes larger, but as the temperature further increases, the peak height decreases again. In the inset of Fig. 45(c), we plot the temperature dependence of the zero bias conductance, where the non-monotonic behavior can be clearly seen.

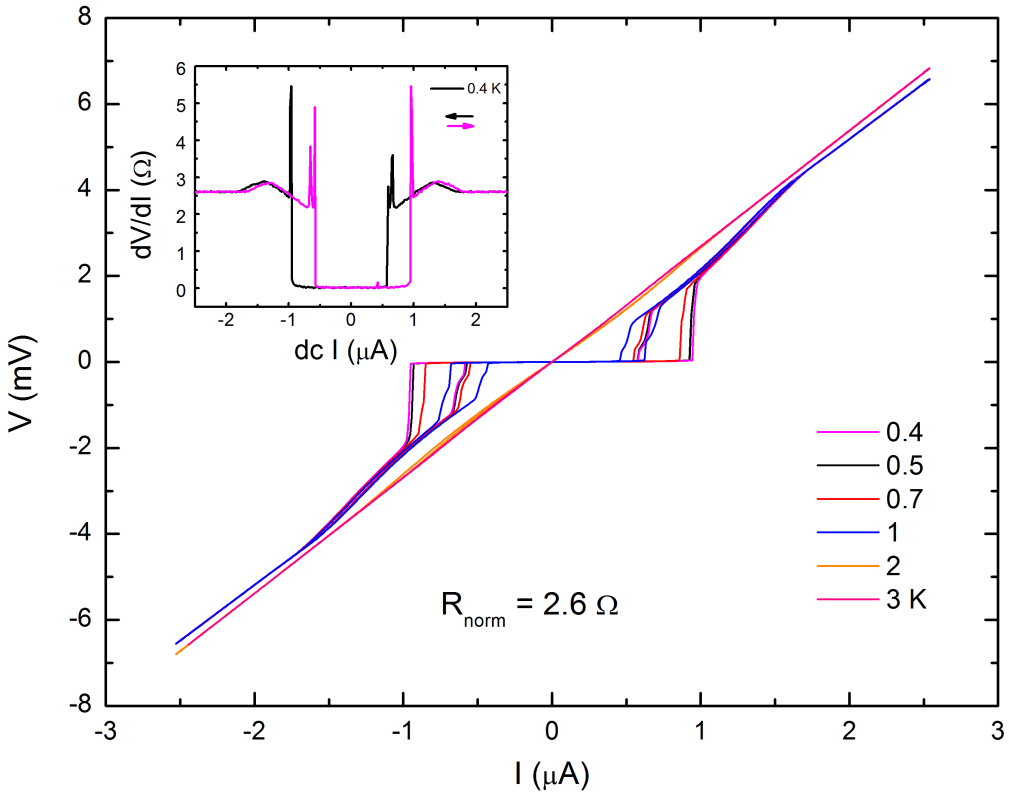

Figure 44: Point contact spectroscopy data using a niobium tip on electron beam deposited tantalum thin film. The main panel plots the V-I curve of the point contact. Under the T_c of tantalum, the V-I curve deviates from the Ohm's law, and supercurrent is evident (current flowing through the junction without a voltage drop). The inset is the resistance of the junction as a function of the dc current. When current is smaller than the critical current, the junction has zero resistance. The black curve and pink curve are taken with opposite current sweeping direction and there is hysteresis.

When the tip is further pressed down to the sample, and the contact resistance becomes smaller [$R_N = 25\ \Omega$, Fig. 45(d)], the suppression of the zero bias conductance becomes more evident. A clear zero-bias conductance dip is observed at low temperatures. When the temperature is increased, this dip first becomes to a pronounced peak at ~ 1 K and then vanishes at a higher temperature. Such a conductance dip and non-monotonic temperature dependence are very similar to the observations on *d*- wave superconductor $Bi_2Sr_2CaCu_2O_8$ [100] and signify the unconventional superconductivity of $Cu_{0.25}Bi_2Se_3$.

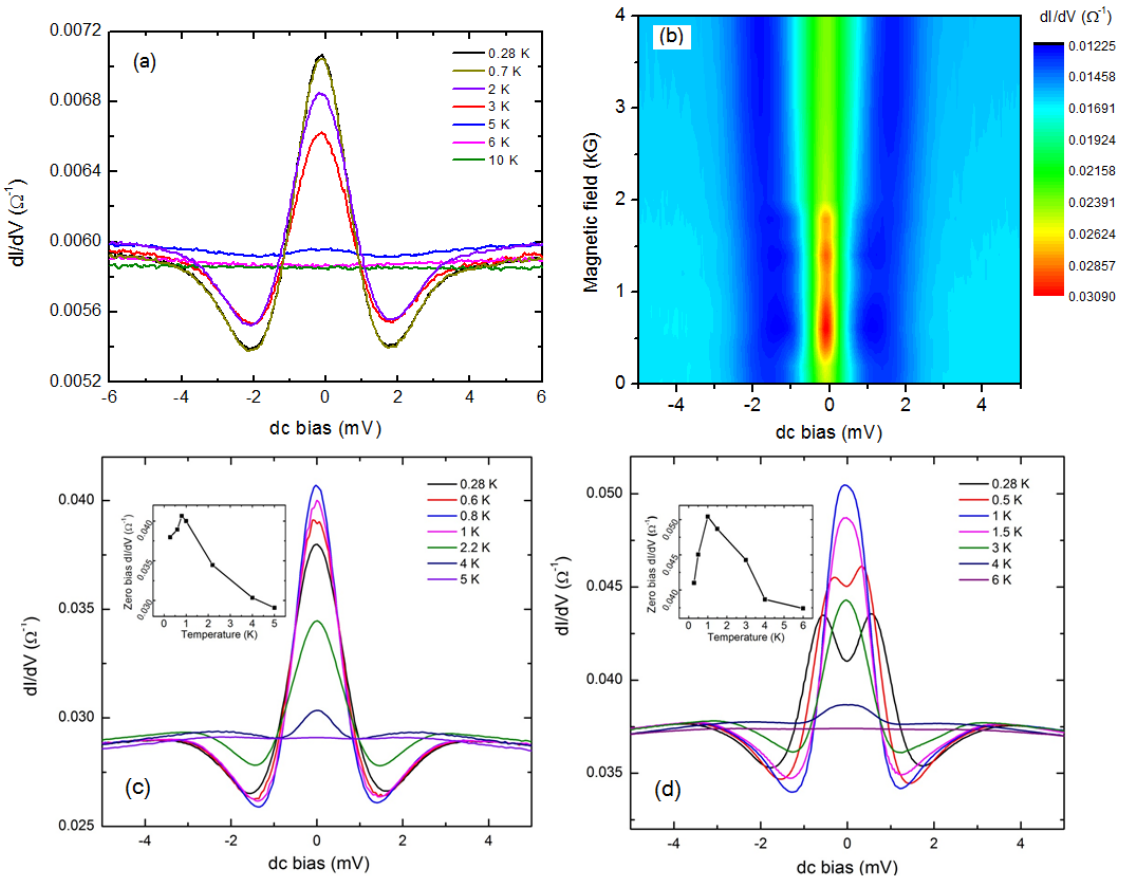

Figure 45: Point contact spectra at the Nb/$Cu_{0.25}Bi_2Se_3$ interface. Panel (a) and (b) shows the temperature and magnetic field dependence of the point contact spectra with relatively high normal state resistance [170 Ω for (a) and 62 Ω for (b)]. Panel (c) and (d) shows the temperature dependence of the point contacts spectra with normal state resistance of 35 Ω and 25 Ω, respectively. The insets are the temperature dependence of the zero bias conductance, where a non-monotonic behavior can be clearly seen.

Figure 46 shows the data taken on an as-grown facet of a $Sn_{0.965}In_{0.035}Te$ single crystal. Panel (a) is the temperature dependence and panel (b) is the magnetic field dependence. Compared with the point-contact spectra of $Cu_xBi_2Se_3$, we reveal several relatively small spectral features within the superconducting gap of Nb ($\Delta \approx 1.4$ meV) including the dI/dV dips around ~ 0.16 mV and ~ 0.62 mV. These spectral features become stronger at low temperatures and may be attributed to multiple Andreev reflections between the two superconductors. When a magnetic field is applied, these features vanish at ~ 5 kG with the coherent peaks of Nb at 1.6 mV, while a robust zero-bias conductance peak remains up to 3 T. Oddly, in this case we did not observe the non-monotonic temperature dependence of the zero bias conductance, as in the case of $Cu_{0.25}Bi_2Se_3$. The rich spectral features in Fig. 46 and their mysterious magnetic field dependence invite further investigations.

We believe that the niobium tip point contact spectroscopy measurements provide valuable information on the pairing mechanism of topological superconductors. The ongoing debate [67, 80] about the origin of the ZBCP has been focused on measurements using normal metal tips. Our data provides a new perspective on the problem and further theoretical explorations are needed to fully resolve this matter.

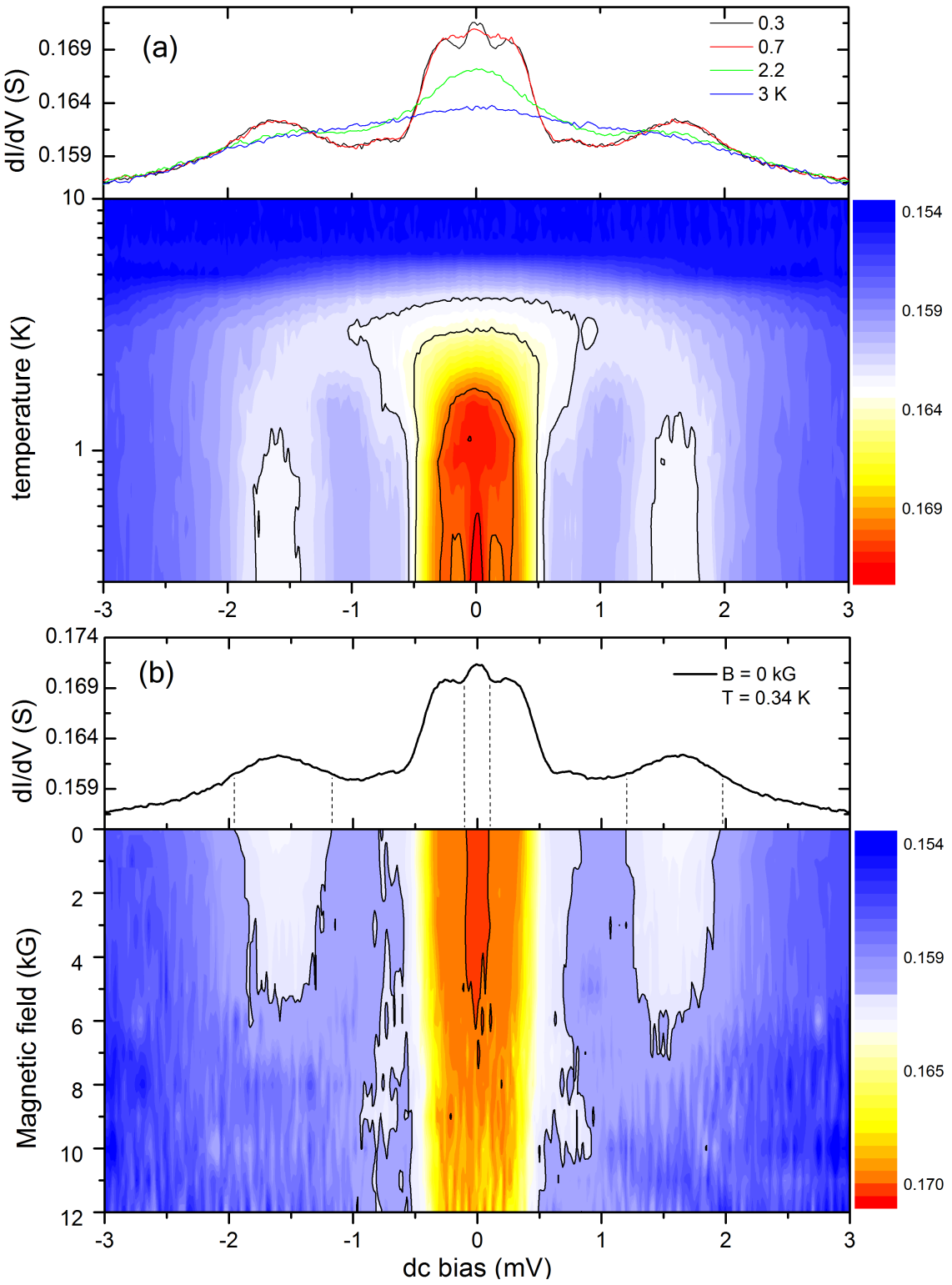

Figure 46: (a) Temperature and (b) magnetic field dependences of the point contact spectra taken at a Nb/$Sn_{0.965}In_{0.035}Te$ interface. The bottom part of each panel is a 2D contour plot of the dependence. Dashed guidelines are added to reveal the evolution of the small features in the spectra.

CHAPTER VII

CONCLUSION

We explored some fundamental material properties of TI Bi_2Se_3 and Sb_2Te_3, including the temperature dependence of the thermal expansion coefficient and the Raman-active optical phonons. The majority of the dissertation is devoted to the point contact studies of the topological superconductivity. Our home made point contact system is capable of acquiring the spectra using both normal metal gold tip and superconducting niobium tip in the ballistic transport regime. For the Nb/Bi_2Se_3 interface, we observed proximity induced superconductivity. We extended the standard BTK model using a Hamiltonian appropriate for the TI Bi_2Se_3 to provide a possible explanation for the ZBCP observed in the point contact spectra. For the gold/$Cu_xBi_2Se_3$ and gold/$Sn_{1-x}In_xTe$ interfaces, we observed a robust ZBCP, which is consistent with a p-wave BTK model explanation. We observed a non-monotonic temperature dependence of the ZBCP for the Nb/$Cu_xBi_2Se_3$ interface, which further signifies the unconventional nature of the superconductivity of $Cu_xBi_2Se_3$; while for the Nb/$Sn_{1-x}In_xTe$ interface, no non-monotonic dependence was observed. Our result is strongly in favor of an odd parity paring for $Cu_xBi_2Se_3$, but more theoretical work is needed to fully understand the spectra, especially for the case of $Sn_{1-x}In_xTe$. Future work directions include performing point contact spectroscopy measurements on the TSCs using d-wave tip, to study the interaction between superconductors with different pairing symmetries, and extend the BTK model to TSCs, using an appropriate Hamiltonian.

REFERENCES

[1] Ando, T., Nakanishi, T., and Saito, R., "Berry's phase and absence of back scattering in carbon nanotubes," *Journal of the Physical Society of Japan*, vol. 67, no. 8, pp. 2857–2862, 1998.

[2] Ando, Y., "Topological insulator materials," *Journal of the Physical Society of Japan*, vol. 82, no. 10, 2013.

[3] Andreev, A., "The thermal conductivity of the intermediate state in superconductirs," *Journal of Experimental and Theoretical Physics*, vol. 19, no. 5, p. 1228, 1964.

[4] Appelbaum, J., ""$s-d$" exchange model of zero-bias tunneling anomalies," *Phys. Rev. Lett.*, vol. 17, pp. 91–95, Jul 1966.

[5] Balkanski, M., Wallis, R. F., and Haro, E., "Anharmonic effects in light scattering due to optical phonons in silicon," *Phys. Rev. B*, vol. 28, pp. 1928–1934, Aug 1983.

[6] Bardeen, J., Cooper, L., and Schrieffer, J., "Microscopic theory of superconductivity," *Phys. Rev.*, vol. 106, pp. 162–164, Apr 1957.

[7] Barnes, J., Rayne, J., and Jr, R. U., "Lattice expansion of bi2te3 from 4.2 k to 600 k," *Physics Letters A*, vol. 46, no. 5, pp. 317 – 318, 1974.

[8] Beenakker, C., "*Colloquium* : Andreev reflection and klein tunneling in graphene," *Rev. Mod. Phys.*, vol. 80, pp. 1337–1354, Oct 2008.

[9] Beenakker, C. W. J., "Specular andreev reflection in graphene," *Phys. Rev. Lett.*, vol. 97, p. 067007, Aug 2006.

[10] Beenakker, C. W. J. and van Houten, H., "Josephson current through a superconducting quantum point contact shorter than the coherence length," *Phys. Rev. Lett.*, vol. 66, pp. 3056–3059, Jun 1991.

[11] Bernevig, B. and Zhang, S.-C., "Quantum spin hall effect," *Phys. Rev. Lett.*, vol. 96, p. 106802, Mar 2006.

[12] Bernevig, B. A., Hughes, T. L., and Zhang, S.-C., "Quantum spin hall effect and topological phase transition in hgte quantum wells," *Science*, vol. 314, no. 5806, pp. 1757–1761, 2006.

[13] Blonder, G. and Tinkham, M., "Metallic to tunneling transition in cu-nb point contacts," *Phys. Rev. B*, vol. 27, pp. 112–118, Jan 1983.

[14] Blonder, G., Tinkham, M., and Klapwijk, T., "Transition from metallic to tunneling regimes in superconducting microconstrictions: Excess current, charge imbalance, and supercurrent conversion," *Phys. Rev. B*, vol. 25, pp. 4515–4532, Apr 1982.

[15] Chen, X., Zhou, H., Kiswandhi, A., Miotkowski, I., Chen, Y., Sharma, P., Sharma, A. L., Hekmaty, M., Smirnov, D., and Jiang, Z., "Thermal expansion coefficients of bi2se3 and sb2te3 crystals from 10 k to 270 k," *Applied Physics Letters*, vol. 99, no. 26, p. 261912, 2011.

[16] Chen, Y. L., Analytis, J. G., Chu, J.-H., Liu, Z. K., Mo, S.-K., Qi, X. L., Zhang, H. J., Lu, D. H., Dai, X., Fang, Z., Zhang, S. C., Fisher, I. R., Hussain, Z., and Shen, Z.-X., "Experimental realization of a three-dimensional topological insulator, bi2te3," vol. 325, no. 5937, pp. 178–181, 2009.

[17] Chen, Y. L., Chu, J.-H., Analytis, J. G., Liu, Z. K., Igarashi, K., Kuo, H.-H., Qi, X. L., Mo, S. K., Moore, R. G., Lu, D. H., Hashimoto, M., Sasagawa, T., Zhang, S. C., Fisher, I. R., Hussain, Z., and Shen, Z. X., "Massive dirac fermion on the surface of a magnetically doped topological insulator," *Science*, vol. 329, no. 5992, pp. 659–662, 2010.

[18] Cheng, P., Song, C., Zhang, T., Zhang, Y., Wang, Y., Jia, J.-F., Wang, J., Wang, Y., Zhu, B.-F., Chen, X., Ma, X., He, K., Wang, L., Dai, X., Fang, Z., Xie, X., Qi, X.-L., Liu, C.-X., Zhang, S.-C., and Xue, Q.-K., "Landau quantization of topological surface states in bi_2se_3," *Phys. Rev. Lett.*, vol. 105, p. 076801, Aug 2010.

[19] Choy, C. L., Wong, S. P., and Young, K., "Thermal expansion and grüneisen parameters for anisotropic solids," *Phys. Rev. B*, vol. 29, pp. 1741–1747, Feb 1984.

[20] Daghero, D. and Gonnelli, R. S., "Probing multiband superconductivity by point-contact spectroscopy," *Superconductor Science and Technology*, vol. 23, no. 4, p. 043001, 2010.

[21] Daghero, D., Tortello, M., Ummarino, G., Griveau, J.-C., Colineau, E., Eloirdi, R., Shick, A., Kolorenc, J., Lichtenstein, A., and Caciuffo, R., "Strong-coupling d-wave superconductivity in pucoga5 probed by point-contact spectroscopy," *Nature communications*, vol. 3, p. 786, 2012.

[22] de Gennes, P. and Saint-James, D., "Elementary excitations in the vicinity of a normal metal-superconducting metal contact," *Physics Letters*, vol. 4, no. 2, pp. 151 – 152, 1963.

[23] De Gennes, P.-G. and Pincus, P. A., *Superconductivity of metals and alloys*, vol. 86. WA Benjamin New York, 1966.

[24] Deutscher, G., "Andreev saint-james reflections: A probe of cuprate superconductors," *Rev. Mod. Phys.*, vol. 77, pp. 109–135, Mar 2005.

[25] Erickson, A. S., Chu, J.-H., Toney, M. F., Geballe, T. H., and Fisher, I. R., "Enhanced superconducting pairing interaction in indium-doped tin telluride," *Phys. Rev. B*, vol. 79, p. 024520, Jan 2009.

[26] Francombe, M., "Structure-cell data and expansion coefficients of bismuth telluride," *British Journal of Applied Physics*, vol. 9, no. 10, p. 415, 1958.

[27] Fu, L., "Topological crystalline insulators," *Phys. Rev. Lett.*, vol. 106, p. 106802, Mar 2011.

[28] Fu, L. and Berg, E., "Odd-parity topological superconductors: Theory and application to $cu_xbi_2se_3$," *Phys. Rev. Lett.*, vol. 105, p. 097001, Aug 2010.

[29] Fu, L. and Kane, C., "Topological insulators with inversion symmetry," *Phys. Rev. B*, vol. 76, p. 045302, Jul 2007.

[30] Fu, L., Kane, C., and Mele, E., "Topological insulators in three dimensions," *Phys. Rev. Lett.*, vol. 98, p. 106803, Mar 2007.

[31] Fu, L. and Kane, C. L., "Superconducting proximity effect and majorana fermions at the surface of a topological insulator," *Phys. Rev. Lett.*, vol. 100, p. 096407, Mar 2008.

[32] Geim, A. K. and Novoselov, K. S., "The rise of graphene," *Nature materials*, vol. 6, no. 3, pp. 183–191, 2007.

[33] Gibbons, T. G., "Calculation of the thermal expansion for a quasiharmonic model of tellurium," *Phys. Rev. B*, vol. 7, pp. 1410–1419, Feb 1973.

[34] Halperin, B., "Quantized hall conductance, current-carrying edge states, and the existence of extended states in a two-dimensional disordered potential," *Phys. Rev. B*, vol. 25, pp. 2185–2190, Feb 1982.

[35] Hao, L. and Lee, T. K., "Surface spectral function in the superconducting state of a topological insulator," *Phys. Rev. B*, vol. 83, p. 134516, Apr 2011.

[36] Hasan, M. and Kane, C., "*Colloquium* : Topological insulators," *Rev. Mod. Phys.*, vol. 82, pp. 3045–3067, Nov 2010.

[37] Hasan, M. Z., Xu, S.-Y., and Neupane, M., "Topological insulators, topological crystalline insulators, and topological kondo insulators," *arXiv preprint arXiv:1406.1040*, 2014.

[38] Hatsugai, Y., "Topological aspects of the quantum hall effect," *Journal of Physics: Condensed Matter*, vol. 9, no. 12, p. 2507, 1997.

[39] Hor, Y., Williams, A., Checkelsky, J., Roushan, P., Seo, J., Xu, Q., Zandbergen, H., Yazdani, A., Ong, N., and Cava, R., "Superconductivity in $cu_x bi_2 se_3$ and its implications for pairing in the undoped topological insulator," *Phys. Rev. Lett.*, vol. 104, p. 057001, Feb 2010.

[40] Hsieh, D., Qian, D., Wray, L., Xia, Y., Hor, Y. S., Cava, R., and Hasan, M. Z., "A topological dirac insulator in a quantum spin hall phase," *Nature*, vol. 452, no. 7190, pp. 970–974, 2008.

[41] Hsieh, T. H. and Fu, L., "Majorana fermions and exotic surface andreev bound states in topological superconductors: Application to $cu_x bi_2 se_3$," *Phys. Rev. Lett.*, vol. 108, p. 107005, Mar 2012.

[42] Hsieh, T. H., Lin, H., Liu, J., Duan, W., Bansil, A., and Fu, L., "Topological crystalline insulators in the snte material class," *Nature communications*, vol. 3, p. 982, 2012.

[43] Hu, C.-R., "Midgap surface states as a novel signature for d^2_{xa}-x^2_b-wave superconductivity," *Phys. Rev. Lett.*, vol. 72, pp. 1526–1529, Mar 1994.

[44] Ibach, H. and Ruin, E., "Thermal expansion of tellurium," *physica status solidi (b)*, vol. 41, no. 2, pp. 719–724, 1970.

[45] Jenkins, J. O., Rayne, J. A., and Ure, R. W., "Elastic moduli and phonon properties of bi_2 te_3," *Phys. Rev. B*, vol. 5, pp. 3171–3184, Apr 1972.

[46] Jozwiak, C., Chen, Y. L., Fedorov, A. V., Analytis, J. G., Rotundu, C. R., Schmid, A. K., Denlinger, J. D., Chuang, Y.-D., Lee, D.-H., Fisher, I. R., Birgeneau, R. J., Shen, Z.-X., Hussain, Z., and Lanzara, A., "Widespread spin polarization effects in photoemission from topological insulators," *Phys. Rev. B*, vol. 84, p. 165113, Oct 2011.

[47] Kane, C. and Mele, E., "Quantum spin hall effect in graphene," *Phys. Rev. Lett.*, vol. 95, p. 226801, Nov 2005.

[48] Kashiwaya, S., Tanaka, Y., Koyanagi, M., and Kajimura, K., "Theory for tunneling spectroscopy of anisotropic superconductors," *Physical Review B*, vol. 53, no. 5, p. 2667, 1996.

[49] Kim, O., Lee, K., Han, S., Ha, G., Kim, D., and Yoon, W., "Research activities of thermoelectric micro-cooler in kimm," in *Thermoelectrics, 2005. ICT 2005. 24th International Conference on*, pp. 331–334, June 2005.

[50] Kim, Y., Chen, X., Wang, Z., Shi, J., Miotkowski, I., Chen, Y., Sharma, P., Sharma, A. L., Hekmaty, M., Jiang, Z., and others, "Temperature dependence of raman-active optical phonons in bi2se3 and sb2te3," *Applied Physics Letters*, vol. 100, no. 7, p. 071907, 2012.

[51] Kirtley, J. R., "Inelastic transport through normal-metal superconductor interfaces," *Phys. Rev. B*, vol. 47, pp. 11379–11383, May 1993.

[52] Kirtley, J. R. and Scalapino, D. J., "Inelastic-tunneling model for the linear conductance background in the high-t_c superconductors," *Phys. Rev. Lett.*, vol. 65, pp. 798–800, Aug 1990.

[53] Kirtley, J. R., Washburn, S., and Scalapino, D. J., "Origin of the linear tunneling conductance background," *Phys. Rev. B*, vol. 45, pp. 336–346, Jan 1992.

[54] Kirzhner, T., Lahoud, E., Chaska, K. B., Salman, Z., and Kanigel, A., "Point-contact spectroscopy of $cu_{0.2}bi_2se_3$ single crystals," *Phys. Rev. B*, vol. 86, p. 064517, Aug 2012.

[55] Kitaev, A., "Periodic table for topological insulators and superconductors," *arXiv preprint arXiv:0901.2686*, 2009.

[56] Kitaev, A., "Fault-tolerant quantum computation by anyons," *Annals of Physics*, vol. 303, no. 1, pp. 2 – 30, 2003.

[57] Klemens, P. G., "Anharmonic decay of optical phonons," *Phys. Rev.*, vol. 148, pp. 845–848, Aug 1966.

[58] Klitzing, K., Dorda, G., and Pepper, M., "New method for high-accuracy determination of the fine-structure constant based on quantized hall resistance," *Phys. Rev. Lett.*, vol. 45, pp. 494–497, Aug 1980.

[59] Köhler, H. and Wöchner, E., "The g-factor of the conduction electrons in bi2se3," *physica status solidi (b)*, vol. 67, no. 2, pp. 665–675, 1975.

[60] Konig, M., Wiedmann, S., Brne, C., Roth, A., Buhmann, H., Molenkamp, L. W., Qi, X.-L., and Zhang, S.-C., "Quantum spin hall insulator state in hgte quantum wells," *Science*, vol. 318, no. 5851, pp. 766–770, 2007.

[61] Koren, G., Kirzhner, T., Lahoud, E., Chashka, K. B., and Kanigel, A., "Proximity-induced superconductivity in topological bi_2te_2se and bi_2se_3 films: Robust zero-energy bound state possibly due to majorana fermions," *Phys. Rev. B*, vol. 84, p. 224521, Dec 2011.

[62] Kriener, M., Segawa, K., Ren, Z., Sasaki, S., and Ando, Y., "Bulk superconducting phase with a full energy gap in the doped topological insulator cu x bi 2 se 3," *Physical review letters*, vol. 106, no. 12, p. 127004, 2011.

[63] Kriener, M., Segawa, K., Ren, Z., Sasaki, S., Wada, S., Kuwabata, S., and Ando, Y., "Electrochemical synthesis and superconducting phase diagram of $cu_xbi_2se_3$," *Phys. Rev. B*, vol. 84, p. 054513, Aug 2011.

[64] Laube, F., Goll, G., Löhneysen, H. v., Fogelström, M., and Lichtenberg, F., "Spin-triplet superconductivity in sr_2ruo_4 probed by andreev reflection," *Phys. Rev. Lett.*, vol. 84, pp. 1595–1598, Feb 2000.

[65] Lawson, B. J., Hor, Y. S., and Li, L., "Quantum oscillations in the topological superconductor candidate $cu_{0.25}bi_2se_3$," *Phys. Rev. Lett.*, vol. 109, p. 226406, Nov 2012.

[66] Leijnse, M. and Flensberg, K., "Introduction to topological superconductivity and majorana fermions," *Semiconductor Science and Technology*, vol. 27, no. 12, p. 124003, 2012.

[67] Levy, N., Zhang, T., Ha, J., Sharifi, F., Talin, A. A., Kuk, Y., and Stroscio, J. A., "Experimental evidence for *s*-wave pairing symmetry in superconducting $cu_xbi_2se_3$ single crystals using a scanning tunneling microscope," *Phys. Rev. Lett.*, vol. 110, p. 117001, Mar 2013.

[68] Liu, M. S., Bursill, L. A., Prawer, S., and Beserman, R., "Temperature dependence of the first-order raman phonon line of diamond," *Phys. Rev. B*, vol. 61, pp. 3391–3395, Feb 2000.

[69] Madelung, O., *Semiconductors: data handbook*. Butterworth, 1974.

[70] Mao, Z., Nelson, K., Jin, R., Liu, Y., and Maeno, Y., "Observation of andreev surface bound states in the 3-k phase region of sr_2ruo_4," *Phys. Rev. Lett.*, vol. 87, p. 037003, Jun 2001.

[71] Menéndez, J. and Cardona, M., "Temperature dependence of the first-order raman scattering by phonons in si, ge, and α-sn: Anharmonic effects," *Phys. Rev. B*, vol. 29, pp. 2051–2059, Feb 1984.

[72] Mills, K. C., *Thermodynamic Data for Inorganic Sulphides, Selenides and Tellurides*. Springer, 2004.

[73] Moore, G. and Read, N., "Nonabelions in the fractional quantum hall effect," *Nuclear Physics B*, vol. 360, no. 23, pp. 362 – 396, 1991.

[74] Moore, J. and Balents, L., "Topological invariants of time-reversal-invariant band structures," *Phys. Rev. B*, vol. 75, p. 121306, Mar 2007.

[75] Nagai, M., Tomitori, M., and Nishikawa, O., "Sharpening processes of scanning tunneling microscopy/scanning tunneling spectroscopy tips by thermal field treatment," *Japanese Journal of Applied Physics*, vol. 36, no. 6S, p. 3844, 1997.

[76] Nayak, C., Simon, S. H., Stern, A., Freedman, M., and Das Sarma, S., "Non-abelian anyons and topological quantum computation," *Rev. Mod. Phys.*, vol. 80, pp. 1083–1159, Sep 2008.

[77] Novak, M., Sasaki, S., Kriener, M., Segawa, K., and Ando, Y., "Unusual nature of fully gapped superconductivity in in-doped snte," *Phys. Rev. B*, vol. 88, p. 140502, Oct 2013.

[78] Novoselov, K., Geim, A. K., Morozov, S., Jiang, D., Grigorieva, M. K. I., Dubonos, S., and Firsov, A., "Two-dimensional gas of massless dirac fermions in graphene," *nature*, vol. 438, no. 7065, pp. 197–200, 2005.

[79] Pavlova, L., Shtern, Y., and Mironov, R., "Thermal expansion of bismuth telluride," *High Temperature*, vol. 49, no. 3, pp. 369–379, 2011.

[80] Peng, H., De, D., Lv, B., Wei, F., and Chu, C.-W., "Absence of zero-energy surface bound states in $cu_xbi_2se_3$ studied via andreev reflection spectroscopy," *Phys. Rev. B*, vol. 88, p. 024515, Jul 2013.

[81] Plecenník, A., Grajcar, M., Beňačka, i. c. v., Seidel, P., and Pfuch, A., "Finite-quasiparticle-lifetime effects in the differential conductance of $bi_2sr_2cacu_2o_y$/au junctions," *Phys. Rev. B*, vol. 49, pp. 10016–10019, Apr 1994.

[82] Qi, J., Chen, X., Yu, W., Cadden-Zimansky, P., Smirnov, D., Tolk, N., Miotkowski, I., Cao, H., Chen, Y., Wu, Y., and others, "Ultrafast carrier and phonon dynamics in bi2se3 crystals," *Applied Physics Letters*, vol. 97, no. 18, p. 182102, 2010.

[83] Qi, X.-L., Hughes, T., Raghu, S., and Zhang, S.-C., "Time-reversal-invariant topological superconductors and superfluids in two and three dimensions," *Phys. Rev. Lett.*, vol. 102, p. 187001, May 2009.

[84] Qi, X.-L. and Zhang, S.-C., "Topological insulators and superconductors," *Rev. Mod. Phys.*, vol. 83, pp. 1057–1110, Oct 2011.

[85] Ren, B., Picardi, G., and Pettinger, B., "Preparation of gold tips suitable for tip-enhanced raman spectroscopy and light emission by electrochemical etching," *Review of Scientific Instruments*, vol. 75, no. 4, 2004.

[86] Richter, W. and Becker, C. R., "A raman and far-infrared investigation of phonons in the rhombohedral v2vi3 compounds bi2te3, bi2se3, sb2te3 and bi2(te1xsex)3 (0 ¡ x ¡ 1), (bi1ysby)2te3 (0 ¡ y ¡ 1)," *physica status solidi (b)*, vol. 84, no. 2, pp. 619–628, 1977.

[87] Richter, W., Krost, A., Nowak, U., and Anastassakis, E., "Anisotropy and dispersion of coupled plasmon-lo-phonon modes in sb2te3," *Zeitschrift fr Physik B Condensed Matter*, vol. 49, no. 3, pp. 191–198, 1982.

[88] Roushan, P., Seo, J., Parker, C. V., Hor, Y., Hsieh, D., Qian, D., Richardella, A., Hasan, M. Z., Cava, R., and Yazdani, A., "Topological surface states protected from backscattering by chiral spin texture," *Nature*, vol. 460, no. 7259, pp. 1106–1109, 2009.

[89] Sasaki, S., Kriener, M., Segawa, K., Yada, K., Tanaka, Y., Sato, M., and Ando, Y., "Topological superconductivity in $cu_xbi_2se_3$," *Phys. Rev. Lett.*, vol. 107, p. 217001, Nov 2011.

[90] Sasaki, S., Ren, Z., Taskin, A., Segawa, K., Fu, L., and Ando, Y., "Odd-parity pairing and topological superconductivity in a strongly spin-orbit coupled semiconductor," *Phys. Rev. Lett.*, vol. 109, p. 217004, Nov 2012.

[91] Sato, M., "Topological odd-parity superconductors," *Phys. Rev. B*, vol. 81, p. 220504, Jun 2010.

[92] Sato, T., Tanaka, Y., Nakayama, K., Souma, S., Takahashi, T., Sasaki, S., Ren, Z., Taskin, A. A., Segawa, K., and Ando, Y., "Fermiology of the strongly spin-orbit coupled superconductor $sn_{1-x}in_xTe$: Implications for topological superconductivity," *Phys. Rev. Lett.*, vol. 110, p. 206804, May 2013.

[93] Schnyder, A., Ryu, S., Furusaki, A., and Ludwig, A., "Classification of topological insulators and superconductors in three spatial dimensions," *Phys. Rev. B*, vol. 78, p. 195125, Nov 2008.

[94] Sengupta, K., Kwon, H.-J., and M. Yakovenko, V., "Edge states and determination of pairing symmetry in superconducting sr_2ruo_4," *Phys. Rev. B*, vol. 65, p. 104504, Feb 2002.

[95] Seo, K., Han, L., and Sá de Melo, C. A. R., "Emergence of majorana and dirac particles in ultracold fermions via tunable interactions, spin-orbit effects, and zeeman fields," *Phys. Rev. Lett.*, vol. 109, p. 105303, Sep 2012.

[96] Sharvin, Y., "A possible method for studying fermi surfaces," *Journal of Experimental and Theoretical Physics*, vol. 21, no. 3, p. 655, 1965.

[97] Sheet, G., Mukhopadhyay, S., and Raychaudhuri, P., "Role of critical current on the point-contact andreev reflection spectra between a normal metal and a superconductor," *Phys. Rev. B*, vol. 69, p. 134507, Apr 2004.

[98] Shen, L. Y. L. and Rowell, J. M., "Zero-bias tunneling anomalies¯temperature, voltage, and magnetic field dependence," *Phys. Rev.*, vol. 165, pp. 566–577, Jan 1968.

[99] Shoemake, G. E., Rayne, J. A., and Ure, R. W., "Specific heat of n- and p-type bi_2te_3 from 1.4 to 90k," *Phys. Rev.*, vol. 185, pp. 1046–1056, Sep 1969.

[100] Sinha, S. and Ng, K.-W., "Zero bias conductance peak enhancement in $bi_2sr_2cacu_2O_8$/Pb tunneling junctions," *Phys. Rev. Lett.*, vol. 80, pp. 1296–1299, Feb 1998.

[101] Strijkers, G., Ji, Y., Yang, F., Chien, C., and Byers, J., "Andreev reflections at metal/superconductor point contacts: Measurement and analysis," *Phys. Rev. B*, vol. 63, p. 104510, Feb 2001.

[102] Svetlichnyy, P., Jiang, Z., and de Melo, C., "Parity violation in ferromagnet-superconductor heterostructures with strong spin-orbit coupling," *arXiv preprint arXiv:1403.6858*, 2014.

[103] Tanabe, K. and Hiraishi, J., "Experimental determination of true raman linewidths from measurements of linewidths observed at different slit openings," *Applied Spectroscopy*, vol. 35, no. 4, pp. 436–438, 1981.

[104] Tanaka, Y. and Kashiwaya, S., "Theory of tunneling spectroscopy of d-wave superconductors," *Phys. Rev. Lett.*, vol. 74, pp. 3451–3454, Apr 1995.

[105] Tang, H. and Herman, I. P., "Raman microprobe scattering of solid silicon and germanium at the melting temperature," *Phys. Rev. B*, vol. 43, pp. 2299–2304, Jan 1991.

[106] Taskin, A., Sasaki, S., Segawa, K., and Ando, Y., "Manifestation of topological protection in transport properties of epitaxial bi_2se_3 thin films," *Phys. Rev. Lett.*, vol. 109, p. 066803, Aug 2012.

[107] Thouless, D., Kohmoto, M., Nightingale, M., and den Nijs, M., "Quantized hall conductance in a two-dimensional periodic potential," *Phys. Rev. Lett.*, vol. 49, pp. 405–408, Aug 1982.

[108] Tzalenchuk, A., Lara-Avila, S., Kalaboukhov, A., Paolillo, S., Syväjärvi, M., Yakimova, R., Kazakova, O., Janssen, T., Fal'Ko, V., and Kubatkin, S., "Towards a quantum resistance standard based on epitaxial graphene," *Nature nanotechnology*, vol. 5, no. 3, pp. 186–189, 2010.

[109] van Wees, B. J., de Vries, P., Magnée, P., and Klapwijk, T. M., "Excess conductance of superconductor-semiconductor interfaces due to phase conjugation between electrons and holes," *Phys. Rev. Lett.*, vol. 69, pp. 510–513, Jul 1992.

[110] von Klitzing, K., "The quantized hall effect," *Reviews of Modern Physics*, vol. 58, no. 3, pp. 519–531, 1986.

[111] Wang, M.-X., Liu, C., Xu, J.-P., Yang, F., Miao, L., Yao, M.-Y., Gao, C., Shen, C., Ma, X., Chen, X., and others, "The coexistence of superconductivity and topological order in the bi2se3 thin films," *Science*, vol. 336, no. 6077, pp. 52–55, 2012.

[112] Wexler, G., "The size effect and the non-local boltzmann transport equation in orifice and disk geometry," *Proceedings of the Physical Society*, vol. 89, no. 4, p. 927, 1966.

[113] Wray, L. A., Xu, S.-Y., Xia, Y., San Hor, Y., Qian, D., Fedorov, A. V., Lin, H., Bansil, A., Cava, R. J., and Hasan, M. Z., "Observation of topological order in a superconducting doped topological insulator," *Nature Physics*, vol. 6, no. 11, pp. 855–859, 2010.

[114] Xia, Y., Qian, D., Hsieh, D., Wray, L., Pal, A., Lin, H., Bansil, A., Grauer, D., Hor, Y., Cava, R., and others, "Observation of a large-gap topological-insulator class with a single dirac cone on the surface," *Nature Physics*, vol. 5, no. 6, pp. 398–402, 2009.

[115] Xu, J.-P., Liu, C., Wang, M.-X., Ge, J., Liu, Z.-L., Yang, X., Chen, Y., Liu, Y., Xu, Z.-A., Gao, C.-L., and others, "Artificial topological superconductor by the proximity effect," *Physical Review Letters*, vol. 112, no. 21, p. 217001, 2014.

[116] Yamakage, A., Yada, K., Sato, M., and Tanaka, Y., "Theory of tunneling conductance and surface-state transition in superconducting topological insulators," *Phys. Rev. B*, vol. 85, p. 180509, May 2012.

[117] Yamakage, A., Yada, K., Sato, M., and Tanaka, Y., "Theory of tunneling spectroscopy in a superconducting topological insulator," *Physica C: Superconductivity*, vol. 494, no. 0, pp. 20 – 23, 2013. Proceedings of the 25th International Symposium on Superconductivity (ISS 2012) Advances in Superconductivity {XXV}.

[118] Yamashiro, M., Tanaka, Y., and Kashiwaya, S., "Theory of tunneling spectroscopy in superconducting sr_2ruo_4," *Phys. Rev. B*, vol. 56, pp. 7847–7850, Oct 1997.

[119] Yang, F., Ding, Y., Qu, F., Shen, J., Chen, J., Wei, Z., Ji, Z., Liu, G., Fan, J., Yang, C., and others, "Proximity effect at superconducting sn-bi 2 se 3 interface," *Physical Review B*, vol. 85, no. 10, p. 104508, 2012.

[120] Yazyev, O. V., Moore, J. E., and Louie, S. G., "Spin polarization and transport of surface states in the topological insulators bi_2se_3 and bi_2te_3 from first principles," *Phys. Rev. Lett.*, vol. 105, p. 266806, Dec 2010.

[121] Yu, W., Jiang, Y., Huan, C., Chen, X., Jiang, Z., Hawkins, S. D., Klem, J. F., and Pan, W., "Superconducting proximity effect in inverted inas/gasb quantum well structures with ta electrodes," *Applied Physics Letters*, vol. 105, no. 19, p. 192107, 2014.

[122] Zhang, F. C. and Rice, T. M., "Effective hamiltonian for the superconducting cu oxides," *Phys. Rev. B*, vol. 37, pp. 3759–3761, Mar 1988.

[123] Zhang, H., Liu, C.-X., Qi, X.-L., Dai, X., Fang, Z., and Zhang, S.-C., "Topological insulators in bi2se3, bi2te3 and sb2te3 with a single dirac cone on the surface," *Nature Physics*, vol. 5, no. 6, pp. 438–442, 2009.

[124] Zhang, Y., He, K., Chang, C.-Z., Song, C.-L., Wang, L.-L., Chen, X., Jia, J.-F., Fang, Z., Dai, X., Shan, W.-Y., and others, "Crossover of the three-dimensional topological insulator bi2se3 to the two-dimensional limit," *Nature Physics*, vol. 6, no. 8, pp. 584–588, 2010.

[125] Zhao, E. *private communications.*

VITA

Xunchi Chen was born in 1987 in the city of Nanjing, China, where he spent the first 22 years of his life. He graduated from High School Affiliated to Nanjing Normal University in 2005 and from Nanjing University with a bachelor's degree in physics in 2009. He then came to Tech to pursue a PhD degree. Six years of time in Atlanta made him grow up from a boy to a big boy. He is very proud to be the first doctor in his family, although he is still not sure what to do with it.